AEROSPACE VEHICLE SYSTEMS INSTITUTE
TEXAS A&M ENGINEERING EXPERIMENT STATION

Ms. Marlene H. Dortch
Secretary
Federal Communications Commission
445 12th Street, S.W.
Washington, DC 20554

August 30, 2017

Re: Use of Spectrum Bands Above 24 GHz For Mobile Radio Services, GN Docket 14-177, report supporting amendment of Part 15.255 of the Commission's rules for operation aboard aircraft within the band 57-71 GHz

Dear Ms. Dortch:

The Aerospace Vehicle Systems Institute (AVSI) at Texas A&M University is pleased to submit the attached report in response to an FCC request for technical studies and interference analyses associated with enabling the use of transceivers on aircraft operating in the 57-71 GHz range pursuant to a *Report and Order and Further Notice of Proposed Rulemaking (FNPRM)* [FCC Report 16-89A1] action under the above-referenced docket.

Detailed analyses, dynamic modeling, and field testing provided in this report demonstrate that transmitters in compliance with 47 CFR 15.255 will comply with International Telecommunications Union (ITU-R) protection levels developed for the incumbent passive service and will not interfere with those services.

AVSI respectfully requests consideration of this report in proceedings under the FNPRM and is prepared to respond to any questions or clarifications requested by the FCC.

Respectfully submitted,

David Redman
Director, Aerospace Vehicle Systems Institute

754 H.R. Bright Building
3141 TAMU | College Station, Texas 77843-3141

AVSI
AEROSPACE VEHICLE SYSTEMS INSTITUTE
TEXAS A&M ENGINEERING EXPERIMENT STATION

AFE 85 Project Report

Analysis of Potential Interference from WiGig Radios on Aircraft to EESS Passive Sensors

30 August 2017

Aerospace Vehicle Systems Institute
754 HRBB - MS 3141
College Station, TX 77843-3141
Office: +1-979-845-5568
FAX: +1-979-339-4079
Web: www.avsi.aero

Table of Contents

Table of Contents i
List of Figures ii
List of Tables vi
List of Acronyms vii
References ix
Executive Summary x
Analysis of Potential Interference from WiGig Radios on Aircraft to EESS Passive Sensors 1
1 Report Overview 1
2 EESS Interference Assessment 2
2.1 Analysis and Testing Summary 2
2.2 Methodology for Interference Assessment 3
2.3 Relevant EESS Sensors 7
2.4 In-band, Out-of-Band, and Spurious Emissions Power Levels 9
2.5 Interference Calculation, Frequency Dependencies 14
2.6 Interference Assessment Results for In-Band, OOB, and Spurious Emissions 17
3 Conclusion 23
4 Acknowledgements 23
A : WiGig Aircraft Emissions Model 24
B : In-Aircraft Emissions Testing 63
C : Aircraft WiGig Performance Testing 71
D : Fuselage Materials Comparison 78
E : Aircraft Fuselage Attenuation Testing 79
F : Reference Area Definition for Dynamic Simulation 89
G : EESS Satellite and Dynamic Simulation Set-up 90
H : Atmospheric Attenuation 97
I : FAA Air Traffic Data Set 99

List of Figures

Figure 1: Summed Emitted Power. 4
Figure 2: Illustration of the calculation of sum interference for NAC aircraft. 5
Figure 3: Example snapshots from dynamic simulation for 3 time steps every 10s. 6
Figure 4: Example total interference computed over time in the dynamic simulation (step size in 20 ms). 6
Figure 5: WiGig in-band, OoB and spurious frequency domains and potentially affected EESS band. 7
Figure 6: 802.11-2016 DMG transmit mask. 10
Figure 7: Comparison of transmit mask (from 802.11-2016 [2]) and typical actual transmit spectrum. 11
Figure 8: Illustration of OoB, spurious domains, transmit power mask and single channel power levels in relation to relevant EESS band, 40 dBm in-band emission level. 12
Figure 9: In-band, OoB, and spurious emission levels following 802.11-2016 DMG transmit mask with 40 dBm in-band EIRP. 13
Figure 10: Total emission level assuming 40 dBm EIRP in-band, 7 dB MEF, FCC spurious emission limit. 14
Figure 11: Comparison of Zenith atmospheric attenuation for different altitudes in K2 frequency range, and WiGig channels 1, 2 and 3 in-band, out of band, and spurious emission domains. 15
Figure 12: Dependency of Zenith atmospheric attenuation on aircraft altitude for different frequencies in the considered EESS band. 16
Figure 13: Combined single aircraft sum EIRP and atmospheric loss without aircraft attenuation. 17
Figure 14: ECCDF from dynamic simulation of sensor K2, 25 dBm/100 MHz at 54.35 GHz. 21
Figure 15: ECCDF from dynamic simulation of sensor K2, 35 dBm/100 MHz at 57.4 GHz. 22
Figure A.1: WiGig distribution to seatback displays. 25
Figure A.2: WiGig distribution to seatback displays (cross-section). 25
Figure A.3: WiGig and PEDs. 26
Figure A.4: WiGig backbone utilizing relays or repeaters. 26
Figure A.5: Aircraft window test setup. 29
Figure A.6: Measurement scenarios. 30
Figure A.7: Measurement scenarios (alternate view). 30
Figure A.8: Measurements results for measurement scenario depicted in Figure A.6. 31
Figure A.9: Measurement results for measurement Scenario II depicted in Figure A.6. 31
Figure A.10: Side view of Ansys Savant model approximating the measurement setup. 32
Figure A.11: Top view of Ansys Savant model approximating the measurement setup. 33
Figure A.12: Simulated gain of the transmit antenna without the fuselage section. 33
Figure A.13: Simulated gain of the transmit antenna with (red) and without (black) the fuselage section. 34
Figure A.14: On-aircraft test concept. 35
Figure A.15: RX power vs. frequency and transmit antenna orientation. 36
Figure A.16: Transmit and receive conical horn Sage SAC-2309-15-S2 antenna typical gain in the E and H planes. 37
Figure A.17: Simulated conical horn E-plane gain. 37
Figure A.18: Simulated conical horn H-Plane gain. 38
Figure A.19: Top view of simulation model. 38
Figure A.20: Approximate access point locations. 39
Figure A.21: Depiction of antenna in 777-200 model. 40
Figure A.22: Histograms of gain for each of the 37 available steering angles at Access Point Position 1. 41

Figure A.23: Empirical cumulative distribution of gain for each of the 37 available steering angles at Access Point Position 1. 41
Figure A.24: Histogram of gain over all 37 available steering angles at Access Point Position 1. 42
Figure A.25: Empirical cumulative distribution of gain for all 37 available steering angles at Access Point Position 1. 42
Figure A.26: Histograms of gain for each of the 37 available steering angles at Access Point Position 2. 43
Figure A.27: Empirical cumulative distribution of gain for each of the 37 available steering angles at Access Point Position 2. 43
Figure A.28: Histogram of gain over all 37 available steering angles at Access Point Position 2. 44
Figure A.29: Empirical cumulative distribution of gain for all 37 available steering angles at Access Point Position 2. 44
Figure A.30: Histograms of gain for each of the 37 available steering angles at Access Point Position 3. 45
Figure A.31: Empirical cumulative distribution of gain for each of the 37 available steering angles at Access Point Position 3. 45
Figure A.32: Histogram of gain over all 37 available steering angles at Access Point Position 3. 46
Figure A.33: Empirical cumulative distribution of gain for all 37 available steering angles at Access Point Position 3. 46
Figure A.34: Histograms of gain for each of the 37 available steering angles at Access Point Position 4. 47
Figure A.35: Empirical cumulative distribution of gain for each of the 37 available steering angles at Access Point Position 4. 47
Figure A.36: Histogram of gain over all 37 available steering angles at Access Point Position 4. 48
Figure A.37: Empirical cumulative distribution of gain for all 37 available steering angles at Access Point Position 4. 48
Figure A.38: Measurement data on 777-200 copied from Annex E: Aircraft Fuselage Attenuation Testing. 50
Figure A.39: Histograms of gain for each of the fan beam steering angles at Access Point Position 1. 51
Figure A.40: Empirical cumulative distribution of gain for each of the fan beam steering angles at Access Point Position 1. 51
Figure A.41: Histogram of gain over all fan beam steering angles at Access Point Position 1....52
Figure A.42: Empirical cumulative distribution of gain over all fan beam steering angles at access point location 1. 52
Figure A.43: Depiction of antenna in 777-200 model. 54
Figure A.44: An alternate depiction of the antenna in the 777-200 model. 54
Figure A.45: Histograms of gain for each of the circular symmetric antenna steering angles at the PED position. 55
Figure A.46: Empirical cumulative distribution of gain for each of the circular symmetric steering angles at the PED position. 55
Figure A.47: Histogram of gain over all circular symmetric antenna steering angles at the PED position. 56
Figure A.48: Empirical cumulative distribution of gain over all circular symmetric antenna steering angles at the PED position. 56
Figure A.49: Fit results from access point position 1. 58
Figure A.50: Fit results from Access Point Position 2. 58
Figure A.51: Fit results from Access Point Position 3. 59
Figure A.52: Fit results from access point position 4. 59
Figure A.53: Fit results for access point position 1 with fan beam antenna. 60

Figure A.54: Fit results for PED use case. 60
Figure B.1: General test concept. 64
Figure B.2: Transmitter block diagram. 64
Figure B.3: Conducted transmit power at the output of the variable attenuator. 65
Figure B.4: Receive block diagram 66
Figure B.5: Rx lineup conducted gain. 67
Figure B.6: Starboard door measurement location. 68
Figure B.7: Measured power vs. frequency with starboard door open and closed. 68
Figure B.8: RX power vs. frequency and transmit antenna orientation. 69
Figure C.1: Boeing B777-200 – LOPA. 71
Figure C.2: Distance Measurements – AP Set-up – Laptop TGS60-1. 72
Figure C.3: Distance Measurements – STA Set-up – Laptop TGS60-2. 72
Figure C.4: Distance Measurements – Results. 73
Figure C.5: Coverage Measurements – STA Set-up – Laptop TGS60-2. 74
Figure C.6: Coverage Measurements – AP Set-up – Window – Laptop TGS60-1. 75
Figure C.7: Coverage Measurements – AP Aisle – Obtained Data Rate per Seat Column. 75
Figure C.8: Coverage Measurements – AP Window – Obtained Data Rate per Seat Column. 76
Figure C.9: Coverage Measurements – AP Aisle – Data Rate Map. 76
Figure C.10: Coverage Measurements – AP Window – Data Rate Map. 77
Figure E.1: AVSI Test Team and Boeing 777-200 aircraft. 79
Figure E.2: Basic attenuation test setup. 80
Figure E.3: Reference measurements. 81
Figure E.4: Determining correlation. 81
Figure E.5: Data from aircraft cabin. 82
Figure E.6: Three measurement configurations. 83
Figure E.7: Free space attenuation measurement setup. 83
Figure E.8: Transmit antenna 19” from the passenger window. 83
Figure E.9: Transmit antenna 101” from the passenger window. 83
Figure E.10: Comparison of cabin window LoS signal levels. 84
Figure E.11: Transmitter in overhead storage bin. 85
Figure E.12: Fuselage attenuation data. 85
Figure E.13: Attenuation from the fuselage. 86
Figure E.14: Flight deck window test setup. 87
Figure E.15: Flight deck window attenuation. 87
Figure E.16: Coated and non-coated window comparison. 88
Figure F.1: CONUS Air Traffic 1800 8 February 2017. 89
Figure G.1: Simulated satellite ground tracks (blue) from STK ephemeris data and 2e6 km^2 reference area (red). 92
Figure G.2: Satellite tracks and scanned points for a 12 h period. 93
Figure G.3: Sensor gain vs. off-axis angle (according to ITU-R RS.1813-1). 94
Figure G.4: Detail of reference area. Sample time is 20 ms. 94
Figure G.5: Detail of reference area incl. contours of sensor main beam gain. 95
Figure G.6: Satellite tracks for 7 days. 95
Figure G.7: Satellite tracks over 7 days resulting in ~30,000 scan points in reference area (20 ms sampling period). 96
Figure H.1: Ground-space Zenith attenuation for the reference atmosphere; Dry, Water vapor, and total attenuation. 97
Figure H.2: Zenith attenuation in dB from 50 to 70 GHz. 98
Figure I.1: Aircraft count for data set after initial filtering based on aircraft type and geographical area. 99

Figure I.2: Aircraft altitude distribution. 101
Figure I.3: Aircraft speed distribution. 102
Figure I.4: Aircraft distribution for peak. 103
Figure I.5: Aircraft distribution for altitude. 104
Figure I.6: Distribution of aircraft for peak time step, 60s time window (altitude, long/lat) within 2e6 km^2 reference area. 105

List of Tables

Table 1: Relevant EESS band and related protection criterion. 7
Table 2: Reproduction of Table 14 from ITU-Rec. RS.1861-0. 8
Table 3: OoB frequency ranges. 10
Table 4: Out of band emissions following 802.11-2016 DMG transmit power mask for 40 dBm EIRP. 11
Table 5: Worst-case single aircraft interference calculation for frequency 54.35 GHz. 18
Table 6: Worst-case single aircraft interference calculation for frequency 57.4 GHz (highlighting shows differences to Table 5). 19
Table 7: Key parameters used in the dynamic simulation for frequencies 54.35 GHz and 57.4 GHz. 20
Table A.1: Average difference between measured receive power at a transmit azimuth angle of 0 degrees (aligned with receive antenna boresight) and a sweep of transmit azimuth angles. 36
Table A.2: Average difference between measured receive power at a transmit azimuth angle of 0 degrees (aligned with receive antenna boresight) and simulated average difference over a sweep of transmit azimuth angles. 39
Table A.3: WiGig channel 1 access point physical locations relative to the nose of the aircraft. 40
Table A.4: Summary of gain based on empirical cumulative distribution for each access point location. 49
Table A.5: Effective attenuation based on empirical cumulative distributions of gain summarized in Table A.4. 49
Table A.6: Summary of gain and effective aircraft attenuation based on empirical cumulative distributions for a fan beam and circular symmetric 30 degree HPBW antennas in access point position 1. 53
Table A.7: Summary of PED gain and effective attenuation statistics with comparison to access point 1 statistics. 57
Table A.8: Summary of overall gain statistics for each of the simulation scenarios. 57
Table A.9: Summary of fit values for variable A in X^2 distribution. 61
Table B.1: Major items in transmitter test setup. 65
Table B.2: Major items in the receive test setup. 66
Table B.3: Average difference between measured receive power at a transmit azimuth angle of 0 degrees (aligned with receive antenna boresight) and a sweep of transmit azimuth angles. 70
Table C.1: Distance Measurements – List of Fixtures/Monuments along the Test Path. 73
Table G.1: K2 and K3 sensor overlap with WiGig harmonics. 90
Table G.2: NOAA current and planned EESS. 90
Table I.1: Aircraft population within Reference Area. 100

List of Acronyms

Acronym	Explanation
AP	Access Point
AVSI	Aeronautical Vehicular Systems Institute
CFRP	Carbon Fiber Reinforced Plastic
CFR	Code of Federal Regulations
CONUS	Continental United States
CORF	Committee on Radio Frequencies
CSMA/CA	Carrier-Sense Multiple Access with Collision Avoidance
dB	decibel
dBi	dB over isotropic
DMG	Directional Multi-Gigabit
ECCDF	Empirical Complementary Cumulative Distribution Function
EESS	Earth Exploration Satellite Service
COTS	Commercial Off-The-Shelf
ETSI	European Telecommunications Standards Institute
FAA	Federal Aviation Administration
FCC	Federal Communications Commission
HPBW	Half Power Beam Width
IEEE	Institute of Electrical and Electronics Engineers
IF	Intermediate Frequency
IFE	In-Flight Entertainment
ITO	Indium Tin Oxide
ITU	International Communications Union
LOPA	Locations of Passenger Accommodations
LoS	Line of Sight
MAC	Medium (or Media) Access Control (in reference to OSI communications model)
MCS	Modulation and Coding Scheme
MEF	Multiple Equipment Factor
NOAA	National Oceanographic and Atmospheric Administration
NSF	National Science Foundation
OoB	Out of Band

Acronym	Explanation
OoBE	Out of Band Emission
PEC	Perfect Electrical Conductor
PED	Personal electronic device
PHY	PHYsical layer (in reference to the OSI communications model)
RX	Receive or receiver
STA	STAtion
STK	System Tool Kit
T-PED	Transmitting Passenger Electronic Device
TX	Transmit or transmitter
WiGig	Wireless technology from the Wireless Gigabit Alliance
X2	Chi square

References

[1] [3]802.11ad TM -2012, IEEE Standard for Information technology--Telecommunications and information exchange between systems--Local and metropolitan area networks--Specific requirements-Part 11: Wireless LAN Medium Access Control (MAC) and Physical Layer (PHY) Specifications Amendment 3: Enhancements for Very High Throughput in the 60 GHz Band, Approved 19 October 2012.

[2] [17]802.11TM-2016, IEEE Standard for Information technology— Telecommunications and information exchange between systems Local and metropolitan area networks— Specific requirements, Part 11: Wireless LAN Medium Access Control (MAC) and Physical Layer (PHY) Specifications, Approved 7 December 2016.

[3] [2]Recommendation ITU-R RS.2017-0 (08/2012), Performance and interference criteria for satellite passive remote sensing.

[4] [15]FCC Code of Federal Regulations §15.255, Operation within the band 57-71 GHz.

[5] [13]Recommendation ITU-R RS.1858-0 (01/2010), Characterization and assessment of aggregate interference to the Earth exploration-satellite service (passive) sensor operations from multiple sources of man-made emissions.

[6] [1]Recommendation ITU-R RS.1861-0 (01/2010), Typical technical and operational characteristics of Earth exploration-satellite service (passive) systems using allocations between 1.4 and 275 GHz.

[7] [14]Recommendation ITU-R P.525-3 (11/2016), Calculation of free-space attenuation.

[8] [7]Recommendation ITU-R P.676-11 (09/2016), Attenuation by atmospheric gases.

[9] [10]Recommendation ITU-R RS.1813-1 (02/2011), Reference antenna pattern for passive sensors operating in the Earth exploration-satellite service (passive) to be used in compatibility analyses in the frequency range 1.4-100 GHz.

[10] [5]Recommendation ITU-R SM1541-6 (08/2015), Unwanted emissions in the out-of-band domain.

[11] [6]Recommendation ITU-R SM.1539-1 (11/2002), Variation of the boundary between the out-of-band and spurious domains required for the application of Recommendations ITU-R SM.1541 and ITU-R SM.329.

[12] [8] FCC Certification Test Report 15U20374-E1A, Qualcomm Atheros 802.11ad Module (https://fccid.io/pdf.php?id=2718223).

[13] [11]FCC Certification Test Report 14U18424-1, Intel 60GHz Wireless Module Adapter (Client side) (https://fccid.io/pdf.php?id=2414315).

[14] [4]ETSI TR 102 555 v 1.1.1, Electromagnetic compatibility and Radio spectrum Matters (ERM); Technical characteristics of multiple gigabit wireless systems in the 60 GHz range System Reference Document.

[15] [12]ETSI EN 302 567 V1.2.1 (2012-01), Broadband Radio Access Networks (BRAN); 60 GHz Multiple-Gigabit WAS/RLAN Systems; Harmonized EN covering the essential requirements of article 3.2 of the R&TTE Directive.

[16] RTCA DO-294B Guidance on Allowing Transmitting Portable Electronic Devices (T-PEDs) on Aircraft.

Executive Summary

This report responds to an FCC request for technical studies and interference analyses associated with enabling the use of transceivers on aircraft operating in the 57-71 GHz range. Detailed analyses, dynamic modeling, and field testing provided in this report demonstrate that transmitters in compliance with 47 CFR 15.255 will comply with International Telecommunications Union (ITU-R) protection levels developed for the incumbent passive service and will not interfere with those services.

To justify this conclusion, example applications and use cases are provided, and analyses is undertaken to determine the extent of radio frequency emissions from an aircraft fuselage. The example applications provide a sizing reference for the number of transmitting devices on an aircraft. Performance testing confirmed that achievable bandwidth and coverage is sufficient for intended commercial applications.

Aircraft fuselage materials were also evaluated to determine effective attenuation. Two airframe manufacturers' analysis and testing reached the same conclusion: Carbon Fiber Reinforced Plastic (CFRP) fuselage skin offers similar attenuation to that of aluminum skinned aircraft.

Independent studies evaluated aircraft effective attenuation. All of the studies reached similar conclusions: Typical aircraft effective fuselage attenuation is 40 dB in the frequency range of 57-71 GHz and this attenuation value should be used in any interference analysis.

Analysis of Potential Interference from WiGig Radios on Aircraft to EESS Passive Sensors

1 Report Overview

Determining the potential interference to Earth Exploration Satellite Service (EESS) systems from transmitters on aircraft was a multi-faceted problem that required the cooperation of government agencies, universities and aviation industry participants.
Analyses and modeling of emissions from WiGig devices, which include use cases to establish the number and location of potential emitters transmitting within an aircraft fuselage in the frequency range 57-71 GHz are provided in Annex A: WiGig Aircraft Emissions Model

Measurements taken to validate the emissions models are documented in Annex B: In-Aircraft Emissions Testing.

Performance testing to confirm the efficiency of WiGig transmitters in aircraft is documented in Annex C: Aircraft WiGig Performance Testing.

Fuselage skin material radio frequency attenuation values are summarized in Annex D: Fuselage Materials Comparison.

Aircraft fuselage radio frequency attenuation field testing is provided in Annex E: Aircraft Fuselage Attenuation Testing.

The ITU Recommends that emissions from multiple devices within a two million square kilometer reference area be dynamically simulated to determine if EESS interference protection threshold is exceeded. The selection criteria for that reference area is documented in Annex F: Reference Area Definition for Dynamic Simulation.

A list of NOAA active and planned satellites is provided in Annex G: EESS Satellite and Dynamic Simulation Set-up.

Based upon ITU-R Recommendations, an analysis of atmospheric free air attenuation between aircraft and satellites is provided in Annex H: Atmospheric Attenuation.

A database of air traffic over the continental United States for the busiest week during 2016 from which traffic over the reference area was derived is provided in Annex I: FAA Air Traffic Data Set.

2 EESS Interference Assessment

The EESS Interference Assessment documents the results of analyses, modeling and testing of potential interference between WiGig (802.11ad [1] and [2]) devices operating in the 57-71 GHz range onboard commercial aircraft and incumbent passive services operating in or near the WiGig frequency range.

The results of this analysis conclude that any emissions into the relevant earth exploration satellite service (EESS) passive sensor band operated onboard aircraft are well below the protection levels recommended by the ITU.

More specifically, the analysis shows that the protection criterion published in ITU-R Recommendation RS.2017 [3] of -169dBW/100MHz is satisfied with a significant margin of at least 20 dB when considering worst-case peak air traffic and worst-case aircraft emissions.

2.1 Analysis and Testing Summary

Analysis and testing of WiGig transmitters utilizing all available channels in the 57-71 GHz range is assessed.

Worst-case emission levels from WiGig channels 1 to 6 are obtained using the FCC power level restrictions for in-band and spurious emissions found in 47 CFR §15.255 [4]. The 802.11-2016 transmit mask was also used to obtain out-of-band emission levels [2].

A Multiple Equipment Factor (MEF) is established in accordance with RTCA DO-294B [16] to represent the maximum number of simultaneously transmitting devices in a WiGig aircraft installation.

FAA traffic data is analyzed to determine worst-case traffic volume and patterns within a two million square kilometer bounding area within which aggregate interference is assessed. This volume is used in order to comply with ITU-R Recommendation RS.1858-0 [5].

Satellite sensor data provided by the National Oceanographic and Atmospheric Administration (NOAA) is assessed to determine potentially at-risk satellites and establish worst-case potentially at-risk frequencies for consideration based on interference criteria established in Recommendation ITU-R RS.1861 [6].

The threat assessment is organized as follows:

- Section 2.2 Methodology for Interference Assessment describes the general methodology applied for assessment of potential interference to EESS (passive) sensors.
- Section 2.3 Relevant EESS Sensors identifies the EESS (passive) sensors that may be affected from WiGig devices operating on-board aircraft.
- Section 2.4 In-band, Out-of-Band, and Spurious Emissions Power Levels derives worst-case WiGig transmit power levels for in-band, out-of-band and spurious emissions domains.
- Section 2.5 Interference Calculation, Frequency Dependencies provides the power levels and at-risk frequencies to evaluate in the interference calculations.
- Section 2.5 Interference Calculation, Frequency Dependencies also presents the results for worst-case interference calculations. Interference statistics from detailed dynamic simulations are presented and compared with the applicable ITU-R protection criteria.
- Section 2.6 Interference Assessment Results for In-Band, OOB, and Spurious Emissions presents the conclusions drawn regarding the potential impact of interference from WiGig radios on aircraft to EESS passive sensors.

2.2 Methodology for Interference Assessment

International Telecommunications Union (ITU) Recommendation ITU-R RS.1858-0 (01/2010) [5] describes the characteristics and applicable methodology to assess aggregate interference to Earth exploration-satellite service (passive) sensor operations from multiple sources. Guidelines are included for characterization of interference sources and methods for interference aggregation. Accordingly, the interference analysis described in this document is based on this ITU-R Recommendation. ITU-R RS.1858-0 recommends either a simple worst-case interference assessment or dynamic simulations to determine if the interference protection criteria of ITU-R RS.2017 [3] are met. Both assessments were performed.

The single worst case and dynamic simulation interference assessments are described in the sections that follow.

2.2.1 Single Aircraft Worst-case Interference Assessment

Interference received at the satellite from a single aircraft was computed from the overall interference emitted by the multiple WiGig radios on the aircraft and then fuselage attenuation, free-space and atmospheric losses and the satellite sensor gain were applied using the criteria specified in Recommendations ITU-R P.525 [7], P.676 [8], and RS.1813 [9]. Interference from a single aircraft was established by summing the worst-case in-band, out-of-band and spurious emissions from all WiGig devices operating in various WiGig channels, including a multiple equipment factor (MEF) to account for the number of devices that can simultaneously transmit in the aircraft at the considered frequencies. In addition, attenuation due to the fuselage or antenna directivity was considered.

It should be noted that, for any given access point using a single WiGig channel, only a single transmitter can be active at any time, irrespective of the number of clients associated with this access point. This is due to the access point and its clients utilizing Time-Division Multiplex (TDM)/ Time-Division Multiple Access (TDMA) methods for spectrum access. Further, WiGig devices employ Carrier-Sense Multiple Access with Collision Avoidance (CSMA/CA) protocols to ensure that uncoordinated clients cannot inadvertently transmit simultaneously.

In an aircraft cabin with 30 access points sharing 6 channels, each channel would be reused by 5 access points. Thus, a Multiple Equipment Factor (MEF) of 5 would be applied to represent the number of devices sharing a channel, which is approximately 7 dB.

The sum power at any frequency was determined by adding: (a) in-band emissions, (b) out-of-band emissions of adjacent channels, and (c) spurious emissions of all used channels. The equation below represents a worst-case scenario because it adds peak power levels for in-band, out-of-band (OoB), and spurious emissions. In practice the respective peak emissions will likely radiate in different spatial directions and thus would not directly add up to the values calculated in this document.

The equation is as follows and illustrated in Figure 1:

$$P_{sum}(f) = N_{AP}/N_{ch} \sum_{n=1}^{N_{ch}} P_{TX}(f - f_c(n)) \quad \text{[power spectral density, linear]}$$

where

N_{ch}: Number of WiGig channels (up to 6) used on radios on single aircraft

N_{AP}: Number of access points deployed on single aircraft

$MEF = N_{AP}/N_{ch}$: Multiple equipment factor

$P_{TX}(f)$: In-band, out-of-band emission levels following WiGig transmit mask and FCC spurious emission level. Same absolute emission levels are assumed for all channels.

$f_c(n)$: Center frequency of channel n

Applicable power levels for in-band, out-of-band, and spurious emissions are derived in section 2.4 In-band, Out-of-Band, and Spurious Emissions Power Levels.

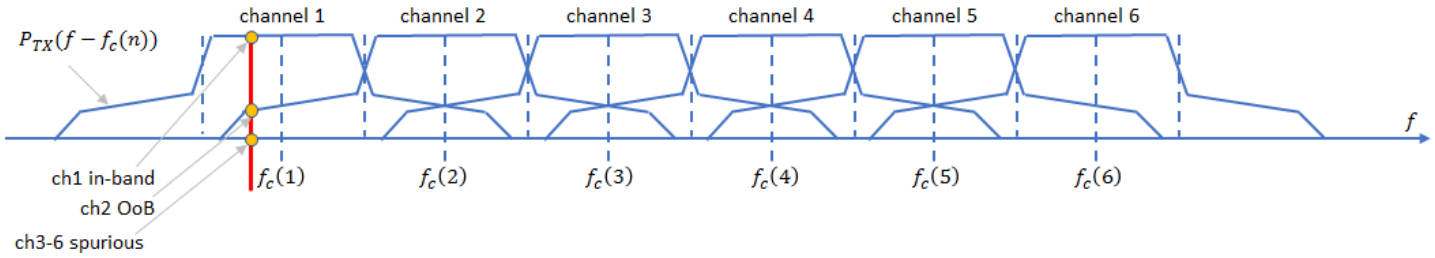

Figure 1: Summed Emitted Power.
Emitted power is the sum of in-band, out-of-band, and spurious emissions due to the overlapping 802.11 Directional Multi Gigabit (DMG) transmit masks for channels 1 to 6. Each channel is reused $MEF = N_{AP}/N_{ch}$ times.

2.2.2 Dynamic Simulation of Aggregate Interference

In the dynamic simulation of the EESS scenario, interference is computed for a population of aircraft by first computing the interference contribution from each aircraft and then calculating the sum (in linear scale) of all the aircraft in a particular area.

The bounds of the simulation area within which the aircraft population resides and the positions and movements of that aircraft population are documented in Annex F: Reference Area Definition for Dynamic Simulation and Annex I: FAA Air Traffic Data Set. The aircraft population used in this simulation reflects the highest density one-week period for air traffic in 2016 as reported by the FAA and is the worst-case air traffic of calendar year 2016. During the simulation aircraft positions were kept fixed during each time instance, which ensures the highest number of aircraft in the considered time period.

Satellite movements were dynamically simulated along the orbit track and the sensor scanning pattern, thus the total interference becomes a function of time (see Figure 4). The time step size was chosen sufficiently small (20 ms or less) to ensure that the distance between adjacent scan points was small in relation to sensor beamwidth. (A 20 ms step size translates to approximately a 5 dB beamwidth as shown in Annex G, Figure G.5).

Total interference calculations of total interference were performed using worst-case frequencies within an EESS sensor's frequency range. Worst-case frequencies within an EESS band under consideration are those frequencies where atmospheric loss is minimum and interference emission is maximum. Worst-case EESS frequencies are identified in 2.5 Interference Calculation, Frequency Dependencies.

The total interference received by the satellite from all N_{AC} aircraft is accordingly calculated as (see also Figure 2 below):

$$I_{sum}(f,t) = \sum_{i=1}^{N_{AC}} \frac{P_i(f) G_{RX}\big(f, \phi_i(t)\big)}{L_{fsl}\big(f, d_i(t)\big) L_{atmo}\big(f, h_i, \epsilon_i(t)\big)} \qquad \text{[linear]}$$

where

f: Signal frequency.

t: Time.

N_{AC}: Number of aircraft.

$P_i(f) = P_{sum}(f)/L_{fus}$: Effective total interference power emitted by aircraft i towards the satellite. This contains fuselage attenuation L_{fus} as obtained from measurements. The same interference power was assumed for all aircraft.

$G_{RX}(f, \phi_i(t))$: Satellite sensor gain, with $\phi_i(t)$ being the off-boresight angle towards the aircraft, assuming a circularly symmetric antenna pattern, based on Recommendation ITU-R RS.1813 [9].

$L_{fsl}(f, d_i(t))$: Free space loss for aircraft-satellite distance $d_i(t)$, based on Recommendation ITU-R P.525 [7].

$L_{atmo}(f, h_i, \epsilon_i(t))$: aircraft-to-satellite atmospheric loss for aircraft altitude h_i and satellite elevation ϵ_i, based on ITU-R P.676 [8].

The total interference time series is used to obtain the interference statistics to be compared with the protection criteria defined in Recommendation ITU-R RS.2017-0 [3].
A fuselage attenuation L_{fus} of 40 dB is used based upon simulation, aircraft testing and analysis.
Refer to Annex A: WiGig Aircraft Emissions Model and Annex B: In-Aircraft Emissions Testing for details.

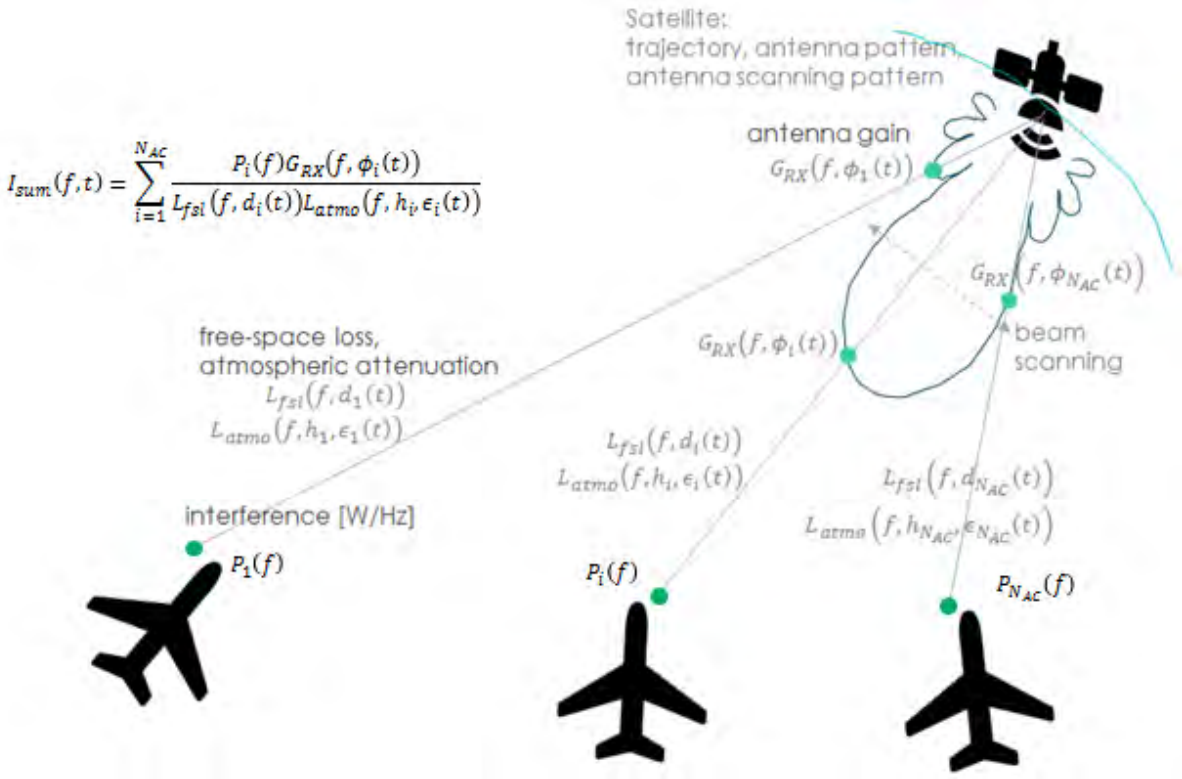

Figure 2: Illustration of the calculation of sum interference for N_{AC} aircraft.

Figure 3 provides snapshots from the dynamic simulation, including satellite movement along the orbit track and sensor scanning. Further details of the dynamic simulation set up are described in Section 2.5.

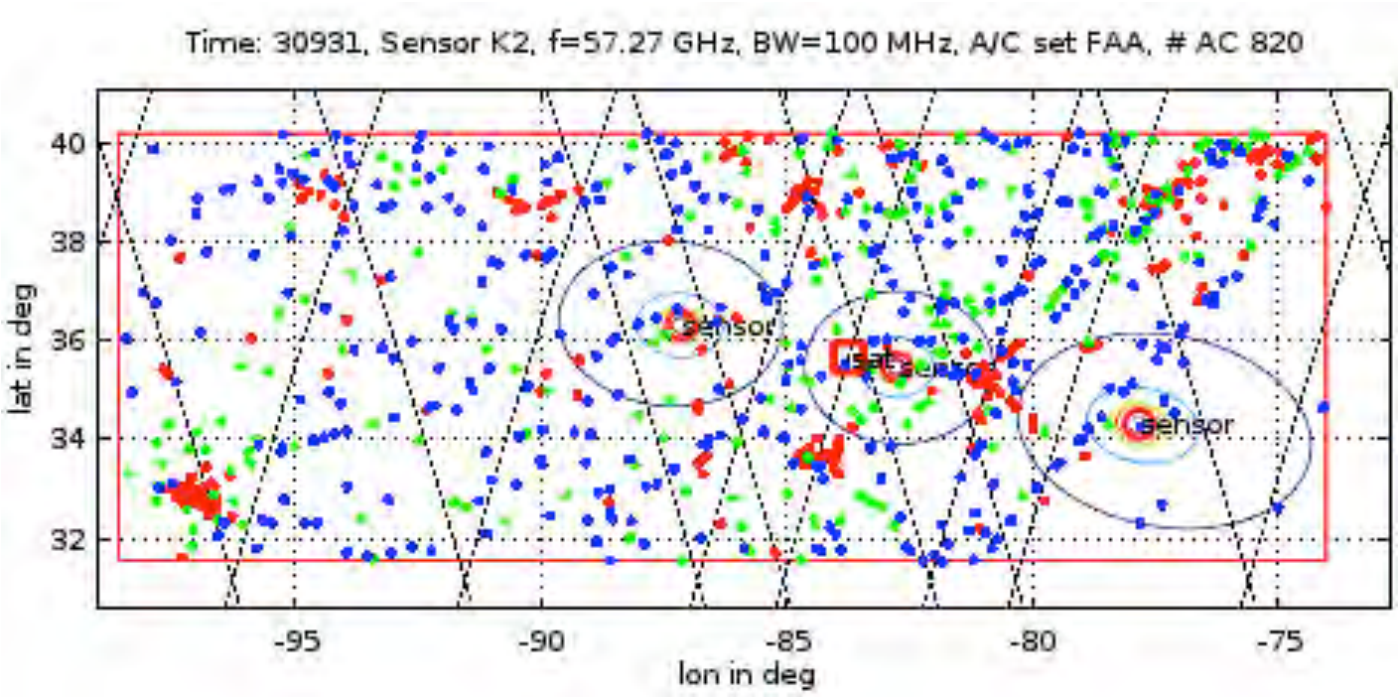

Figure 3: Example snapshots from dynamic simulation for 3 time steps every 10s.
Black dashed: satellite ground track. Contour plots: sensor gain on ground. Small red square: satellite location. Red circle: sensor peak gain on ground. Red/green/blue dots: aircraft positions.

Figure 4 shows the sum of interference over a wider time window as computed for the assumed worst-case aircraft distribution in the required 2e6 km^2 reference area.

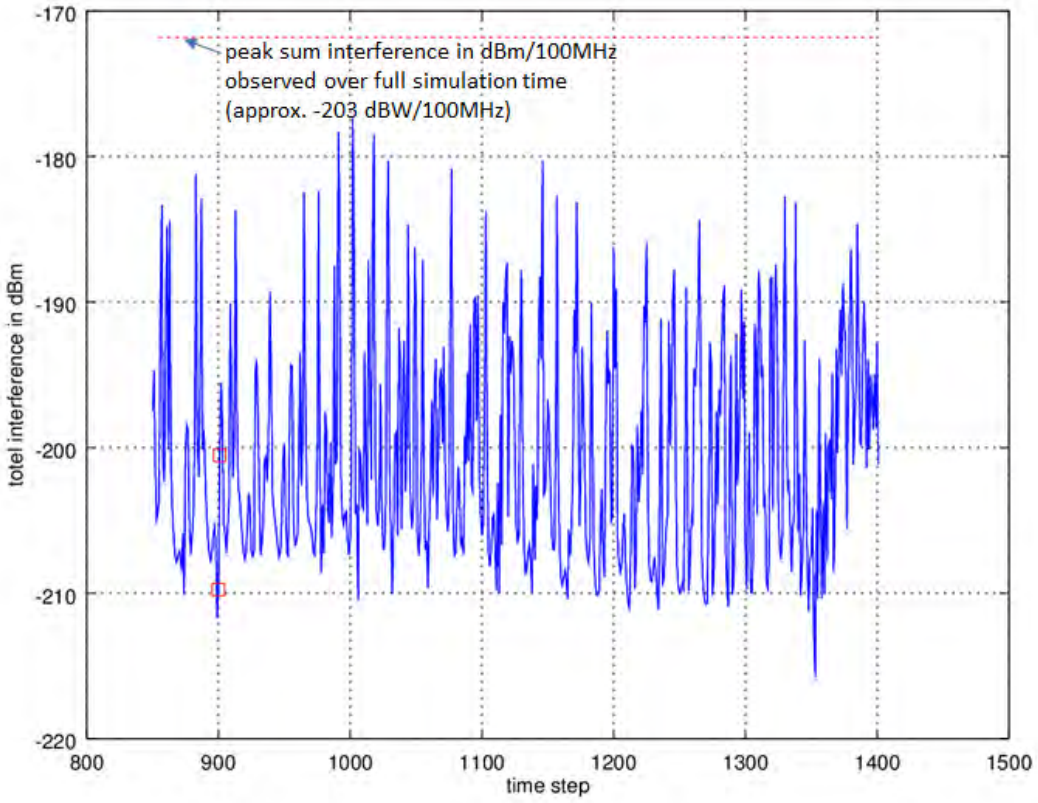

Figure 4: Example total interference computed over time in the dynamic simulation (step size in 20 ms).

2.3 Relevant EESS Sensors

The OoB domain upper and lower limits towards the spurious domain are defined by (see Recommendations ITU-R SM.1541-6 [10] and ITU-R SM.1539-1 [11]):

$$f_c - (0.5\ GHz + 1.5B_N) = f_c - 3.74\ GHz;\quad f_c - 0.5B_N = f_c - 1.08\ GHz,$$
$$f_c + 0.5B_N = f_c + 1.08\ GHz;\quad f_c + (0.5\ GHz + 1.5B_N) = f_c + 3.74\ GHz,$$

with WiGig channel center frequency f_c and assuming a necessary bandwidth $B_N = 2.16$ GHz.

WiGig channel bands and OoB and spurious domain limits for channel 1 to 3 and 6 are illustrated in Figure 5 below, which also shows the relative location of the EESS band under consideration.

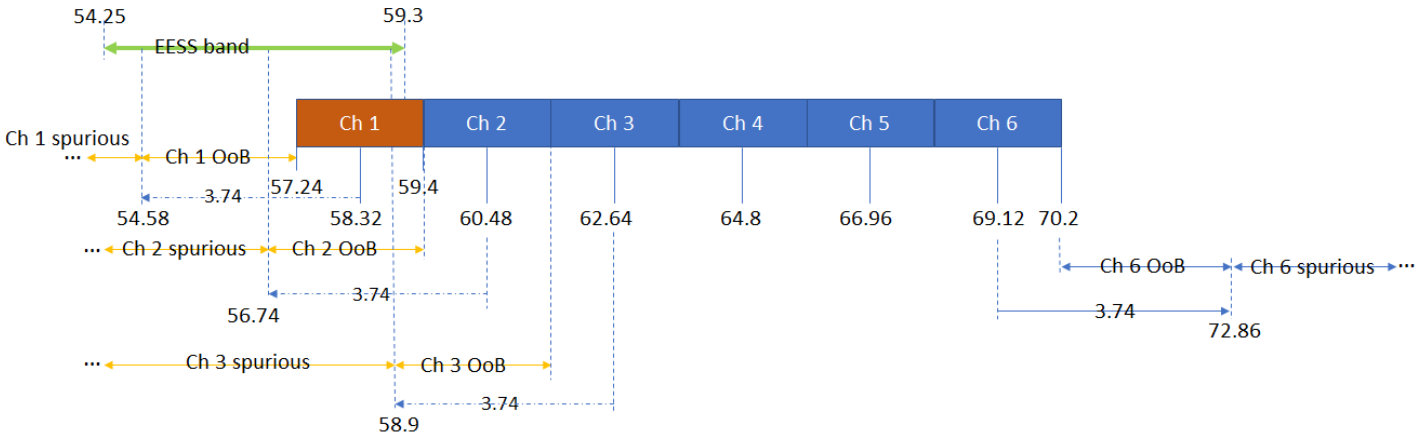

Figure 5: WiGig in-band, OoB and spurious frequency domains and potentially affected EESS band.

According to Recommendation ITU-R RS.1861-0 [6], EESS (passive) sensors operating in the 54.25-59.4 GHz frequency range are represented by systems “K2” and “K3”. The two systems “K2” and “K3” were reviewed. System K2 was considered to be the more demanding scenario due to K2’s higher sensor peak gain.

K2’s mechanical nadir scan sensor characteristics required for the interference analysis are taken from Table 14. Applicable protection criteria are defined in Recommendation ITU-R RS.2017-0 [3], and are provided in Table 1 and Table 2 below.

Table 1: Relevant EESS band and related protection criterion.

Parameter	Value(s)	Comments
Frequency range	54.25 – 59.3 GHz	ITU-R RS.1861-0 [6]
Protection criterion	-169 dBW/100 MHz at 0.01% or less.	ITU-R RS.2017-0 [3]

Table 2: Reproduction of Table 14 from ITU-Rec. RS.1861-0.

	Sensor K1	Sensor K2	Sensor K3	Sensor K4
Sensor type	Conical scan	Mechanical nadir scan	Mechanical nadir scan	Conical scan
Orbit parameters				
Altitude	828 km	824 km	833 km 822 km*	835 km
Inclination	98.7°		98.6° 98.7°*	98.85°
Eccentricity	0		0 0.001*	0
Repeat period	17 days	9 days	9 days 29 days*	
Sensor antenna parameters				
Number of beams	2		30 earth fields per 8 s scan period	1
Reflector diameter	2.2 m	0.203 m	0.15 m	0.6 m
Maximum beam gain	60 dBi	37.9 dBi	34.4 dBi	51 dBi
Polarization	See Table 15	See Table 16	See Table 17	See Table 18
–3 dB beamwidth	0.39°	2.2°	3.3°	0.6°
Instantaneous field of view	16 km × 12 km	Nadir FOV: 31.6 km Outer FOV: 136.7 × 60 km	Nadir FOV: 48.5 km (3.3°) Outer FOV: 149.1 × 79.4 km 147 × 79 km*	Outer FOV 18 × 43 km
Main beam efficiency	95%			
Off-nadir pointing angle	46.8°	±52.73° cross-track	±48.33° cross-track	55.4°
Beam dynamics	31.6 rpm	8/3 s scan period cross-track; 96 earth fields per scan period	8 s scan period	2.88 s scan period
Incidence angle at Earth	55.7°		0 57.5°*	65°

Sensor antenna parameters				
Number of beams	2		30 earth fields per 8 s scan period	1
Reflector diameter	2.2 m	0.203 m	0.15 m	0.6 m
Maximum beam gain	60 dBi	37.9 dBi	34.4 dBi	51 dBi
Polarization	See Table 15	See Table 16	See Table 17	See Table 18
–3 dB beamwidth	0.39°	2.2°	3.3°	0.6°
Instantaneous field of view	16 km × 12 km	Nadir FOV: 31.6 km Outer FOV: 136.7 × 60 km	Nadir FOV: 48.5 km (3.3°) Outer FOV: 149.1 × 79.4 km 147 × 79 km*	Outer FOV 18 × 43 km
Main beam efficiency	95%			
Off-nadir pointing angle	46.8°	±52.73° cross-track	±48.33° cross-track	55.4°
Beam dynamics	31.6 rpm	8/3 s scan period cross-track; 96 earth fields per scan period	8 s scan period	2.88 s scan period
Incidence angle at Earth	55.7°		0 57.5°*	65°

Sensor receiver parameters				
Sensor integration time	1.2 ms	18 ms	165 ms	N/A
Channel bandwidth	See Table 15	See Table 16	See Table 17	See Table 18
Measurement spatial resolution				
Horizontal resolution	3 km	32 km	48 km	18 km
Vertical resolution	3 km	32 km	48 km	18 km

2.4 In-band, Out-of-Band, and Spurious Emissions Power Levels

2.4.1 In-Band Emissions

Following 47 CFR §15.255(b)(1)(i) the average EIRP of any emission shall not exceed 40 dBm and the peak EIRP of any emission shall not exceed 43 dBm.

EIRP was further constrained due to RF exposure limits requirements. The FCC limit for General Population/Uncontrolled Exposure in the frequency range 1.5 GHz-100 GHz is 1 mW/cm2 (see 47 CFR §1.1310), which translates to a maximum allowable EIRP of approximately 37 dBm at a minimum distance of 20 cm.

WiGig standard equipment has an average and peak EIRP between 23 dBm and 30 dBm, significantly below the FCC limits, see, e.g., FCC WiGig radio certification test reports [12] and [13].

While the current generation of commercial WiGig radios does not support the highest EIRP level allowed by the FCC, this study assumes an in-band EIRP within any WiGig channel of 40 dBm in an

effective 1.88 GHz channel bandwidth, equivalent to 27.3 dBm in 100 MHz bandwidth. This assumption represents the worst-case in-band emission level, which in turn leads to worst-case OoB emission levels.

2.4.2 Spurious Emissions

47 CFR §15.255(c) requires that in the range of 40-200 GHz spurious emissions shall not exceed 90 pW/cm2 at a distance of 3 meters, corresponding to -10 dBm/MHz.

Other regional regulations, e.g. within CEPT member states, limit spurious emissions to 30 dBm/MHz (see [14] and [15]). WiGig is intended to provide high-speed communications for the portable computing products distributed in open retail market. Device portability implies mobility and a need to operate in multiple regulatory environments. Chipsets for portable devices are produced by the hundreds of millions. To achieve the necessary economies of scale for such large production WiGig manufacturers produce chipsets designed for global application and multi-national certification –either by limiting chipset design to the most stringent requirement limits or by designing chipsets to be configurable to meet regulatory limits in every intended country of operation. While this is a probable outcome, the interference analysis in this document utilizes the FCC limit as a conservative worst-case.

2.4.3 Out-of-Band Emissions

Of the six WiGig channels in the 57-71 GHz band, only the out-of-band domains of channels 1, 2, and 3 extend into the considered EESS band, see Figure 5 above and Table 3 below.

Table 3: OoB frequency ranges.

Parameter	Value
Frequency range of interest for EESS sensor type K2 (for comparison)	54.25 – 59.3 GHz
OoB range for channel 1	54.58 – 57.24 GHz
OoB range for channel 2	56.74 – 59.4 GHz
OoB range for channel 3	58.9 – 61.56 GHz

OoB emission levels were computed by applying both the FCC 40 dBm in-band transmit EIRP limit and the 802.11-2016 DMG transmit mask (from 802.11-2016 [2]). Refer to Figure 6.

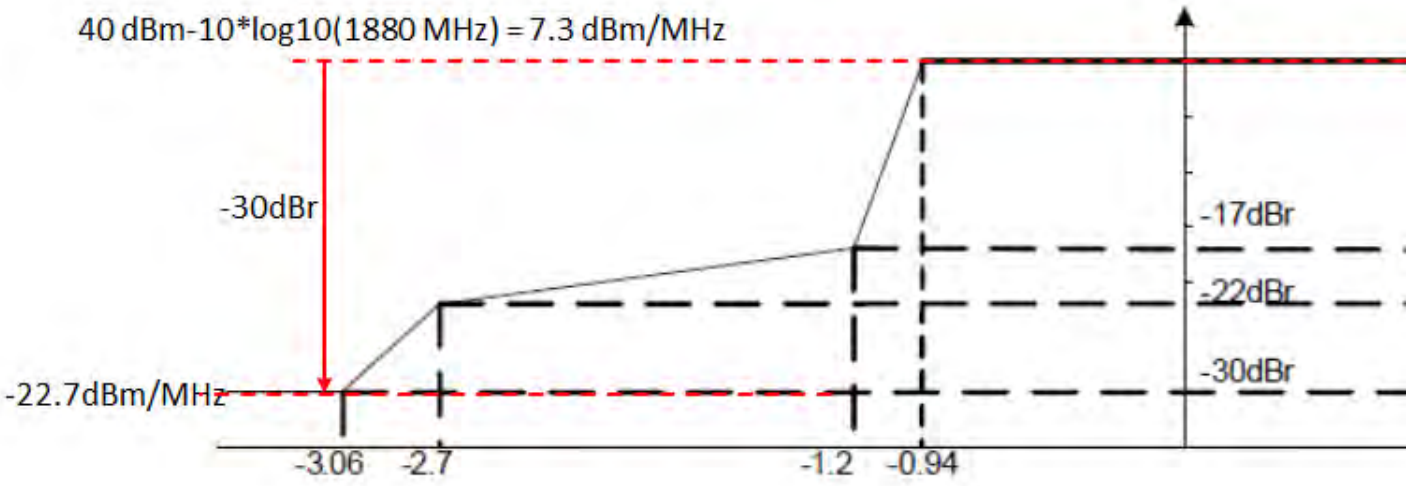

Figure 6: 802.11-2016 DMG transmit mask.
The FCC average transmit power limit of 40 dBm is used for computing absolute out of band transmit power levels.

Figure 7 below shows that actual OoB emission levels should be significantly below the worst-case limits defined by the transmit mask used in the analyses of this document.

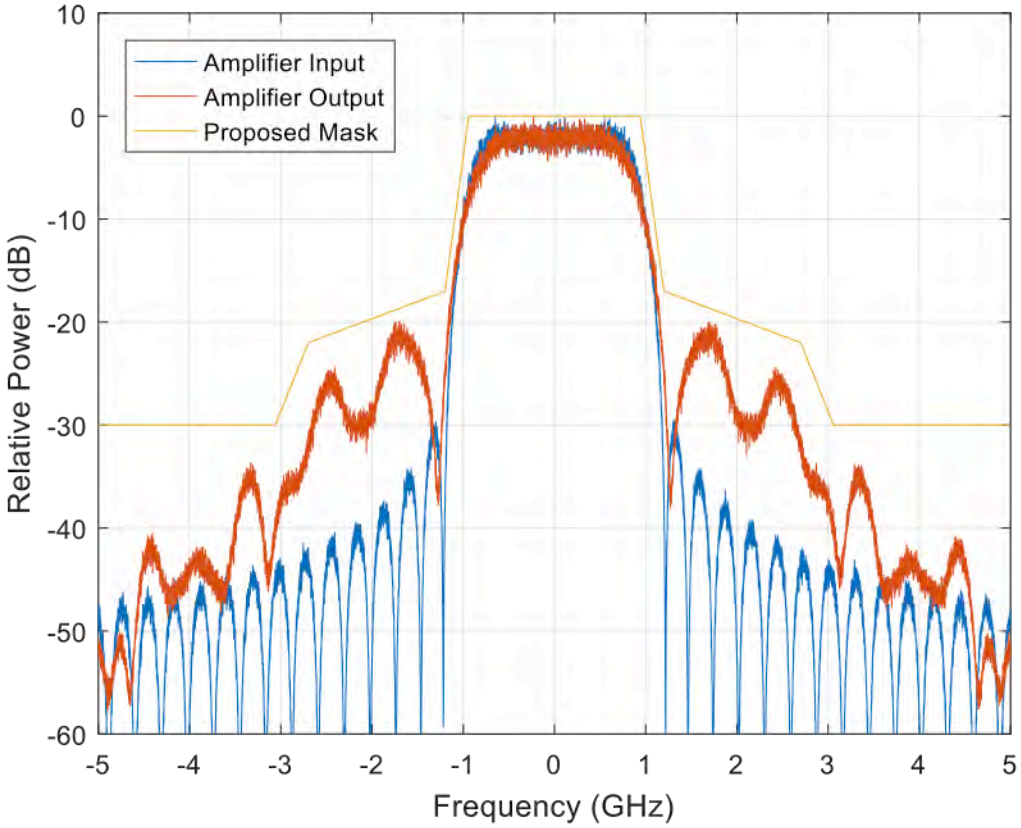

Figure 7: Comparison of transmit mask (from 802.11-2016 [2]) and typical actual transmit spectrum.

Referring to the 802.11-2016 DMG transmit mask, the emitted power outside the respective WiGig channel can be computed by applying the corresponding dBr values of the transmit mask to obtain the worst-case OoB emission levels, see Table 4 and Figure 8 below.

Table 4: Out of band emissions following 802.11-2016 DMG transmit power mask for 40 dBm EIRP.

Frequency offset from center frequency f_c	Absolute transmit power level in dBm in 100 MHz, f and f_c in GHz
$0 \leq \lvert f - f_c \rvert < 0.94$ GHz	$P_r = 27.3\ dBm$ (40 dBm in 1.88 GHz)
0.94 GHz $\leq \lvert f - f_c \rvert < 1.2$ GHz	$P_r - 17$ dBr $(\lvert f - f_c \rvert - 0.94)/(1.2 - 0.94)$
$1.2\ GHz \leq \lvert f - f_c \rvert < 2.7\ GHz$	$P_r - 17\ dBr - 5\ dBr\ (\lvert f - f_c \rvert - 1.2)/(2.7 - 1.2)$
$2.7\ GHz \leq \lvert f - f_c \rvert < 3.06\ GHz$	$P_r - 22\ dBr - 8\ dBr\ (\lvert f - f_c \rvert - 2.7)/(3.06 - 2.7)$
$3.06\ GHz \leq \lvert f - f_c \rvert < 3.74\ GHz$	$P_r - 30dBr = -2.7\ dBm$
$3.74\ GHz \leq \lvert f - f_c \rvert$	$+10\ dBm$ (FCC limit)

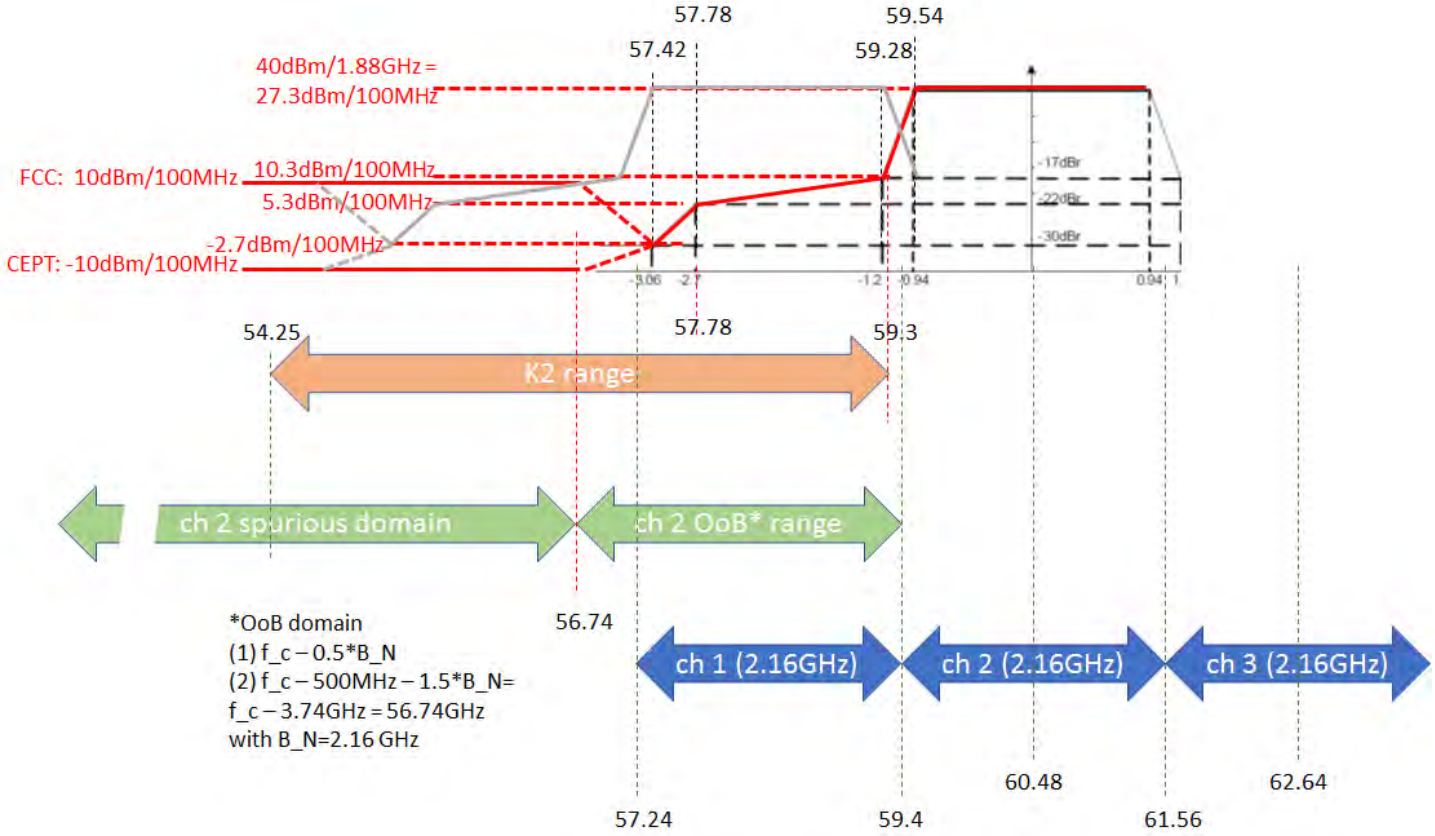

Figure 8: Illustration of OoB, spurious domains, transmit power mask and single channel power levels in relation to relevant EESS band, 40 dBm in-band emission level.

Note that the -30 dBr point at 3.06 GHz of the WiGig transmit mask is still within the OoB domain. Between the 3.06 GHz point and the start of the spurious domain at 3.74 GHz offset we assume a constant emission level of 30 dBr. This creates a step at the start of the spurious domain, where the FCC's spurious emission limit of +10 dBm/100 MHz is assumed, see Figure 9. For comparison the 10 dBm/100 MHz limit from CEPT is also shown.

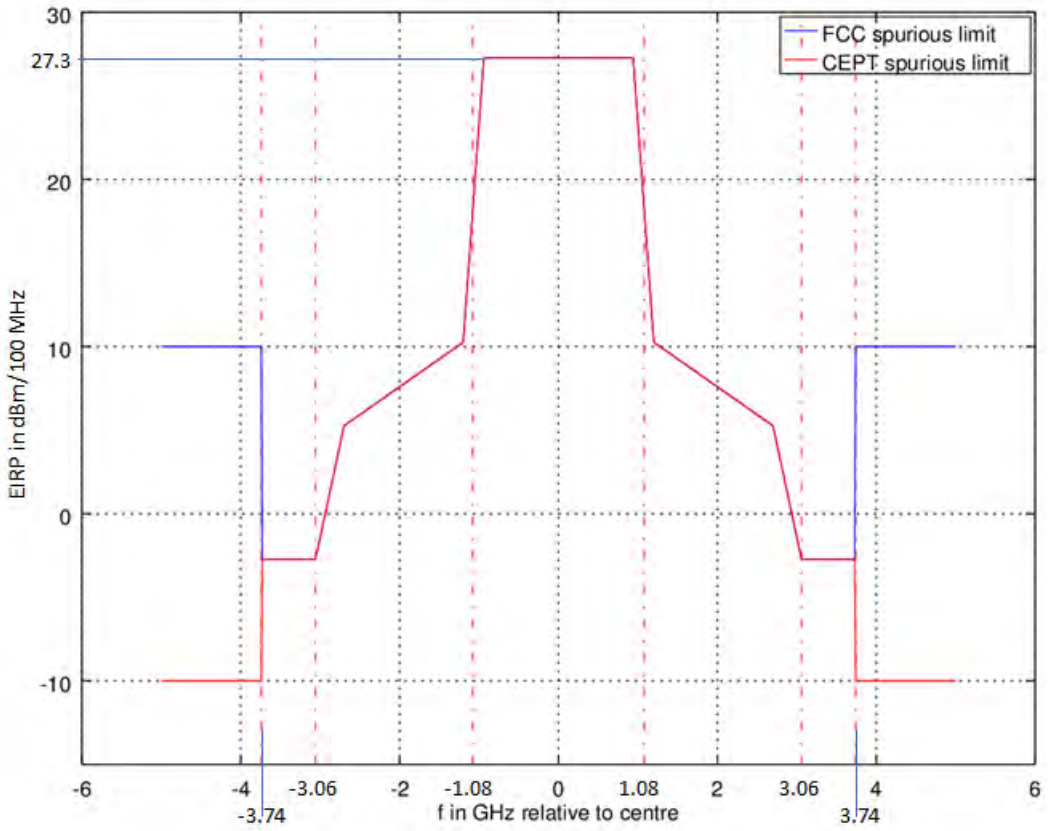

Figure 9: In-band, OoB, and spurious emission levels following 802.11-2016 DMG transmit mask with 40 dBm in-band EIRP.

2.4.4 Total Emission Levels

As explained in Section 2.2, the total emission level to consider for the interference analysis is obtained by summing (in linear scale) all the emissions in a 100 MHz frequency range used by the EESS which include in-band, OoB, and spurious emissions. Further a multiple equipment factor was considered to take into account the number of WiGig channels that may be reused in an aircraft installation.

Figure 10 shows the worst-case sum emission level considering all 6 channels are used and including a 7 dB MEF. Note that when using the FCC in-band and spurious emission limits, summed spurious emissions dominate OoB emissions and only provide for less than 10 dB signal to interference ratio. This again illustrates that the total emission levels used in the analyses represent a worst-case scenario that is highly unlikely to ever occur.

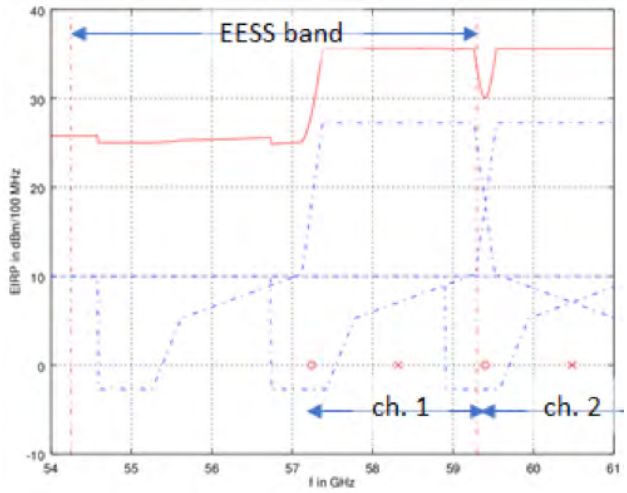

Figure 10: Total emission level assuming 40 dBm EIRP in-band, 7 dB MEF, FCC spurious emission limit.

2.5 Interference Calculation, Frequency Dependencies

Atmospheric attenuation plays a key role in the assessment of interference to EESS in or close to the 60 GHz band. Atmospheric attenuation was computed according to ITU-R Rec. P.676-11 [8]. The reference atmospheric parameters used are altitude dependent, with the following reference values at sea level: pressure = 101.325 kPa, temperature = 288.15 K, and water vapor density = 7.5 g/m3.

Atmospheric losses in the frequency range considered have a minor dependence on typical variations of pressure, temperature and water vapor density at sea level. Attenuation is mostly due to O2 resonance. Therefore, atmospheric loss for the reference values was assumed representative for any atmospheric condition (refer to Annex H: Atmospheric Attenuation for additional details of free space loss).

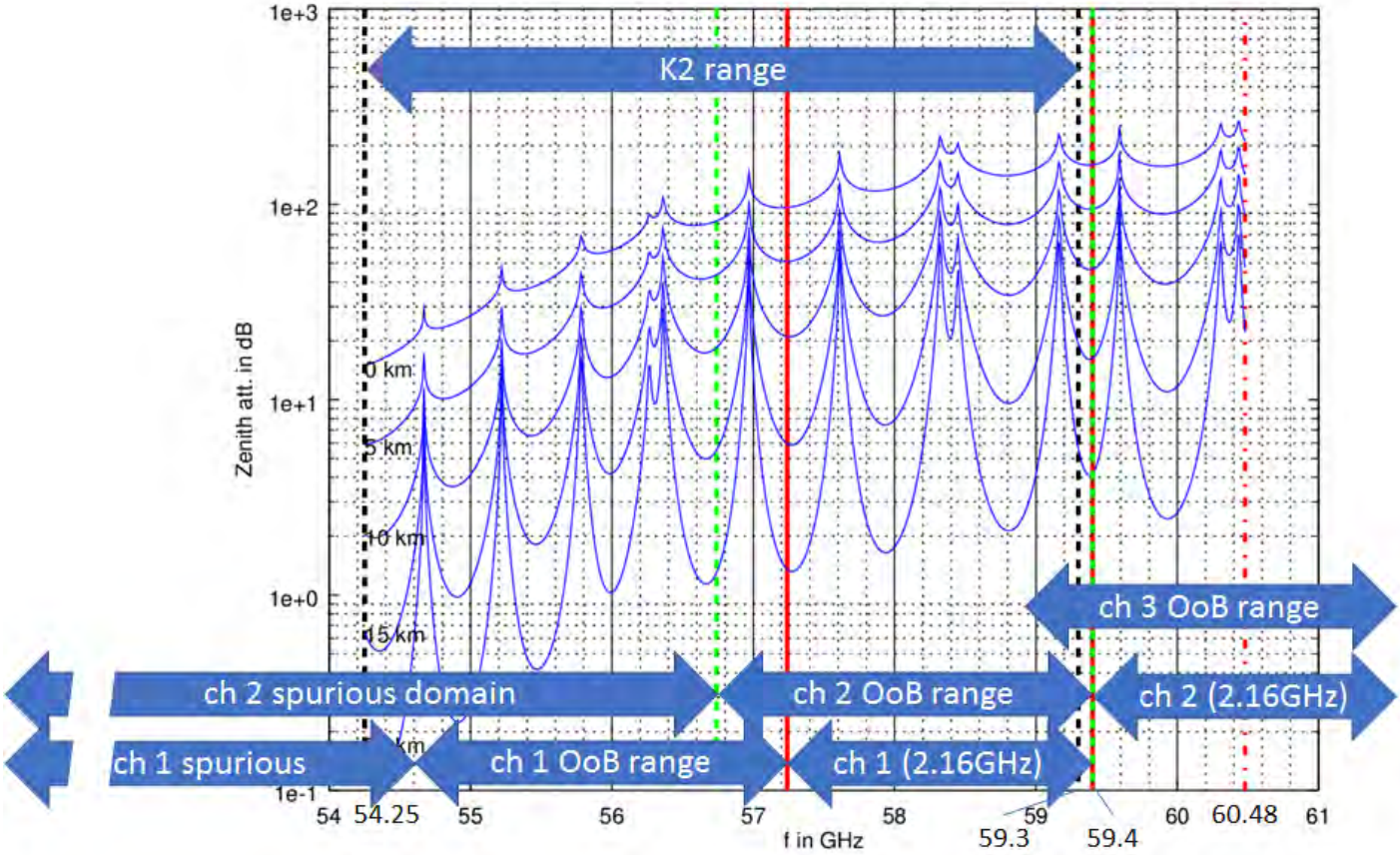

Figure 11: Comparison of Zenith atmospheric attenuation for different altitudes in K2 frequency range, and WiGig channels 1, 2 and 3 in-band, out of band, and spurious emission domains.

Atmospheric attenuation between aircraft and EESS sensor is highly dependent on the frequency and aircraft altitude, as illustrated in Figure 12. Variations in atmospheric attenuation due to altitude are specifically addressed by the dynamic simulations presented in Section 2.6.2.

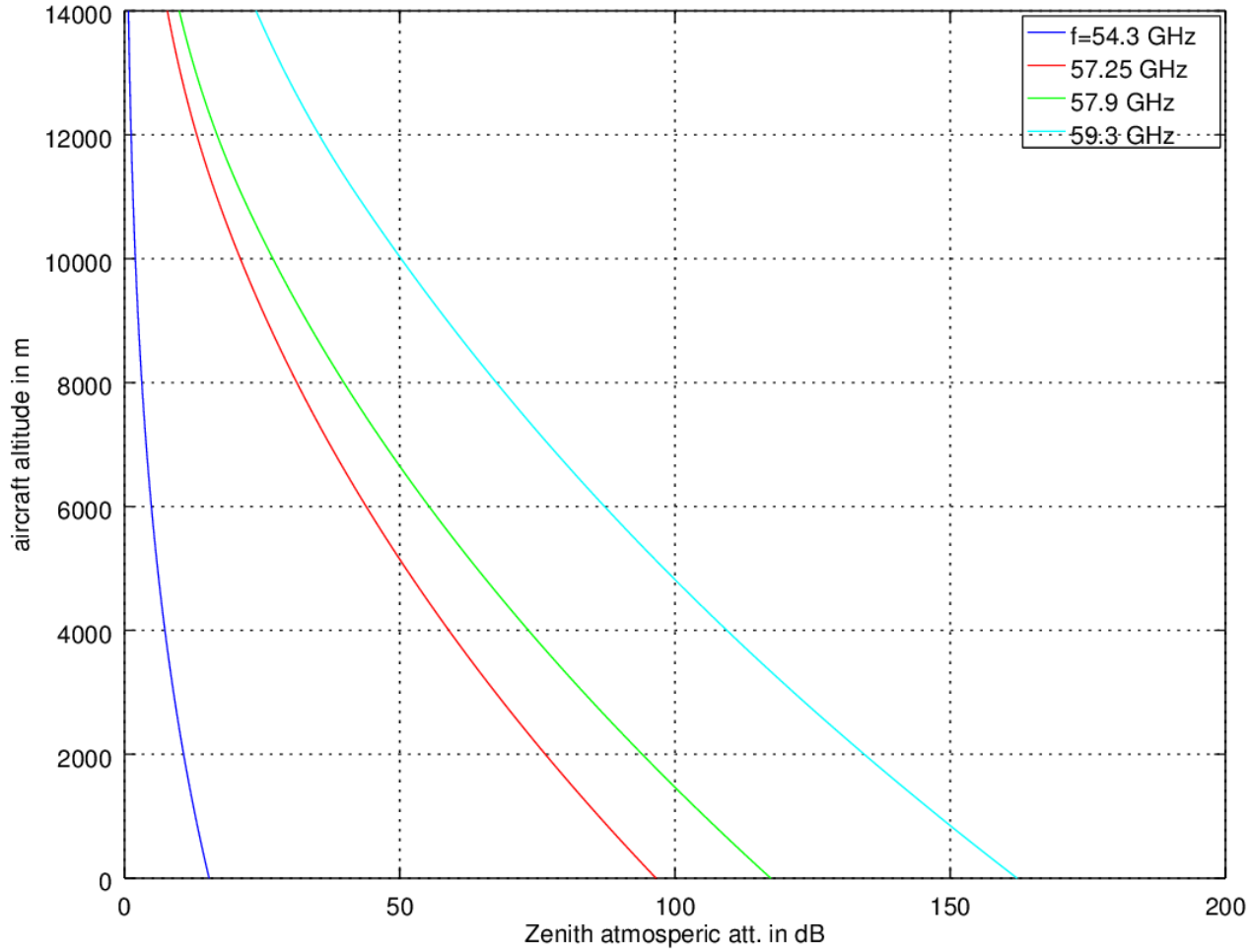

Figure 12: Dependency of Zenith atmospheric attenuation on aircraft altitude for different frequencies in the considered EESS band.

Figure 13 shows the combined atmospheric loss and total EIRP levels between 54 – 61 GHz, indicating that worst-case interference levels at the satellite are expected for frequencies close to 54.35 GHz and 57.4 GHz. Although only spurious emissions are relevant at 54.35 GHz (refer to Figure 11 for the OoB domain boundary of channel 1), low atmospheric attenuation at this frequency results in a high power level at the satellite. Further, although emissions are highest when considering in-band power levels, the peak combined channel 1 in-band power level and atmospheric loss at 57.4 GHz (where atmospheric attenuation at 14 km altitude is minimum) does not significantly exceed the emission level at 54.35 GHz. Thus, even when considering worst-case in-band transmit power, the sum interference from multiple aircraft received at the EESS satellite will be lower at 57.4 GHz due to the increased atmospheric attenuation when compared to 54.35 GHz.

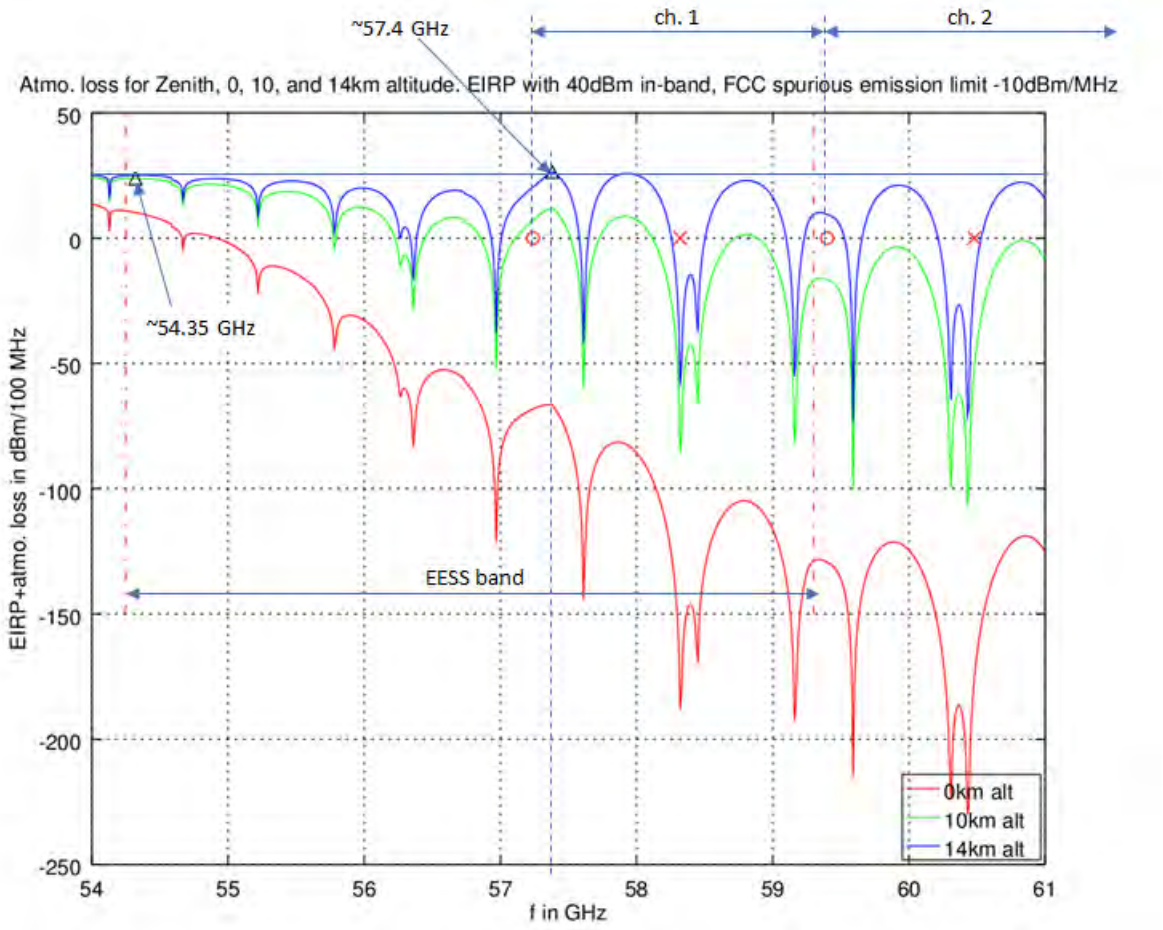

Figure 13: Combined single aircraft sum EIRP and atmospheric loss without aircraft attenuation.

2.6 Interference Assessment Results for In-Band, OOB, and Spurious Emissions

Interference from WiGig transmitters on aircraft to EESS passive sensors at the critical frequencies 54.35 GHz and 57.4 GHz is assessed in this section (a) for a worst-case single aircraft scenario and (b) based on a detailed dynamic simulation of a worst-case multiple aircraft scenario.

Detailed dynamic simulations were performed to determine if the 0.01% total interference requirement of Recommendation ITU-R RS.2017-0 [3] can be met when considering emissions from a population of aircraft distributed within the recommended reference area of 2e6 km2. (Refer to Annex F: Reference Area Definition for Dynamic Simulation and Annex I: FAA Air Traffic Data Set for details of the aircraft population and the reference area were determined.)

The dynamic simulation computes the sum interference received by the satellite from all aircraft for each time step during which the satellite sensor is active and pointed towards the reference area.

Fuselage attenuation is 40 dB following the conclusions from Annex A, Annex B, and Annex E.

An Empirical Complementary Cumulative Distribution Function (ECCDF) was then computed based on a sufficiently large number of samples of sum interference over time and compared to the applicable protection criterion of 0.01% or less for -169 dBW in 100 MHz bandwidth.

2.6.1 Worst-Case Single Aircraft at 54.35 GHz and 57.4 GHz

The frequency 54.35 GHz has the least atmospheric attenuation within the considered EESS band.

The relevant bandwidth is 100 MHz according to the bandwidth for which the ITU-R protection criterion is defined in [3]. It is assumed that parameters are constant for the 100 MHz bandwidth, taking the worst-case value at 54.35 GHz where applicable (free-space loss, atmospheric attenuation, sensor gain).

Table 5 shows that the interference protection criterion was met by a significant margin for a single aircraft, even for the worst-case assumptions of high aircraft altitude, maximum spurious emissions according to FCC limit, and minimum atmospheric attenuation.

Table 5: Worst-case single aircraft interference calculation for frequency 54.35 GHz.

Parameter	Value(s)	Comments
Aircraft alt.	14 km	
Sat. alt.	824 km	
Frequency	54.35 GHz	Frequency results in worst-case atmospheric loss
Multiple equipment factor	7 dB	Assuming 30 APs and 6 channels
Single channel spurious power	10 dBm/100 MHz	-10 dBm/MHz from [4]
Sum power, without fuselage attenuation	25 dBm/100 MHz	Sum emissions from all channels, incl. MEF, see Figure 10 at 54.35 GHz (the sum power resembles the sum spurious emissions from 30 concurrent emitters on the aircraft, each emitting at 40 dBm EIRP).
Fuselage attenuation	40 dB	Typical attenuation according to measurements and simulations
Free-space loss	185 dB	At f=54.35 GHz, alt. 14 km, ITU-R P.525 [7]
Atmospheric loss	~0 dB	At Zenith, f=54.35 GHz, alt. 14 km, ITU-R P.525 [7]
Max. sensor gain	38 dBi	At f=54.35 GHz
Receive power at sensor input, after antenna	-192 dBW/100 MHz	25 dBm - 40 dB – 185 dB -0 dB + 38 dBi = -162 dBm
Protection criterion	-169 dBW/100 MHz	ITU-R RS.2017-0 [2]
Margin	23 dB	>0 means protection criterion is met with stated margin

The second considered frequency 57.4 GHz relates to minimum atmospheric attenuation within the in-band frequency range of channel 1 (see Figure 11 and Figure 12). The atmospheric attenuation is significantly higher than at the frequency 54.35 GHz; thus, the combined emission and atmospheric attenuation yields a similar power level as for 54.35 GHz (see Figure 13).

Again, the considered bandwidth is 100 MHz according to the bandwidth for which the ITU-R protection criterion is defined. It is assumed that parameters are constant for the 100 MHz bandwidth, taking values at 57.4 GHz where applicable for free-space loss, atmospheric attenuation and sensor gain.

As previously indicated in Figure 13, the resulting interference level at 57.4 GHz is very close to the interference level due to spurious emissions at 54.35 GHz. When Table 5 and Table 6 are compared it can be seen that the significant margin of 24 dB is almost the same as for 54.35 GHz (10 dB higher EIRP is more than compensated by the 11 dB higher combined atmospheric and free-space loss).

Table 6: Worst-case single aircraft interference calculation for frequency 57.4 GHz (highlighting shows differences to Table 5).

Parameter	Value(s)	Comments
Aircraft alt.	14 km	
Sat. alt.	824 km	
Frequency	57.4 GHz	
Multiple equipment factor	7 dB	
Single channel spurious power	10 dBm/100 MHz	-10 dBm/MHz from [15]
Sum power, without fuselage attenuation	35 dBm/100 MHz	Sum emissions from all channels, incl. MEF, see Figure 10 at 57.4 GHz (with channel 1 in-band emissions at 27.3 dBm/100MHz dominating OoB and spurious emissions from all other channels, the 35 dBm/100MHz mainly correspond to the sum in-band emissions from 5 concurrent emitters in channel 1 on the aircraft each emitting at 40 dBm).
Fuselage attenuation	40 dB	Attenuation according to measurements and simulations
Free-space loss	186 dB	At f=57.4 GHz, alt. 14 km, ITU-R P.525 [7]
Atmospheric loss	10 dB	At Zenith, f=57.4 GHz, alt. 14 km ITU-R P.676-11 [7]
Max. sensor gain	38 dBi	At f=57.4 GHz
Receive power at sensor input, after antenna	-193 dBW/100 MHz	35 dBm - 40 dB – 186 dB -10 dB + 38 dBi = -163dBm
Protection criterion	-169 dBW/100 MHz	ITU-R RS.2017-0 [2]
Margin	24 dB	>0 means protection criterion is met with stated margin

Dynamic simulations of the scenario were performed for the considered frequencies to assess the impact of interference from a large number of aircraft in the reference area. The results of that simulation are presented in the next section.

2.6.2 Dynamic Simulation for Peak Air Traffic 54.35 GHz and 57.4 GHz

The single aircraft assessment above shows that the interference protection threshold is maintained with large margins of at least 23 dB for 54.35 GHz and 57.4 GHz, respectively, even assuming worst-case conditions with respect to in-band and spurious emission levels, atmospheric attenuation, and realistic fuselage attenuation.

As described above and in the annexes, a detailed dynamic simulation is performed to assess the impact of the large number of aircraft within the required reference area to obtain an accurate interference statistics to compare with the applicable ITU protection criteria.

The dynamic simulations include realistic modeling of fuselage attenuation and it will be shown below that required interference limits are maintained in all cases.

Parameters used in the dynamic simulation are summarized in the Table 7 below.

Table 7: Key parameters used in the dynamic simulation for frequencies 54.35 GHz and 57.4 GHz.

Parameter	Value(s)	Comments
Time step	20 ms	Provides for a sufficiently dense sampling pattern of the scanning sensor across the reference area.
Simulated time (considering only time steps during which sensor is active and directed to reference area)	7 days (~ 600 s)	Corresponds to multiple satellite fly-overs and approx. 30,000 scan points in the reference area
Aircraft positions	From FAA data, altitude varies from 0 to approx. 14 km	Based on FAA data for peak traffic time in 2016
Sat. alt.	824 km	Orbit ephemeris data is imported from STK
Frequencies	54.35 GHz, 57.4 GHz	Frequencies results in minimum atmospheric losses and maximum OOB emissions in K2 EESS frequency range following 802.11-2016 DMG transmit mask
Multiple equipment factor	7 dB	Assuming 30 APs and 6 channels
Fuselage attenuation	40 dB	From measurements and simulations
Sum power, without fuselage attenuation	25 dBm/100 MHz at 54.35 GHz, 35 dBm/100 MHz at 57.4 GHz	See Figure 10
Free-space loss	Depending on satellite and aircraft position	Computed each time step in dynamic simulation
Atmospheric loss	Depending on satellite and aircraft position	Computed each time step in dynamic simulation following ITU-R P.676-11 [8]
Max. sensor gain	38 dBi	
Sensor gain	Depending on satellite and aircraft position and on sensor scan angle	Computed each time step in dynamic simulation following ITU-R RS.1813-1 [9]
Receive power at sensor input, after antenna	Depends on satellite and aircraft position	Computed each time step in dynamic simulation per aircraft as function of emitted power, free-space loss, atmospheric loss and antenna gain.
Protection criterion	-169 dBW/100 MHz at 0.01% or less	ITU-R RS.2017-0 [3]

The ECCDF derived from the dynamic simulations show that the impact of multiple aircraft within the sensor beam is small (see Figure 14 and Figure 15).

Even at 54.35 GHz, where atmospheric attenuation is minimum within the EESS band, the increase of interference due to multiple aircraft amounts only to approx. 5 dB at 0.01% compared to the single aircraft worst-case (see Figure 13).

Thus, the protection criterion is met for the worst-case frequency 54.35 GHz with a margin very close to the 23 dB margin obtained for the worst-case single aircraft scenario (see margin obtained in Table 5).

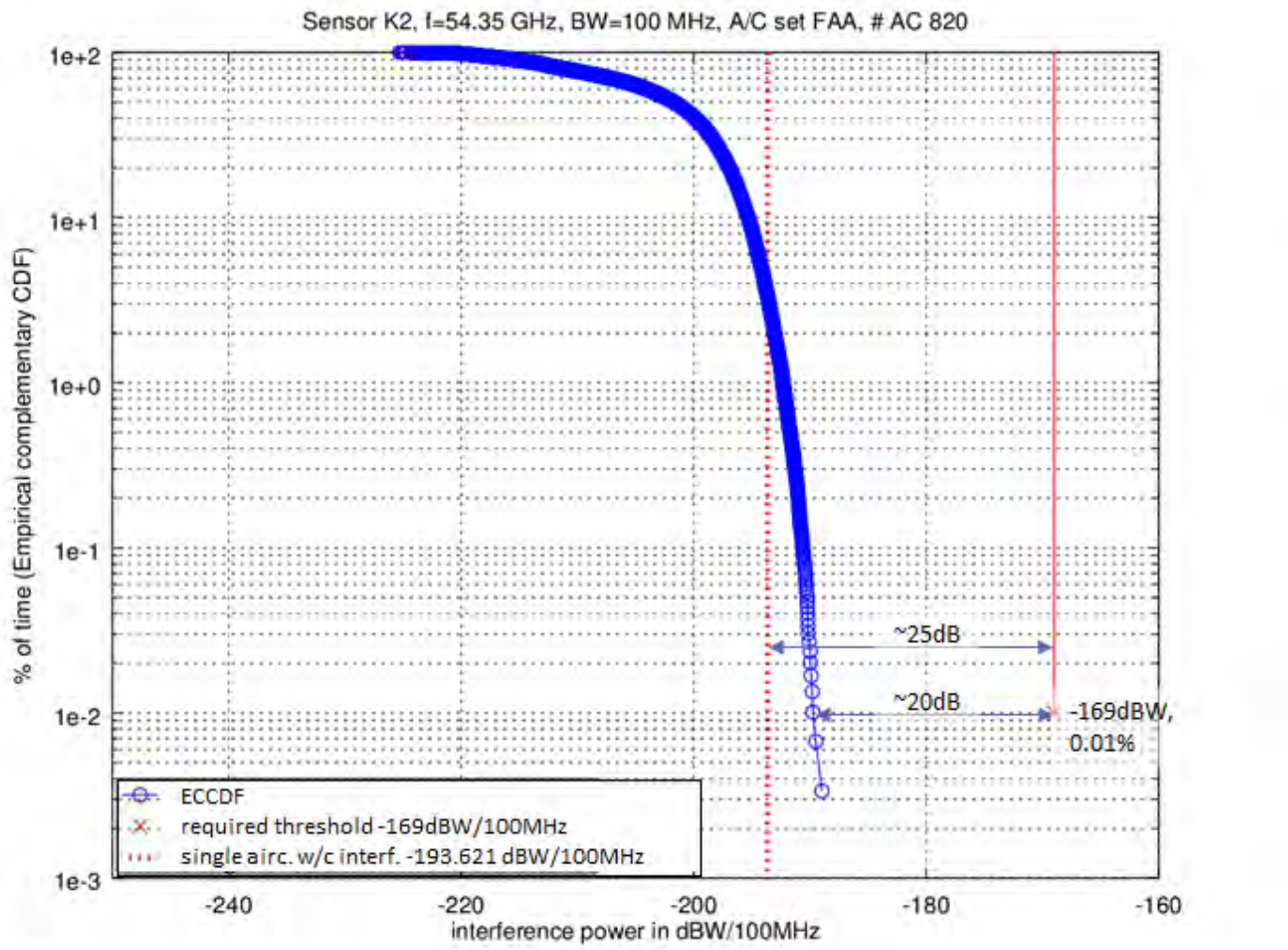

Figure 14: ECCDF from dynamic simulation of sensor K2, 25 dBm/100 MHz at 54.35 GHz.

As expected, the dynamic simulation for 57.4 GHz shows a significantly reduced impact of multiple aircraft because interference from aircraft at lower frequencies is heavily attenuated due to high atmospheric attenuation at that frequency, see Figure 12.

Thus, for 57.4 GHz a significant margin of approx. 24 dB can be maintained for the multiple aircraft case as for the single aircraft worst-case (see Table 6), even considering high in-band power levels from channel 1 usage.

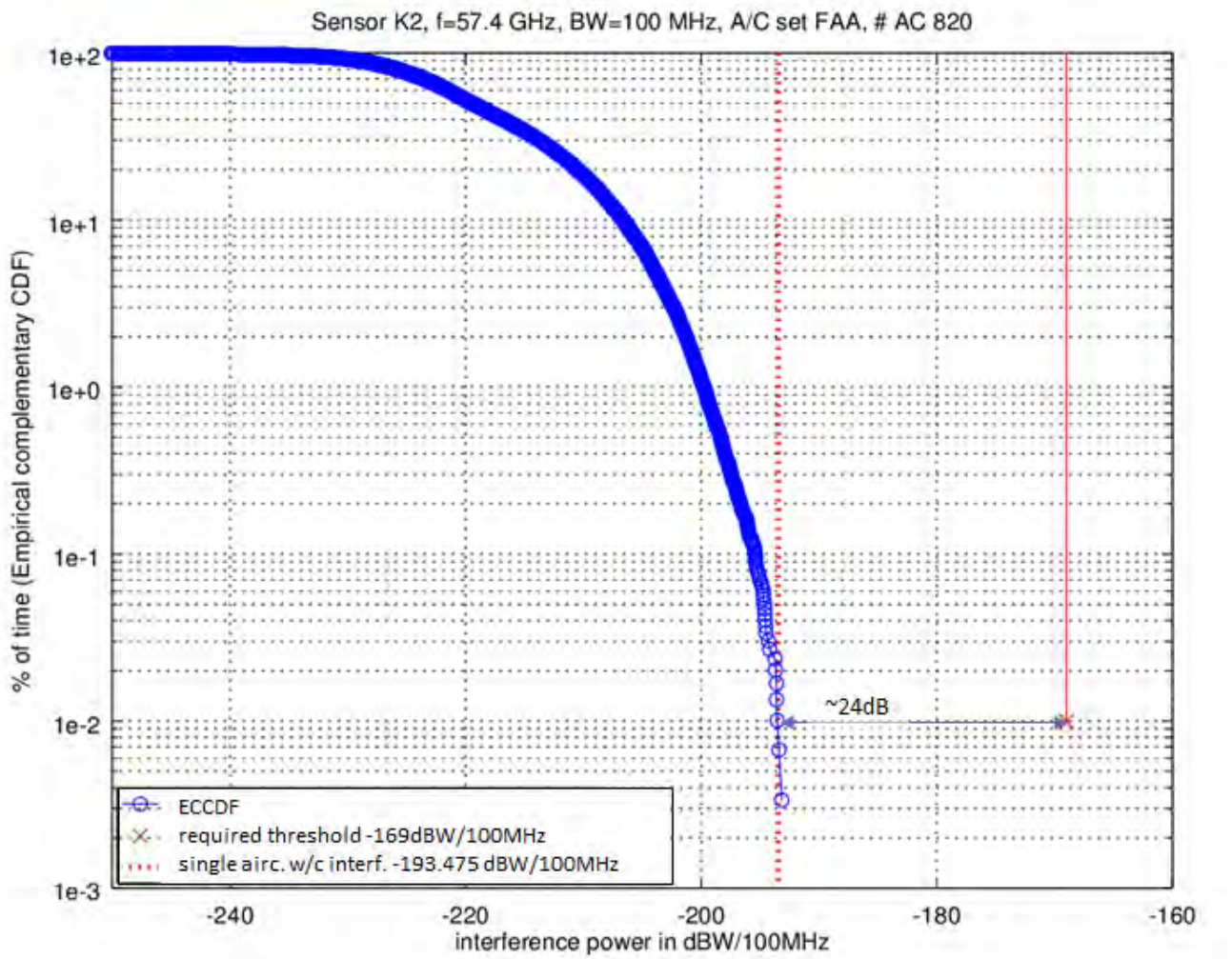

Figure 15: ECCDF from dynamic simulation of sensor K2, 35 dBm/100 MHz at 57.4 GHz.

3 Conclusion

The worst-case analyses above show that the required interference protection threshold is met with a significant margin, even when considering worst-case spurious emissions at minimum atmospheric losses and channel 1 in-band emissions. Thus, it is concluded that any emissions from WiGig equipment operated onboard aircraft do not pose a threat to EESS passive services.

4 Acknowledgements

AVSI wishes to acknowledge the enthusiastic contributions and invaluable expertise of its AFE 85 participants:

Reza Arefi	Intel
Matthew Carrico	Rockwell Collins
Wayne Cooper	The Boeing Company
Joseph Cramer	The Boeing Company
Mehdi Izadyar	Panasonic Avionics Corporation
Jeffrey Jost	The Boeing Company
Kim Kolb	The Boeing Company
Dennis Lewis	The Boeing Company
Oliver Lücke	Zodiac Inflight Innovations
Nazih Khaouly	Federal Aviation Administration
Anil Kumar	Boeing
Mike Paglione	Federal Aviation Administration
David Redman	AVSI
Steven Rines (Project Lead)	Zodiac Inflight Innovations
Manny Rios	Federal Aviation Administration
John Roman	Intel
Uwe Schwark	Airbus
Jayne Stancavage	Intel
Joe Storniolo	Panasonic Avionics Corporation
David Walen	Federal Aviation Administration
Hassan Yaghoobi	Intel

A: WiGig Aircraft Emissions Model

This annex provides a WiGig aircraft emissions model. Details regarding use cases, overall methodology, development tools, correlation of development tools with various measurements, detailed simulation results and finally a general aircraft radiation model are provided. The aircraft emissions model may be considered in terms of fair field gain or in terms of an effective aircraft attenuation. It will be shown that the expected value of effective aircraft attenuation is largely independent of the location and gain of the directional antenna utilized by WiGig devices. Simulations and ultimately the aircraft emissions model presented in this annex consider all WiGig beam steering angles based on various use cases and implementations. This includes cases where aircraft windows are fully, partially and non-illuminated. Simulations and measurements are in close agreement and indicate that the expected effective aircraft attenuation is approximately 40 dB. In the event the expected value of effective aircraft attenuation is insufficient, simulation data is fitted to a general X2 distribution. Detailed model definition and variable parameters are provided in section A.6.2 Gain and Effective Attenuation Statistical Model.

A.1 Introduction

This annex provides a WiGig aircraft emissions model based on analyses of ray tracing simulation results from various use cases and implementations. This annex also includes background and model development details that support the use of ray tracing tools and the resulting conclusions.

Topics and organization:

- An overview of WiGig on-aircraft use cases.
- A brief description of WiGig and beam steering.
- An overview of the aircraft emissions model development including correlation with laboratory and on-aircraft measurements.
- WiGig phased array antennas and steering angles.
- Simulation results and analyses for WiGig access point use cases with various antenna implementations and a PED use case.
- A general aircraft emissions model definition in terms of gain as well as effective aircraft attenuation.

A.2 Overview of WiGig On-Aircraft Use Cases

Various WiGig on-aircraft use cases are anticipated. These use cases may be lumped into two broad categories based on mobility: fixed and nomadic. Both fixed and nomadic use cases will require high gain antennas in order to achieve multi-gigabit data rates in the 60 GHz WiGig band. Nomadic use cases will require adaptive beam steering technology to maintain a connection and achieve the highest available throughput. Fixed use cases on the other hand may utilize non-adaptive antenna technology such as an antenna array with fixed element weighting factors, horn antennas, etc. This differentiation in antenna technology is an important distinction when considering use cases and the scope of the aircraft emissions MODELING effort. Details on potential use cases are provided in the sections that follow.

A.2.1 Nomadic Use Cases

Nomadic use cases may employ WiGig for distribution of content to IFE seat back displays, passenger provided PEDs, etc. Example use cases are presented in the figures below.

Figure A.1 and Figure A.2 depict a connection between a WiGig access point and seat monitors. This use case is considered nomadic since the seats may be repositioned by passengers. Further, there may be passenger activity around the seat monitors forcing the access point and seat back WiGig devices to re-optimize antenna steering angles.

Figure A.3 depicts a connection between a WiGig access point and passenger PEDs. Clearly passenger PEDs are not fixed, and therefore may be considered nomadic. Similar to the access point and seat monitor use case, antenna steering angle optimization will be required.

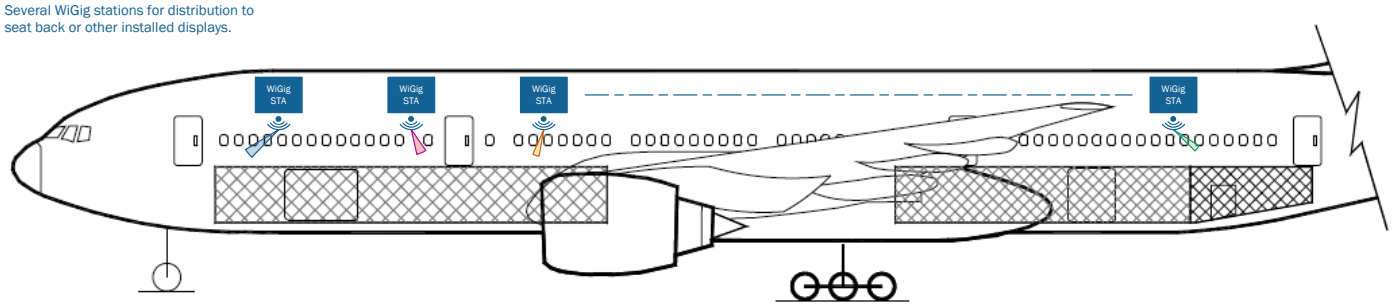

Figure A.1: WiGig distribution to seatback displays.

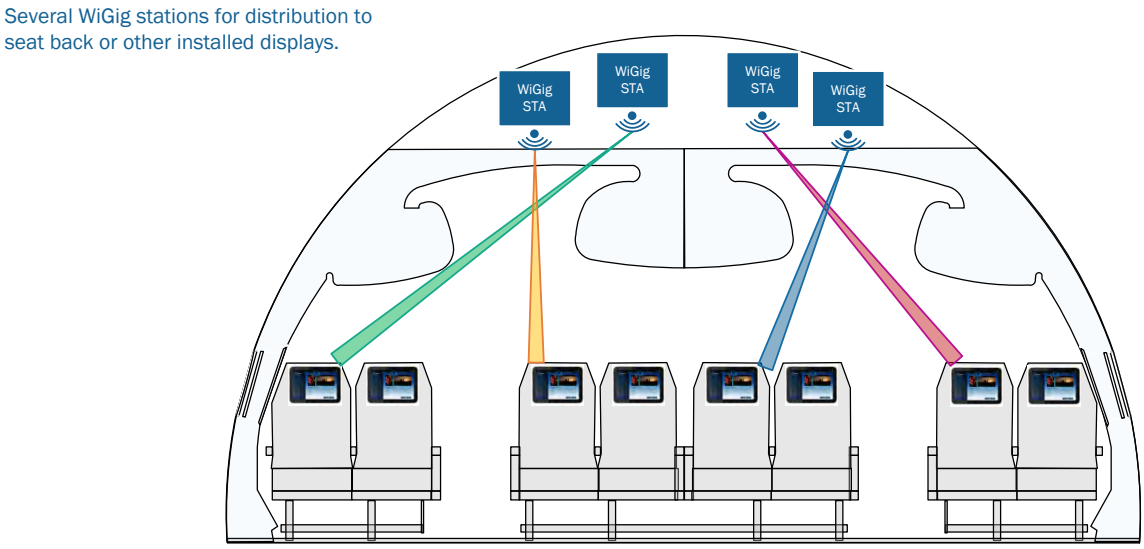

Figure A.2: WiGig distribution to seatback displays (cross-section).

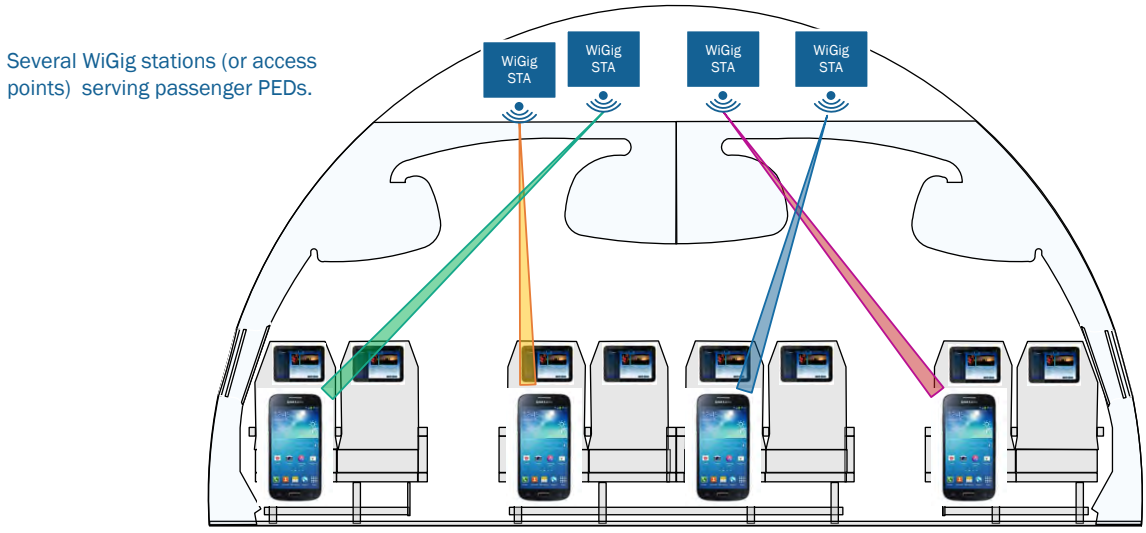

Figure A.3: WiGig and PEDs.

A.2.2 Fixed Use Cases

WiGig may be utilized for backbone connections along the length of an aircraft. Figure A.4 depicts a sample WiGig backbone architecture. Since this use case provides connectivity down the length of the aircraft, it is likely that high gain antennas with a fixed beam direction will be utilized.

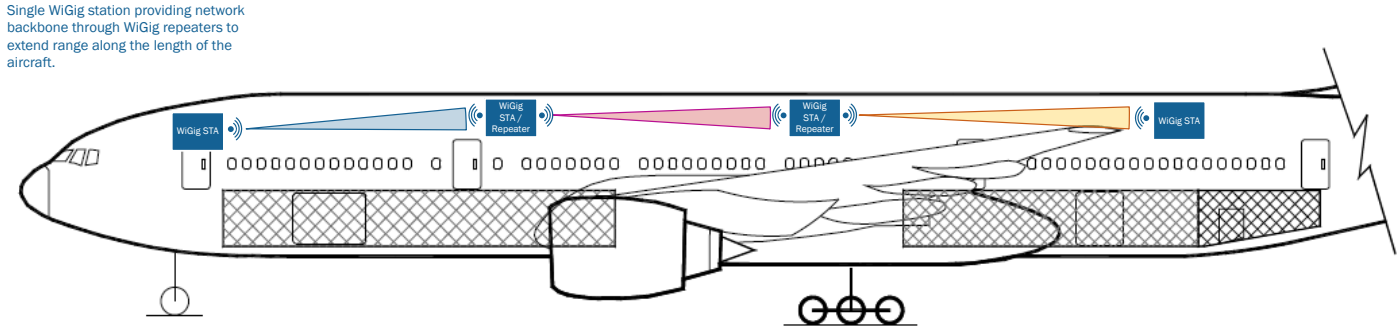

Figure A.4: WiGig backbone utilizing relays or repeaters.

A.2.3 Use Case Summary

Three sample WiGig on-aircraft use cases were provided and split into two broad categories: fixed and nomadic. Since fixed use cases will utilize a set beam direction along the length of the aircraft, it is highly unlikely that antennas will point directly towards windows which provide little to no transmission attenuation. Nomadic use cases on the other hand must utilize steerable antenna technology. It is probable that the steerable antenna will point toward an aircraft window (even if momentarily) and will contribute to the power radiated from the aircraft in the 60 GHz WiGig band. Given that fixed use cases will not contribute significantly to the power radiate by from the aircraft, only nomadic use cases are considered in the development of an aircraft emissions model.

A.3 A Brief Description of WiGig and Beam Steering

WiGig 802.11 ad operates in the unlicensed 57 to 71 GHz frequency band and includes a channel bandwidth of 2.16 GHz. Given a free space path loss of approximately 90 dB at 10 m, a relatively low conducted transmit power capability at 60 GHz and a transmission bandwidth of approximately 1.84 GHz, high gain transmit and receive antennas are required to maintain high rate communication links. WiGig use cases often are nomadic, implying that steerable antennas on the transmit and / or receive sides of the WiGig link are required. Therefore beam steering antenna technology is included in the

802.11 ad WiGig standards. A general understanding of beam steering operation for WiGig is key to development of aircraft emissions models.

A.3.1 WiGig Beam Steering Overview

The 802.11 ad standards provide several details on DMG channel access and beam steering. Since window transmission attenuation is expected to be near 0 dB, the main area of concern in the development of an aircraft emissions model with WiGig on board is the direction of the beam. Two states may be considered: the connected state where one WiGig device has packets specifically for another WiGig device; the training state where adaptive beam former training is being performed by the WiGig access point and / or client device.

In the connected state, beam direction will depend on many random variables. For example:

- The location of a PED is random within the confines of the aircraft cabin and will vary with time on any given flight. Similarly, a seat back monitor position is random within some physical limits and will vary during flight.
- The location of access points will vary by aircraft type design and may be considered random.
- Passengers acting as blockers or in some cases reflectors will also impact beam steering angles of WiGig devices, and passenger locations in the cabin are random.
- Note that optimal beam steering angles may result in zero to three or more bounces off highly reflective materials in order to provide the highest quality link. The number of bounces, though related to physical location of WiGig devices and physical blockers or reflectors is also a random variable.

In the training state, the access point and / or client device perform a sweep over some set of steering angles. The access point and client device determine their respective steering angles for optimum link quality. If a client device moves, beam training may again be required to optimize link quality. Similar to the connected state, the steering angle of a WiGig device during the training state is considered random since it is implementation specific.

Given the number of random variables in both the connected and training states, it is clear that the beam steering angle of any WiGig device supporting nomadic use cases is also random. It is assumed in this paper that the beam steering angles follow a uniform random probability. For example: If there are 37 possible steering angles, then each steering angle is assumed to be equally probable. Simulations are performed over all steering angles and the far field gain statistics are calculated. Further details on model development are provided in section A.1.4.

A.3.2 Sample WiGig Beam Steering Antennas

WiGig devices intended for nomadic use cases will utilize phased array antenna technology. The dimensions of the antenna array and the underlying antenna elements vary between implementations. Typical antenna arrays utilize patch antennas arranged in either a 2 x 8 or 4 x 8 array. A 2 x 8 array of patch antennas is expected to yield a fan beam pattern with HPBW of 57 x 14 degrees. A 4 x 8 patch array will yield a HPBW approximately 29 x 14 degrees. Certainly other configurations are possible, especially as WiGig integration into various devices evolves. Two types of antennas are considered in simulations. This includes a circular symmetric 30-degree HPBW antenna and a fan 57 x 14 degree fan beam antenna.

A.4 Overview of WiGig Aircraft Emission Model Development

Use cases and a brief description of WiGig beam steering have been provided. Understanding these use cases and the basics of WiGig beam steering are crucial in the development of an aircraft emissions model. It is especially important to consider the randomness of the beam steering angles, the types of antennas and device locations. An additional random variable is the orientation between the aircraft and satellite sensors. It is clear that there are a large number of random variables, and therefore the approach to modeling aircraft emissions must be statistical. Attempting to define a closed form deterministic model of aircraft emissions given the large number of random variables is impractical.

Generating a significant set of data for statistical analysis is also challenging. Aircraft are not readily available, and exercising the large number of random variables in an aircraft measurement environment is intractable. Therefore ray tracing simulation is used in conjunction with some limited number of on-aircraft measurements to attain a statistical model of aircraft emissions. The ray tracing simulations assume a Boeing 777-200 aircraft. In order to keep ray tracing simulation times reasonable (days rather than weeks), cabin details such as seats, stowage bins, galleys, etc. were omitted from the model. A complex permittivity was assigned to the skin of the aircraft to replicate the effects of cabin interiors. This complex permittivity provides a bulk dampening effect on the large number of potential reflections and natural modes of resonance from the aircraft fuselage. The simulations yield far field gain over 4π steradians in one-degree increments.

Since the orientation of the aircraft relative to EESS and RAS sensors, location of WiGig devices, etc. are all random variables, the approach is to generate histograms of far field gain over all far field observation angles for a given use case or antenna location. A common probability density function is then fit to the histograms of simulated far field gain predicted by ray tracing simulations. This predicted fair field gain is also used to determine an average effective attenuation of the aircraft, where the average effective attenuation is the difference between the peak antenna gain and the expected value of far field gain given aircraft blockage and scattering effects.

A.4.1 Simulation Tools and Correlation with Measured Data

Ansys Savant was used for ray tracing simulations, and Matlab was used for pre and post processing wherever necessary. SolidWorks was used for preparing 3D mechanical models of various structures as needed.

This section provides two sets of correlation data:

- Aircraft window attenuation measurements were conducted to validate the assumption that windows without electronic shading provide little to no direct attenuation and ray tracing simulation results are compared with these measurements.
- Emissions and attenuation measurements were performed on a Boeing 777-200 in Marana, AZ as reported in Annex B: In-Aircraft Emissions Testing.
- Ray tracing simulation results are compared with measurement results to determine the accuracy of ray tracing predictions.

A.4.2 Correlation with “60 GHz Aircraft Window Testing”

A series of measurements aimed at confirming the attenuation of an aircraft window without electronic shading was performed. The goal of these measurements was to determine the transmission loss through such a window at 60 GHz. An aircraft window was placed in a large section of aluminum sheet metal to replicate a portion of an aircraft fuselage. Figure A.5 depicts the test setup. The test setup includes a transmitter that can be seen through the window, the emulated fuselage section with

aircraft window, and a receiver, which can be seen closet to the camera position. The fuselage section with window and receiver are mounted on a turntable.

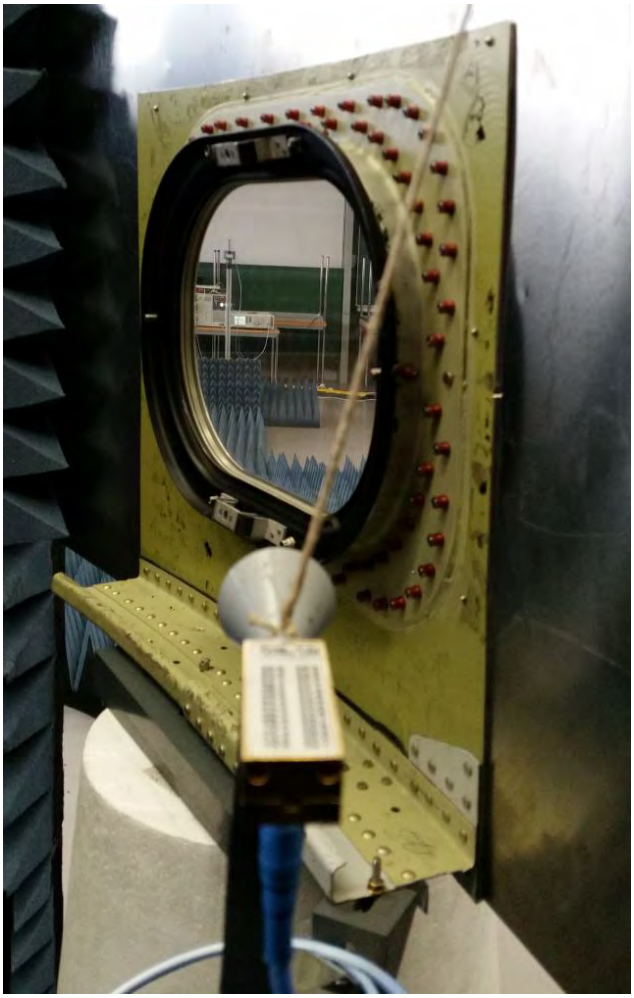

Figure A.5: Aircraft window test setup.

Three receiver positions relative to the window were tested. These are depicted in Figure A.6 and Figure A.7.

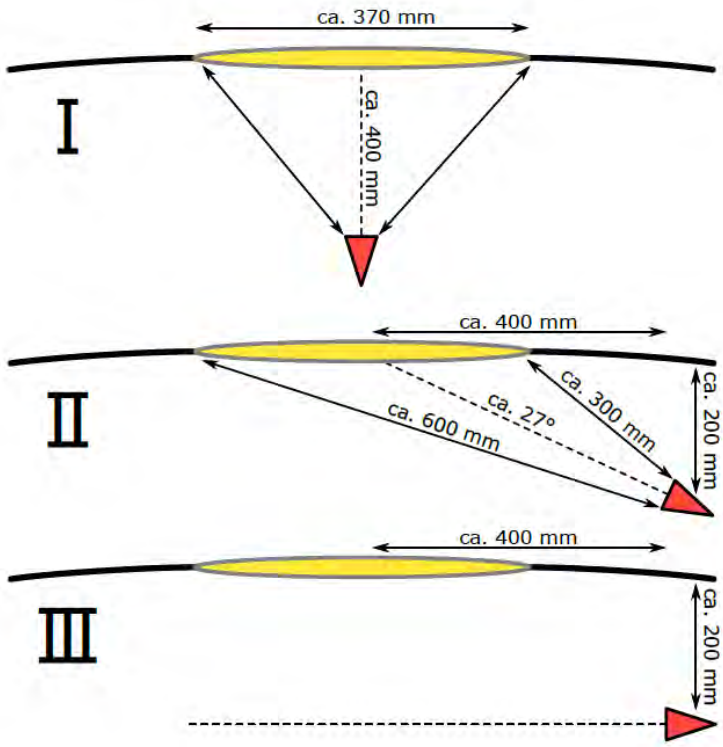

Figure A.6: Measurement scenarios.

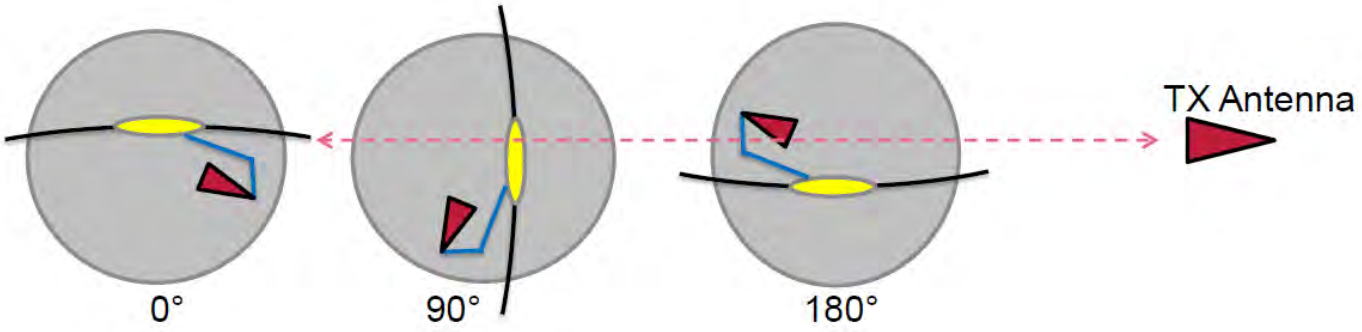

Figure A.7: Measurement scenarios (alternate view).

The measurement results are depicted in Figure A.8 and Figure A.9. Figure A.8 shows that the window provides little to no transmission attenuation. It also provides an indication of the receive antenna half power beam width (HPBW) of approximately 12 degrees. Based on this HPBW, the peak gain of the conical horn antenna is expected to be approximately 23 to 24 dBi.

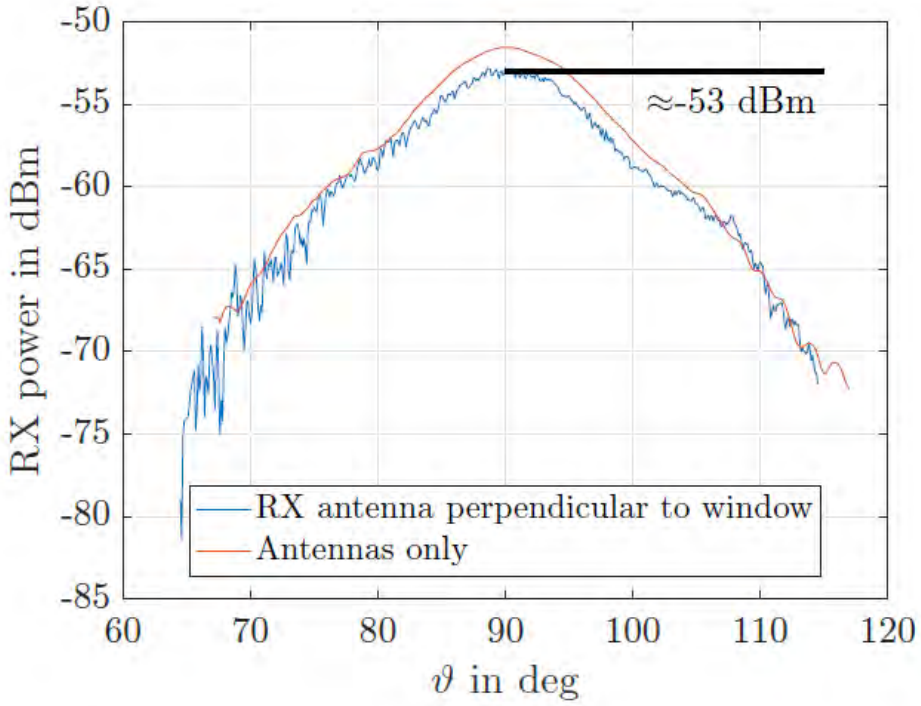

Figure A.8: Measurements results for measurement scenario depicted in Figure A.6.

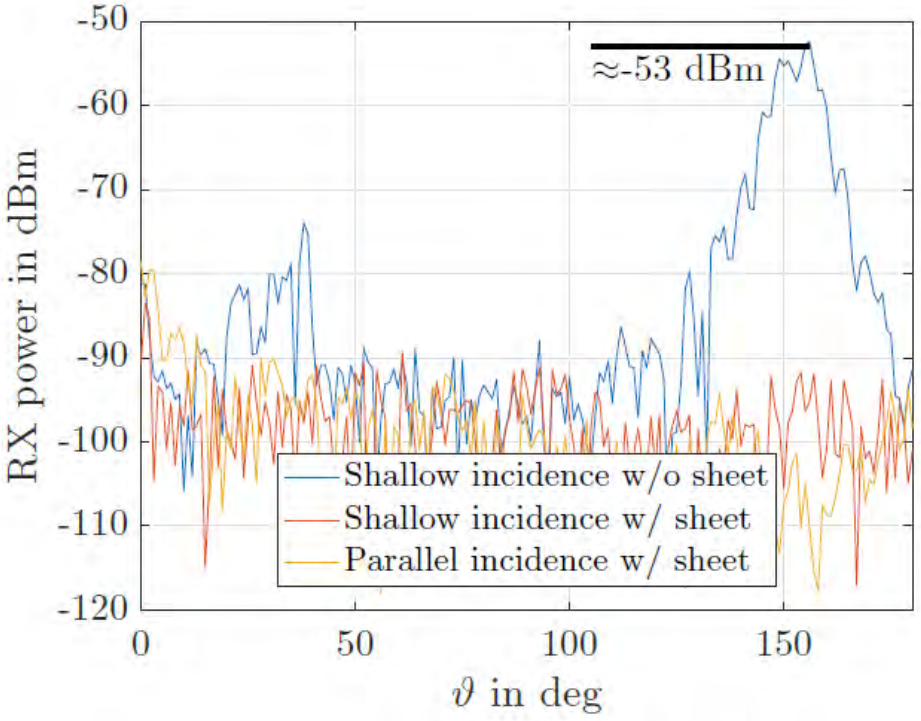

Figure A.9: Measurement results for measurement Scenario II depicted in Figure A.6.
Measurements were made with and without a metal sheet covering the window.

A Savant simulation model was developed for correlation purposes. Figure A.10 and Figure A.11 depict a side and top view of the Savant ray tracing model. Figure A.12 and Figure A.13 provide simulation results. The simulated HPBW is approximately 10 degrees and slightly narrower than what

was estimated from the measurements. This was considered relatively minor and was not expected to have a significant impact on simulation results.

Comparing Figure A.9 and Figure A.13 is of particular interest. The simulation and measurement results share many characteristics. In particular they both show a narrowing of the main beam and a 10 dB beam width of roughly 15 degrees. The general shape of the measured and simulated responses are quite similar. The only significant difference between measured and simulated responses occurs at roughly 125 degrees off the peak power or peak gain point. The measured data indicates the power is roughly 21 dB below the peak, while the simulations show 40 dB below peak. This is most likely due to mechanical features such as the rib (Figure A.5) that was present in measurements but not in simulations.

Overall, the simulated and measured results are very similar. This lends credence to the use of Ansys Savant for aircraft radiation model development. However, this set of simulations and correlation data does not excite the natural resonances, reflections and dampening effects of an aircraft cabin. Therefore additional correlation points are desired. Section A.4.3 provides additional correlation with on-aircraft measurements documented in Annex B: In-Aircraft Emissions Testing and Annex E: Aircraft Fuselage Attenuation Testing.

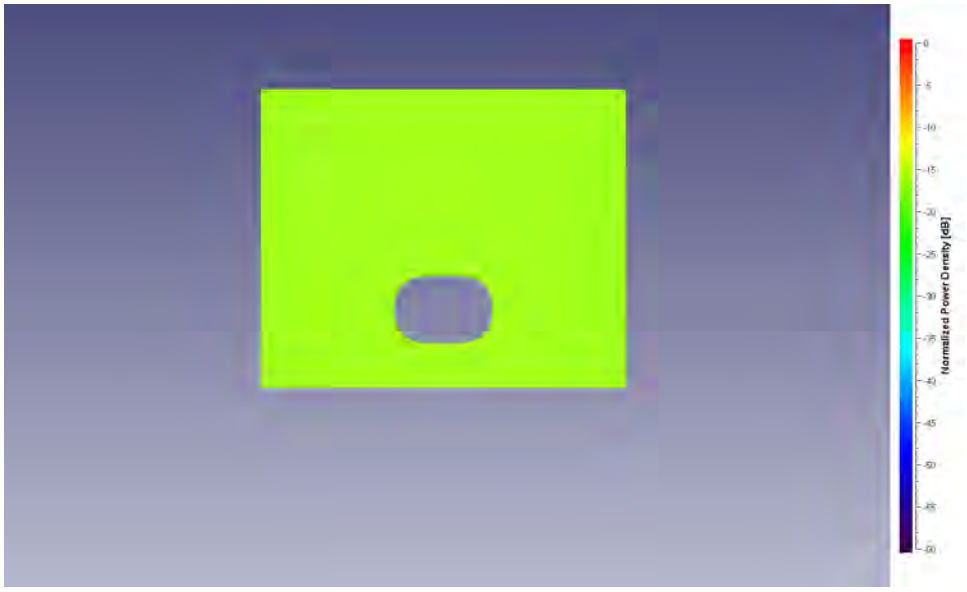

Figure A.10: Side view of Ansys Savant model approximating the measurement setup.

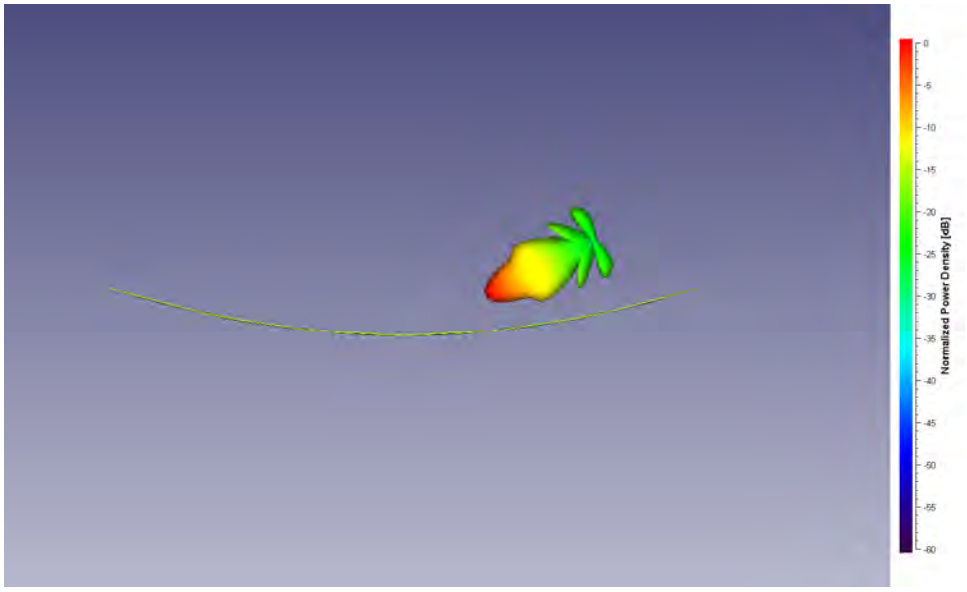

Figure A.11: Top view of Ansys Savant model approximating the measurement setup.

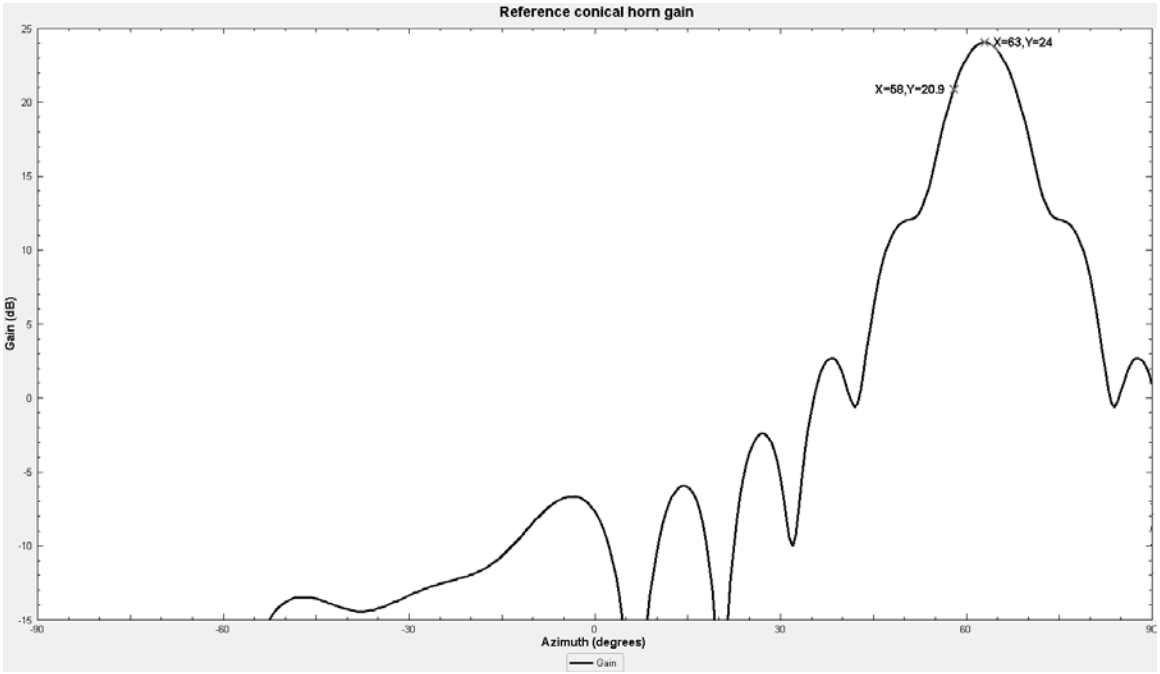

Figure A.12: Simulated gain of the transmit antenna without the fuselage section.
The HPBW of the simulated antenna is approximately 10 degrees.

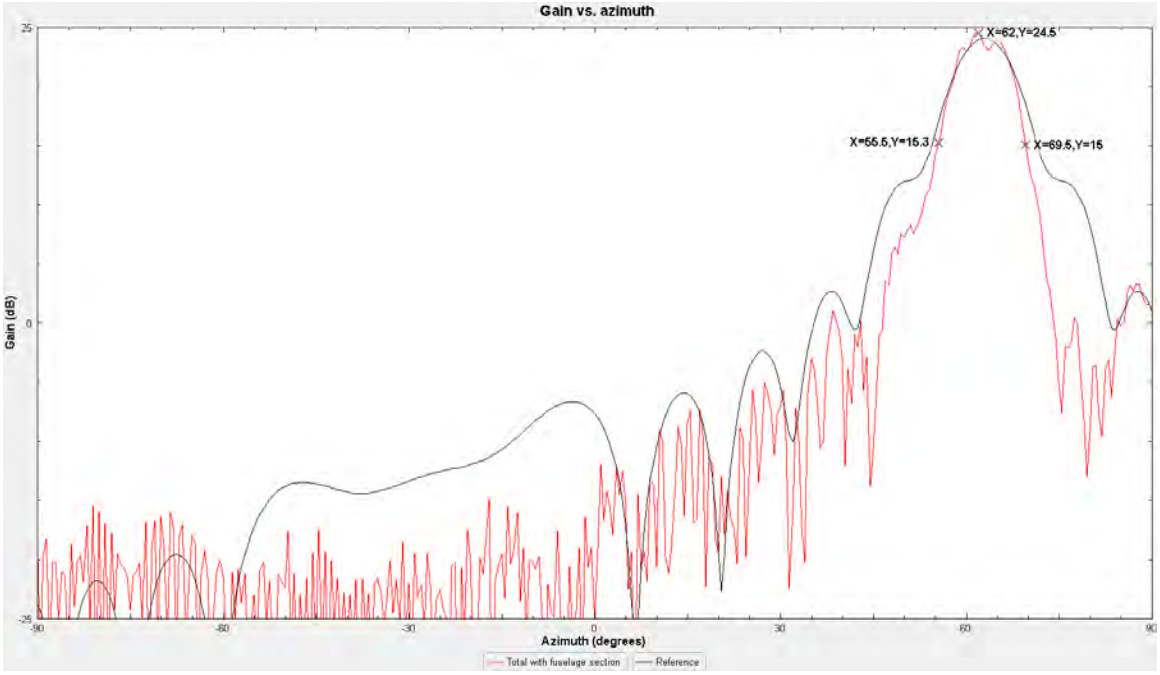

Figure A.13: Simulated gain of the transmit antenna with (red) and without (black) the fuselage section.

A.4.3 Correlation with On-Aircraft Measurements

Section A.4.1 showed very good correlation between Ansys Savant simulations and the measurements. This certainly worked well for determining window attenuation and lends credence to the use of Ansys Savant for predicting aircraft radiation at 60 GHz for various use cases. However, an aircraft cabin is a much more complicated scenario. The simplest analysis would consist of an aircraft modeled simply as a metallic tube with apertures (windows) and various dampening materials. The challenge is to determine the bulk dampening effect of cabin materials, such as seats, insulation, luggage containers to name a few, and ultimately assign a bulk lossy, complex relative dielectric constant to the aircraft fuselage for the purposes of relatively simple modeling. A second set of correlation measurements were therefore required, but this time on an aircraft.

A.4.4 On-Aircraft Measurement Summary

On-aircraft measurements were performed on a Boeing 777-200 in Marana, AZ. Aircraft emissions test results are documented in Annex B: In-Aircraft Emissions Testing and Annex E: Aircraft Fuselage Attenuation Testing.

Figure A.14 depicts the on-aircraft test concept. A transmitter with a conical horn antenna was placed inside the aircraft. The horn antenna pointed towards a window at a reference location (seat 12J) on the starboard side of the aircraft. A receiver with a conical horn antenna was placed outside the aircraft on a scissor lift. The receiver horn antenna was pointed directly at the window at seat 12J. Received power was recorded over frequency for 12 transmitter orientations as depicted in Figure A.14.

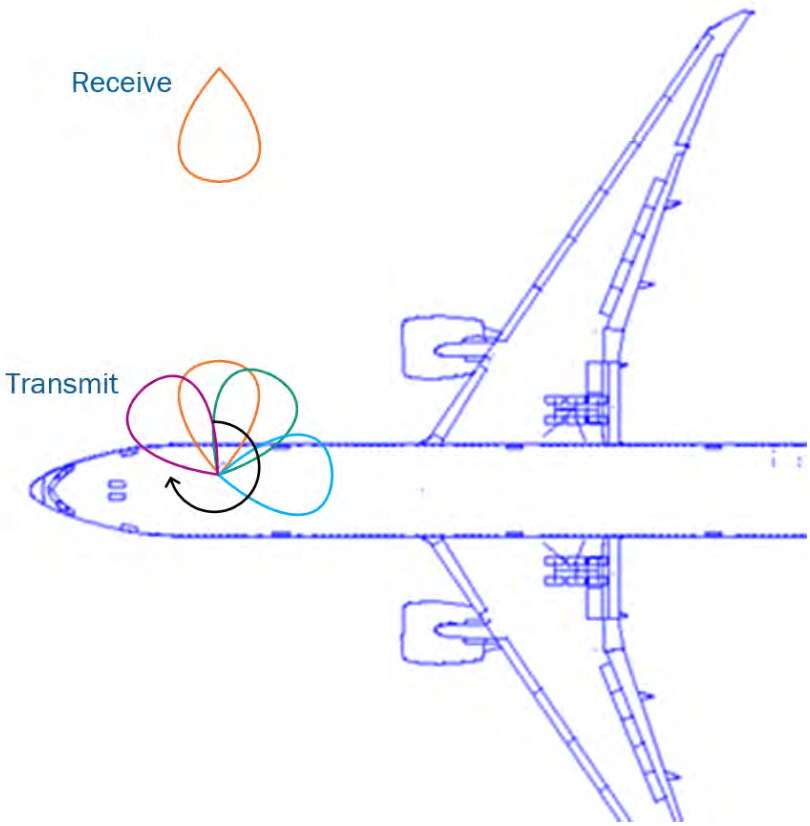

Figure A.14: On-aircraft test concept.

Figure A.15 depicts a subset of measurements at seat 12J. These measurements include:

- Transmit pointing through the window at seat 12J directly at the receiver on a scissor lift. The transmit and receive sections were visually aligned on boresight and co-polarized.
- Transmit pointing orthogonal to receive (90 degrees) and towards the tail of the aircraft.
- Transmit pointing directly opposite of receive (180 degrees) and towards the port sized of the aircraft.
- Transmit pointing orthogonal to receive (270 degrees) and towards the nose of the aircraft.
- A reference, open door measurement.

Note: Open starboard door reference measurements depicted in Figure A.15 were collected at a frequency step size of 0.1 GHz. Measurements at seat 12J were collected with a frequency step size of 0.01 GHz.

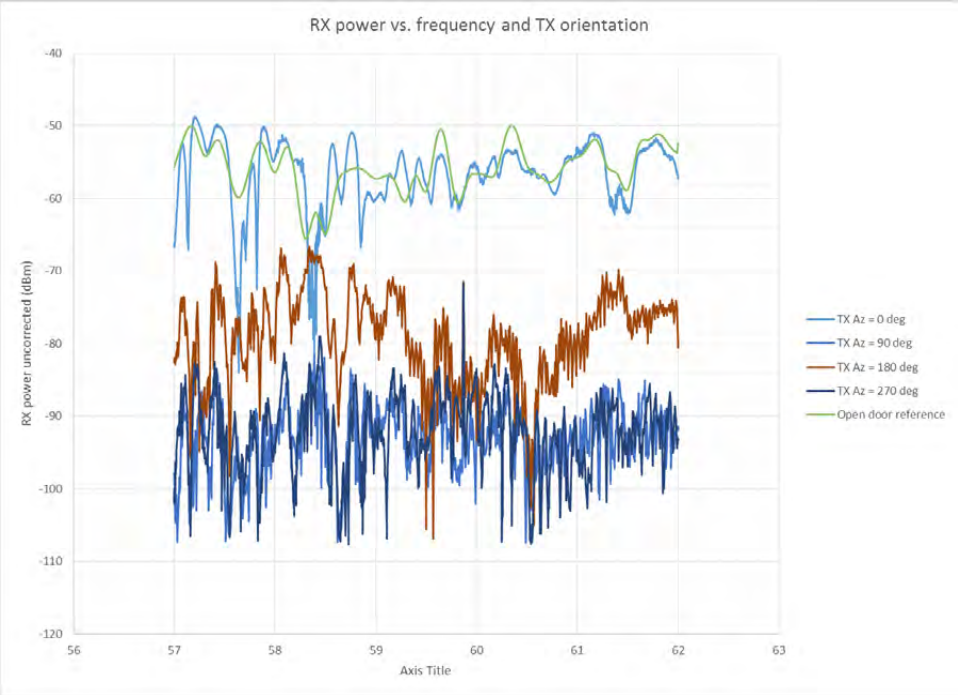

Figure A.15: RX power vs. frequency and transmit antenna orientation.
Measurement data is provided through an open starboard door as well as seat 12J.

Table A.1 provides a summary of the average difference between measurements at seat 12J vs. transmit azimuth angle. The difference is relative to the measurements at a transmit azimuth angle of 0 degrees; i.e. aligned and co-polarized with the receive antenna outside the aircraft.

Table A.1: Average difference between measured receive power at a transmit azimuth angle of 0 degrees (aligned with receive antenna boresight) and a sweep of transmit azimuth angles.

TX Azimuth (deg)	12J measured average delta (dB)
30	24.5
60	39
90	40.5
120	41.6
150	44.4
180	30
210	38.9
240	44.6
270	40.5
300	41
330	28.9

A.4.5 Seat 12J Simulation Results

The Boeing 777-200 measurements at seat 12J were replicated in Ansys Savant. One of the first steps in replicating the measurements was to model the conical horn antenna used for measurements. Figure A.16 depicts the typical, datasheet gain of the transmit and receive conical horns. Typical E-plane HPBW is 11 degrees, and H-plane HPBW is 13 degrees. The simulated conical horn gain is depicted in Figure A.17 and Figure A.18. Simulated E-plane HPBW is 10 degrees, and H-plane HPBW is 12 degrees. The peak gain in simulations is 24 dBi while the

datasheet typical gain is 23 dBi. Overall the simulated antenna pattern is quite similar to the conical horn antenna that was used for test.

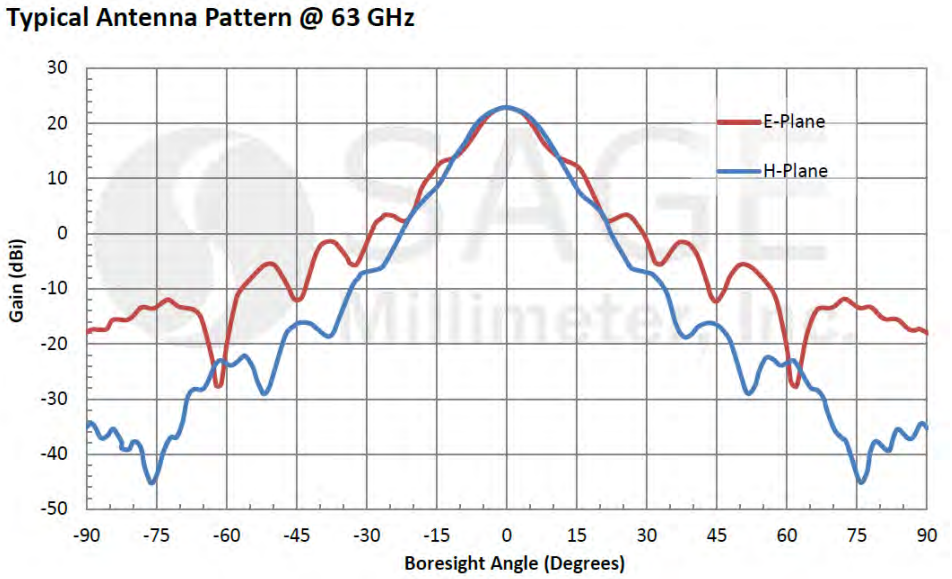

Figure A.16: Transmit and receive conical horn Sage SAC-2309-15-S2 antenna typical gain in the E and H planes.

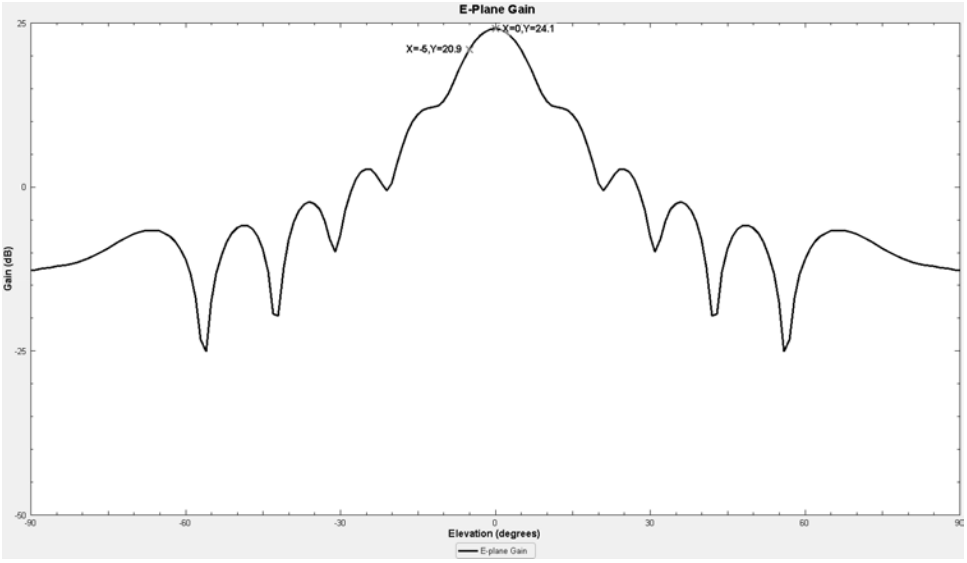

Figure A.17: Simulated conical horn E-plane gain.

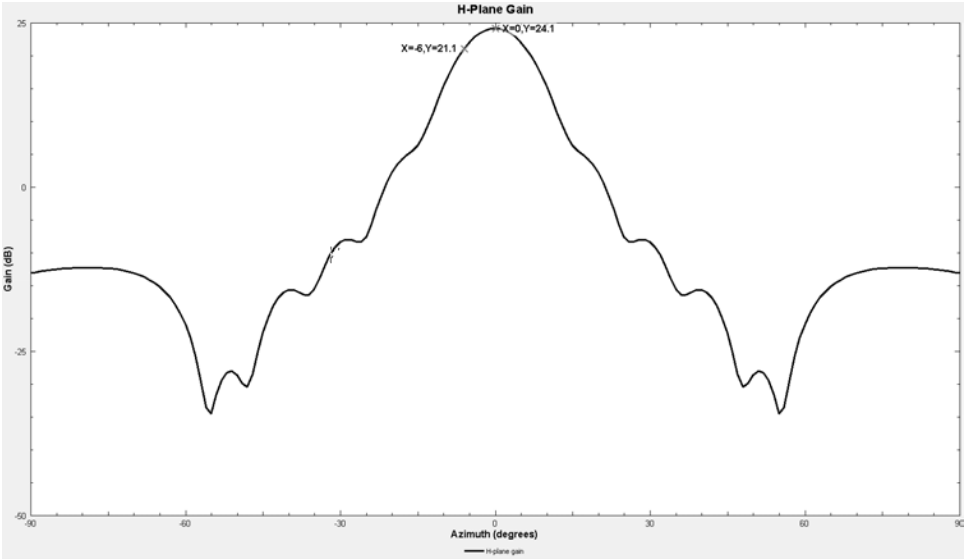

Figure A.18: Simulated conical horn H-Plane gain.

Next simulations were performed with a Boeing 777-200 aircraft model and conical horn. Figure A.19 depicts a top view of the simulation model. The transmit antenna inside the aircraft was rotated in 30 degree increments to replicate what was done on-aircraft measurements in Marana, AZ.

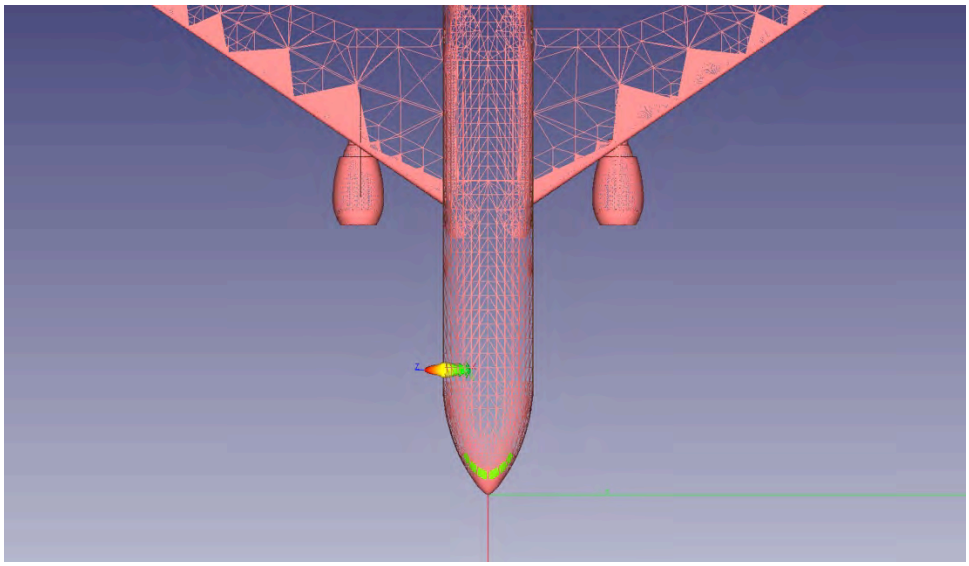

Figure A.19: Top view of simulation model.
The transmit antenna is placed in approximately the same location as measured data; i.e. in the aisle near seat 12J.

Finally the difference in simulated gain at all azimuth offsets relative to simulated through the window gain was calculated. See Table A.2, “Simulated avg. delta” column. The overall average error between measured and simulated values is 2.7 dB. Further, the simulated average difference between gain through the window and any other steering angle is 40.6 dB. Measurement results yielded an overall average of 40.5 dB, indicating that the simulated results provide an excellent overall indication of effective aircraft attenuation.

Table A.2: Average difference between measured receive power at a transmit azimuth angle of 0 degrees (aligned with receive antenna boresight) and simulated average difference over a sweep of transmit azimuth angles.

TX Azimuth (deg)	Measured avg delta (dB)	Simulated avg delta (dB)	Difference (dB)
30	24.5	30.6	6.1
60	39	39.9	0.9
90	40.5	35.1	-5.4
120	41.6	48.2	6.6
150	44.4	42.4	-2
180	30	22.8	-7.2
210	38.9	46.4	7.5
240	44.6	46.1	1.5
270	40.5	34.5	-6
300	41	38.5	-2.5
330	28.9	30.6	1.7

In sum, the simulation results are close to measurement results. This indicates that ray tracing tools may be used for prediction of fair field gain and effective aircraft attenuation.

A.5 Simulation Results for Aircraft

This section provides simulated far field gain and associated analyses for various use cases and antenna types.

A.5.1 Access Point Use Case

WiGig access points will typically be placed above ceiling panels towards the crown of an aircraft. Though the EESS Interference Assessment section assumes 30 access points and 6 channels, this section assumes a total of 16 access points and 4 channels. The exact number of access point and channels will vary by application. The numbers assumed here are for illustrative purposes and are sufficient for assessing sensitivity to WiGig device placement. Figure A.20 depicts an example set of access point locations and their respective channel numbers.

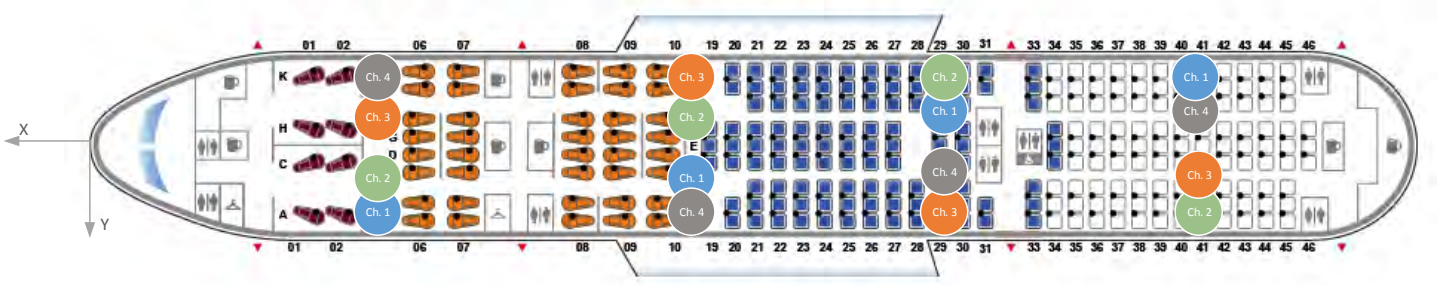

Figure A.20: Approximate access point locations.
Channel assignments run along a diagonal to provide some co-channel interference mitigation.

The physical access point locations used in simulation models are provided in Table A.3.

Table A.3: WiGig channel 1 access point physical locations relative to the nose of the aircraft.

Access Point Position Number	X (m)	Y (m)	Z (m)
1	-12	1.75	2.6
2	-22	1	2.6
3	-32	-1	2.6
4	-42	-1.75	2.6

A.5.2 Circular Symmetric 30 degree HPBW Antenna

A circular symmetric, 30 degree HPBW antenna is used for simulations in this section. Assuming an access point that is mounted above the cabin ceiling panels, the WiGig access point will be required to cover a half sphere or 2π steradians. Given the 30 degree HPBW, a total of 37 steering angles are required to efficiently cover the half sphere. Simulations provide the far field gain over 4π steradians for each of the 37 steering angles. The far field gain includes aircraft scattering and absorption due to a Perfect Electrical Conductor (PEC) backed complex dielectric aircraft skin material assignment. A histogram and empirical cumulative distribution of the simulated far field gain is then generated for each steering angle. In addition, a histogram and empirical cumulative distribution over all steering angles is provided for each access point position. The results are provided in the sections that follow. For reference, note that the peak gain of the 30 degree HPBW antenna is 16.2 dBi.

A.5.3 Access Point Position 1

Figure A.21 depicts a sample simulation model including the antenna pattern and steering angle for an access point in position 1. The histograms and empirical cumulative distributions that follow are based on far field gain observations over 4π steradians. Far field observations are taken in 1 degree increments in both the azimuth and elevation. The histograms and empirical cumulative distribution functions provided in the figures below utilize a 1 dB bin size.

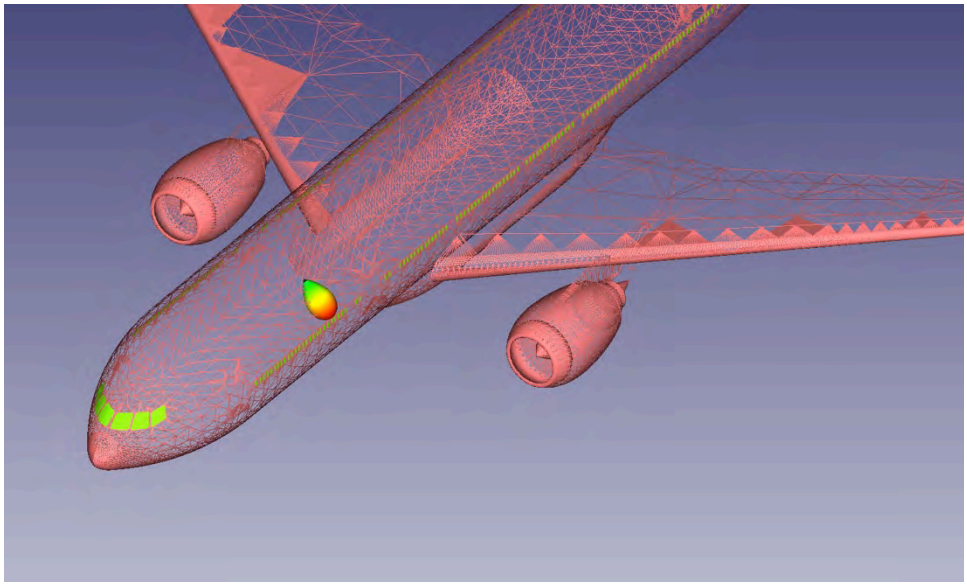

Figure A.21: Depiction of antenna in 777-200 model.
Antenna is in access point position 1 and pointed towards the windows. This steering angle represents 1 of 37 equally-probable steering angles.

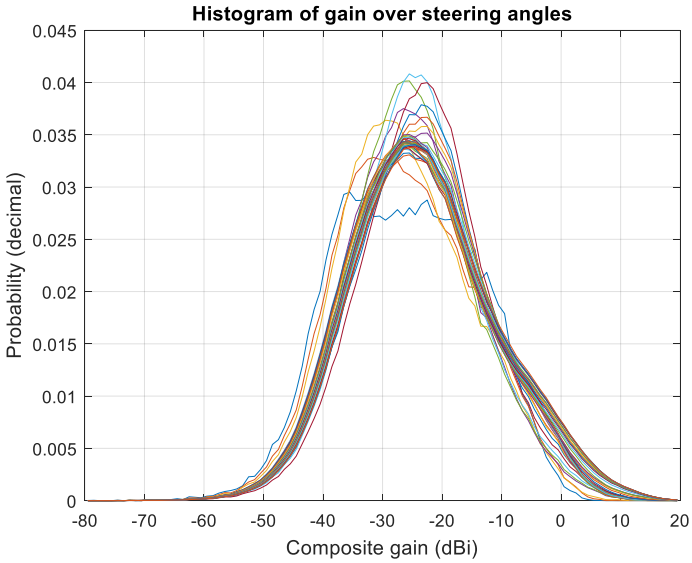

Figure A.22: Histograms of gain for each of the 37 available steering angles at Access Point Position 1.

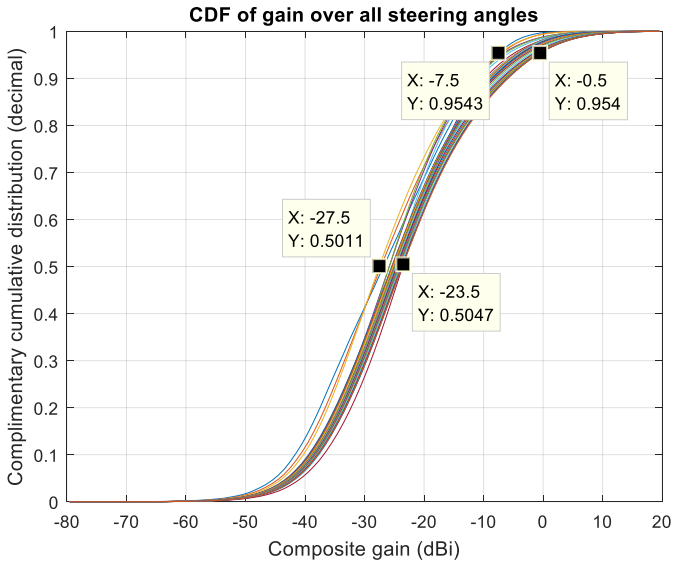

Figure A.23: Empirical cumulative distribution of gain for each of the 37 available steering angles at Access Point Position 1.

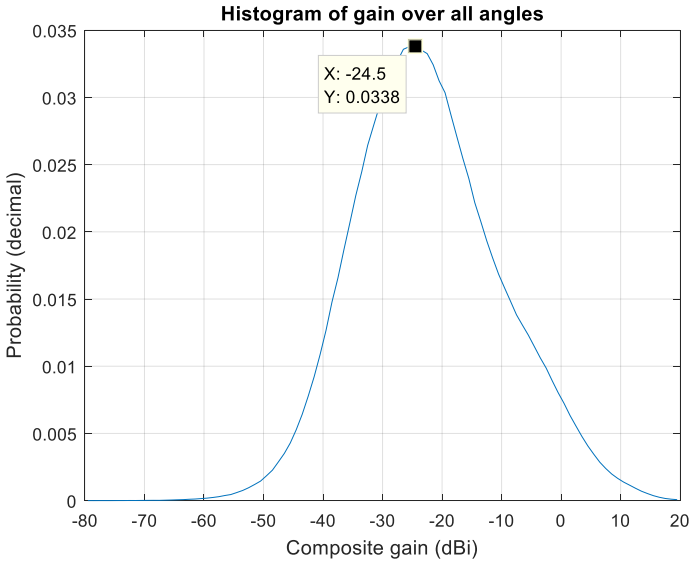

Figure A.24: Histogram of gain over all 37 available steering angles at Access Point Position 1.

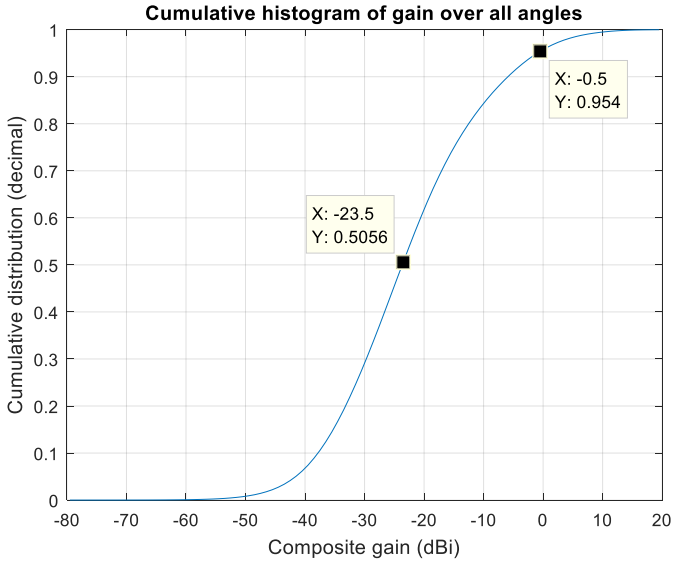

Figure A.25: Empirical cumulative distribution of gain for all 37 available steering angles at Access Point Position 1.

A.5.4 Access Point Position 2

Simulation results for access point Position 2 are provided below. The histograms and empirical cumulative distributions follow the same concepts as access point Position 1.

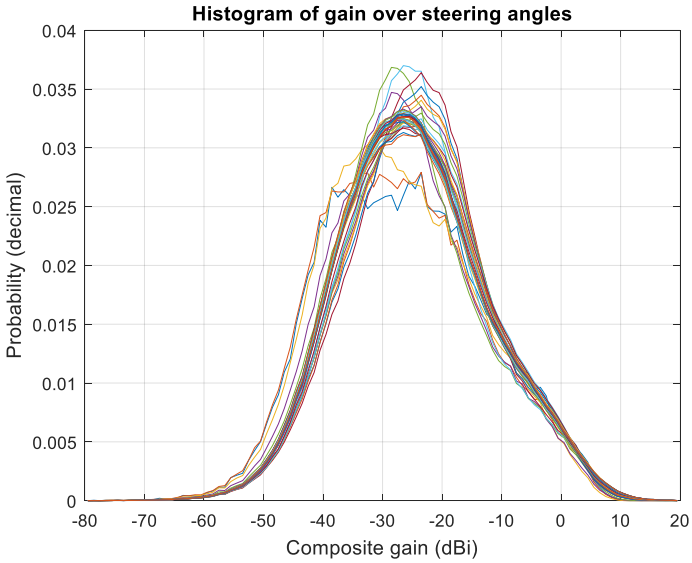

Figure A.26: Histograms of gain for each of the 37 available steering angles at Access Point Position 2.

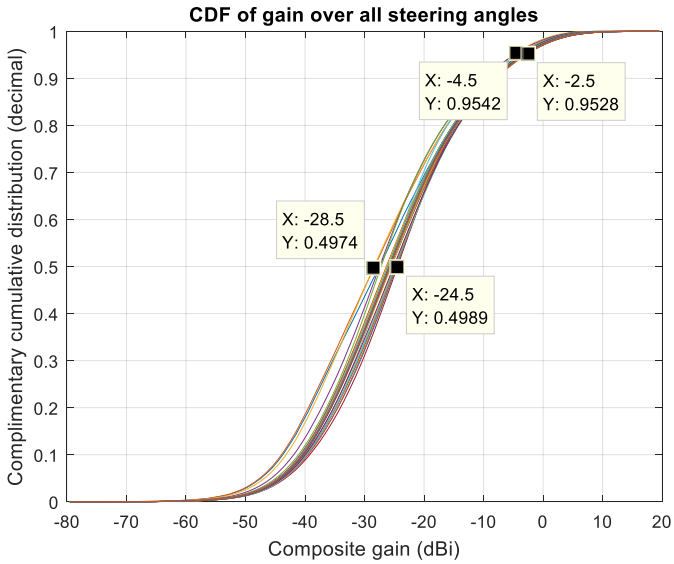

Figure A.27: Empirical cumulative distribution of gain for each of the 37 available steering angles at Access Point Position 2.

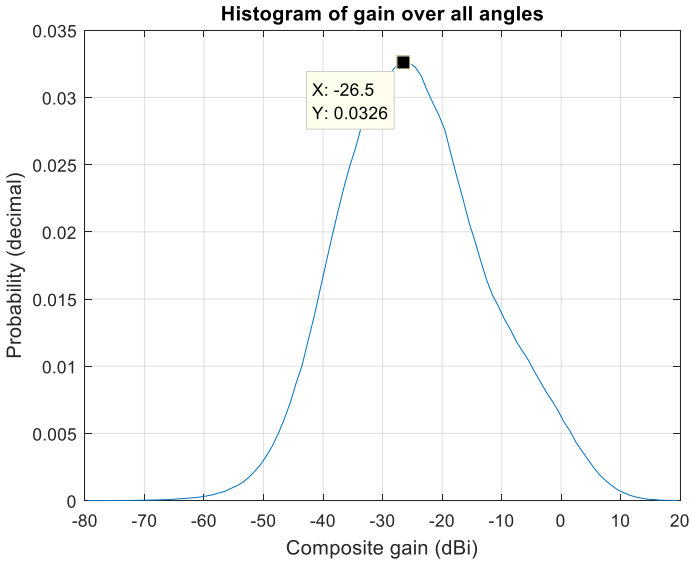

Figure A.28: Histogram of gain over all 37 available steering angles at Access Point Position 2.

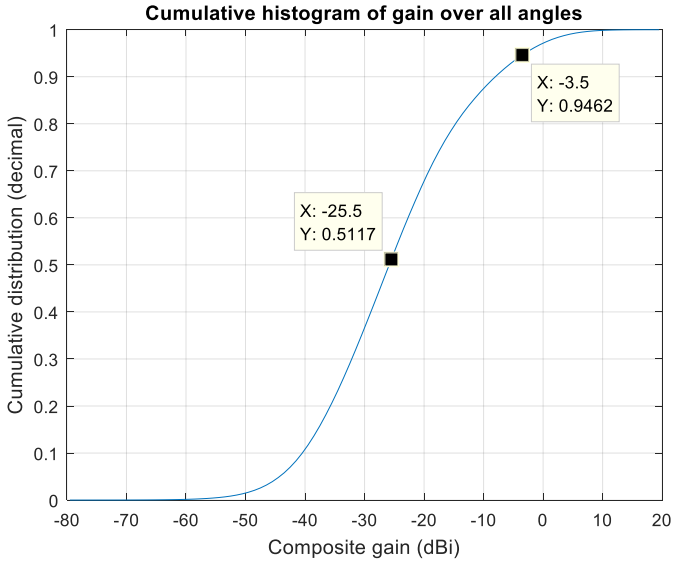

Figure A.29: Empirical cumulative distribution of gain for all 37 available steering angles at Access Point Position 2.

A.5.5 Access Point Position 3

Simulation results for access point position 3 are provided below. The histograms and empirical cumulative distributions follow the same concepts as access point position 1.

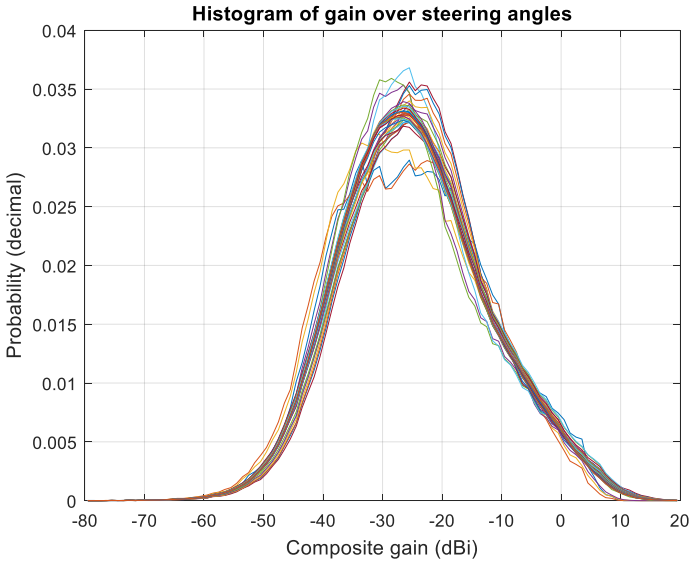

Figure A.30: Histograms of gain for each of the 37 available steering angles at Access Point Position 3.

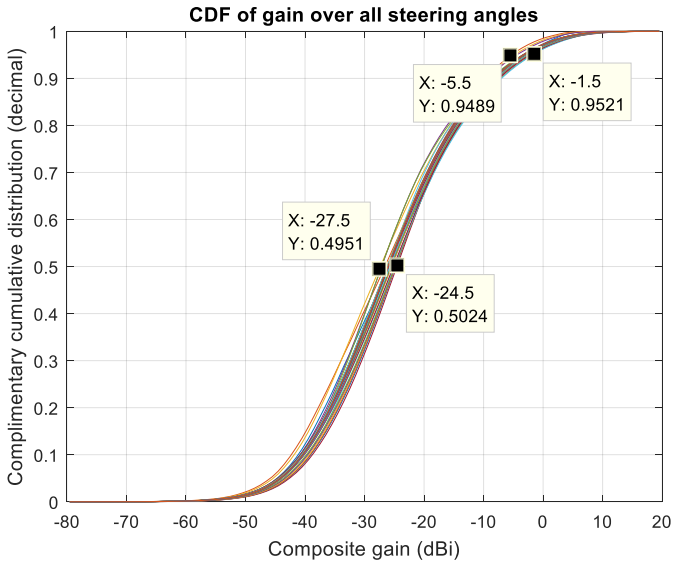

Figure A.31: Empirical cumulative distribution of gain for each of the 37 available steering angles at Access Point Position 3.

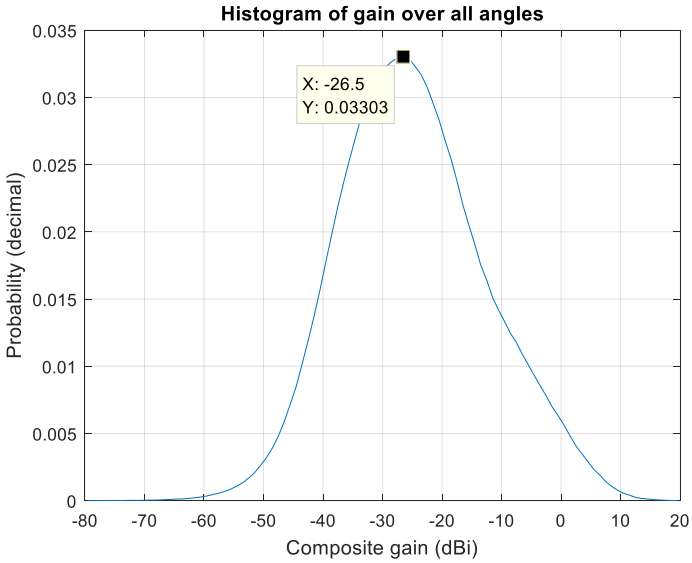

Figure A.32: Histogram of gain over all 37 available steering angles at Access Point Position 3.

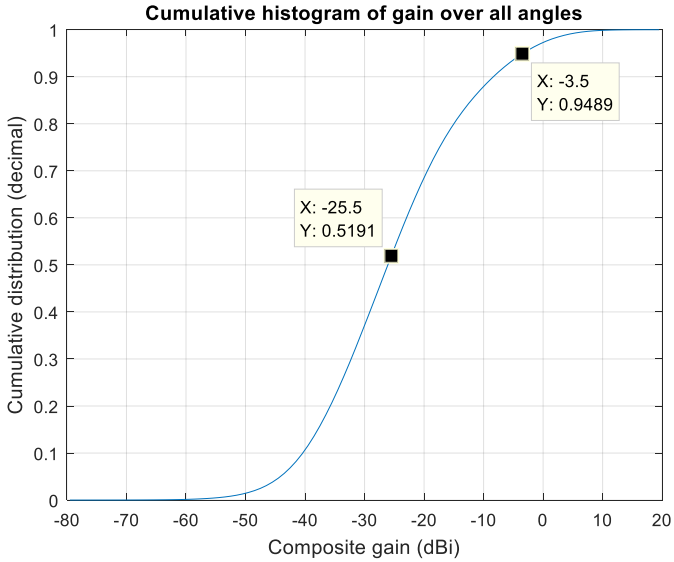

Figure A.33: Empirical cumulative distribution of gain for all 37 available steering angles at Access Point Position 3.

A.5.6 Access Point Position 4

Simulation results for Access Point Position 4 are provided below. The histograms and empirical cumulative distributions follow the same concepts as Access Point Position 1.

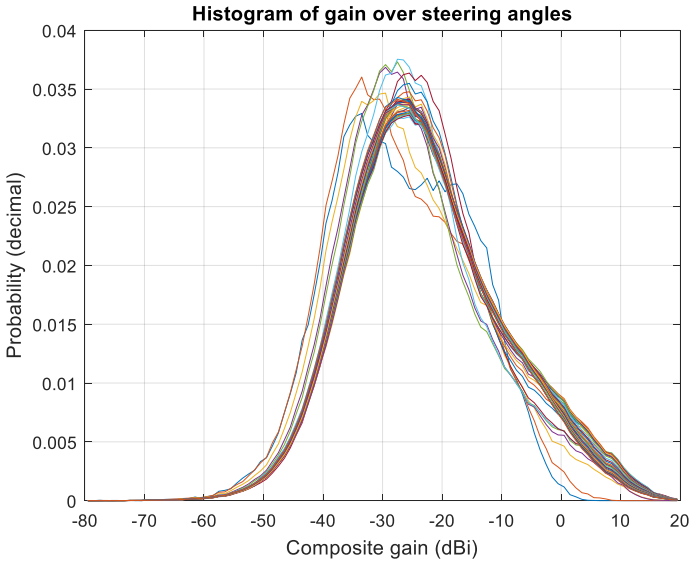

Figure A.34: Histograms of gain for each of the 37 available steering angles at Access Point Position 4.

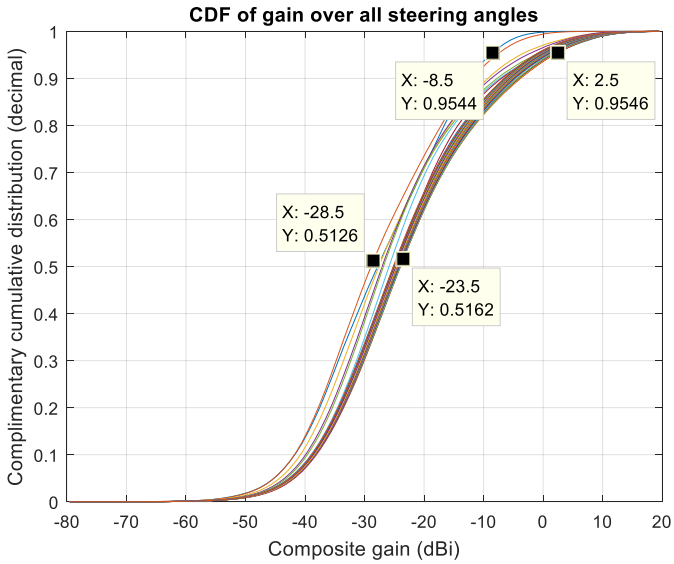

Figure A.35: Empirical cumulative distribution of gain for each of the 37 available steering angles at Access Point Position 4.

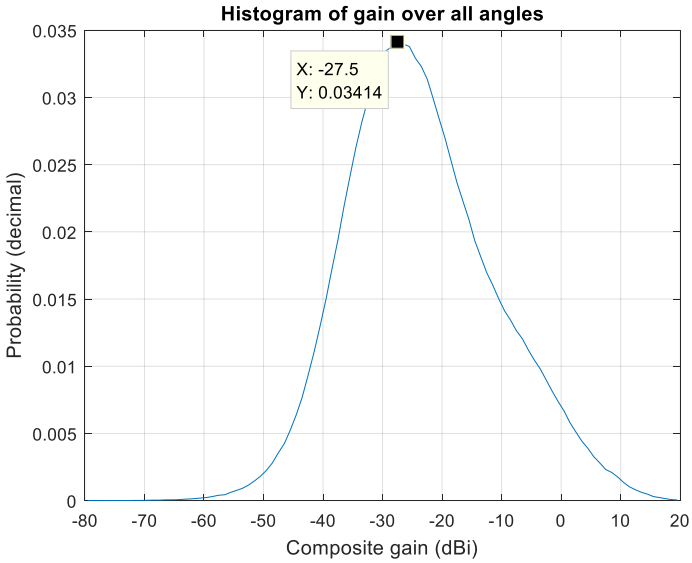

Figure A.36: Histogram of gain over all 37 available steering angles at Access Point Position 4.

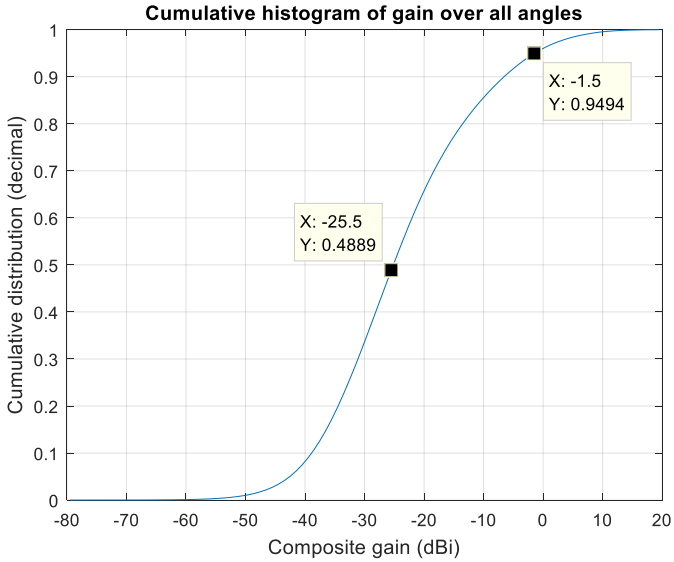

Figure A.37: Empirical cumulative distribution of gain for all 37 available steering angles at Access Point Position 4.

A.5.7 Summary of Circular Symmetric 30 degree HPBW Access Point Simulations

The empirical cumulative distributions provided above are summarized in Table A.4. The high and low values are taken from the empirical cumulative distributions of gain for each of the 37 steering angles. Please see Figure A.35 as an example. The overall values are taken from the empirical cumulative distribution over all 37 steering angles. Please see Figure A.37 as an example.

Table A.4: Summary of gain based on empirical cumulative distribution for each access point location.

Position	50 % Low	50 % High	95 % Low	95 % High	Overall 50 %	Overall 95 %
1	-27.5	-23.5	-7.5	-0.5	-23.5	-0.5
2	-28.5	-24.5	-4.5	-2.5	-25.5	-3.5
3	-27.5	-24.5	-5.5	-1.5	-25.5	-3.5
4	-28.5	-23.5	-8.5	2.5	-25.5	-1.5

Effective aircraft attenuation is defined as the difference between the free space peak antenna gain of 16.2 dBi and the simulated fair field gain summarized in Table A.4. Table A.5 provides a summary of the derived effective aircraft attenuation.

Table A.5: Effective attenuation based on empirical cumulative distributions of gain summarized in Table A.4.

Position	50 % Low	50 % High	95 % Low	95 % High	Overall 50 %	Overall 95 %
1	43.7	39.7	23.7	16.7	39.7	16.7
2	44.7	40.7	20.7	18.7	41.7	19.7
3	43.7	40.7	21.7	17.7	41.7	19.7
4	44.7	39.7	24.7	18.7	41.7	17.7

Observations and conclusions based on summary data in Table A.4 and Table A.5:

- The spread in effective attenuation for individual steering angles at 50 % probability ranges between 3 and 4 dB.
- The spread in effective attenuation at 95 % probability ranges between 2 and 7 dB.
- The spread at 95 % probability vs. 50 % probability is higher, though only by 3 dB.
- The spread at 50 % and 95 % probabilities is relatively small, indicating that steering angle has a rather small impact on the far field gain and ultimately the radiation from the aircraft.
- When considering all steering angles, there is approximately 2 to 3 dB difference between access point positions. This indicates that the effective attenuation or gain statistics are fairly insensitive to access point position.
- The overall average effective attenuation ranges from 39.7 to 41.7 dB. Aircraft fuselage attenuation measurements from Annex F: Aircraft Fuselage Attenuation Testing and copied in Figure A.38 indicate an effective attenuation of roughly 40 to 45 dB. Simulations are very consistent with the attenuation measurements in Annex E.

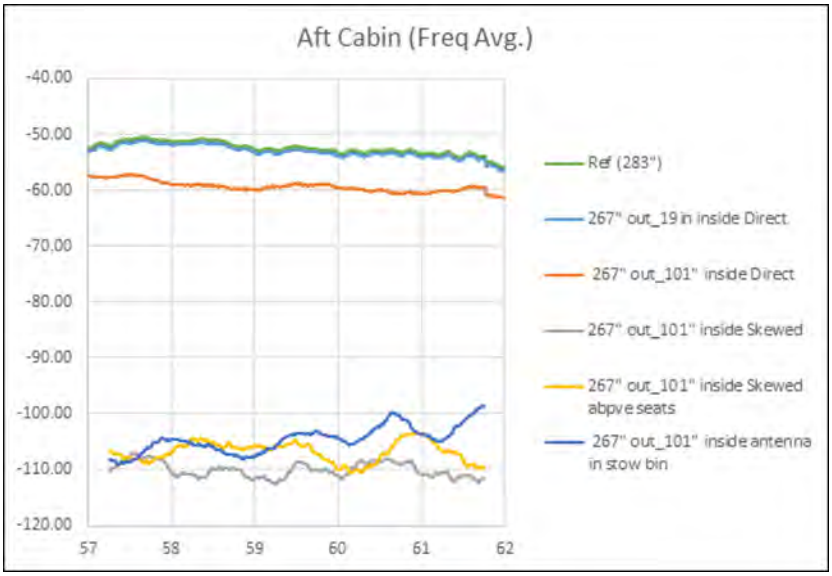

Figure A.38: Measurement data on 777-200 copied from Annex E: Aircraft Fuselage Attenuation Testing.

A.5.8 Fan Beam Antenna

Commercially available WiGig antenna implementations for mobile (nomadic) applications often utilize a non-square array of patch antenna elements. This results in a fan beam antenna pattern. A common array size is 2 x 8 which results in a 57 x 14 degree HPBW. The simulations that follow assume a 57 x 14 degree HPBW antenna in Access Point Position 1. The peak gain of the 57 x 14 degree antenna is 16.5 dBi. Given the simulation results for a 30 degree circular symmetric antenna in section A.5.2, simulating Access Point Positions 2 through 4 is unnecessary since the overall far field gain and effective aircraft attenuation are relatively insensitive to access point location.

A.5.9 Fan Beam Antenna in Access Point Position 1

The fan beam antenna steering angles are based on complete coverage of a half-sphere or 2π steradians. Histograms and empirical cumulative distributions are provided below based on far field gain observations over 4π steradians. Far field observations are taken in 1 degree increments in both the azimuth and elevation. The histograms and empirical cumulative distributions provided in the figures below utilize a 1 dB bin size.

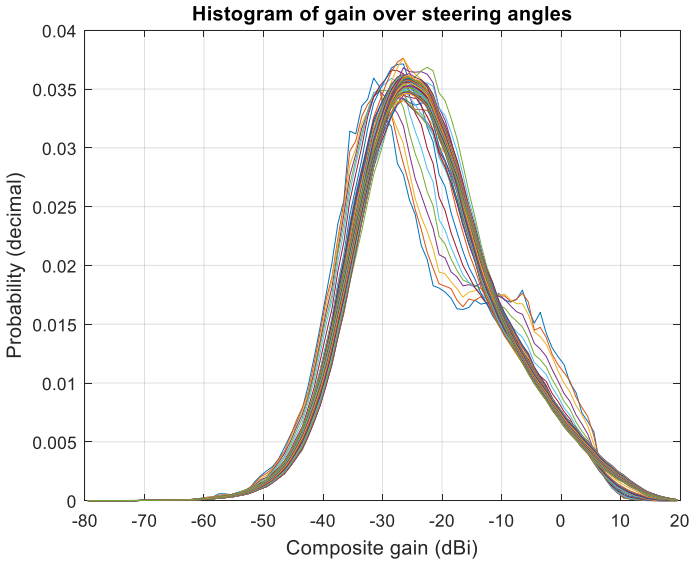

Figure A.39: Histograms of gain for each of the fan beam steering angles at Access Point Position 1.

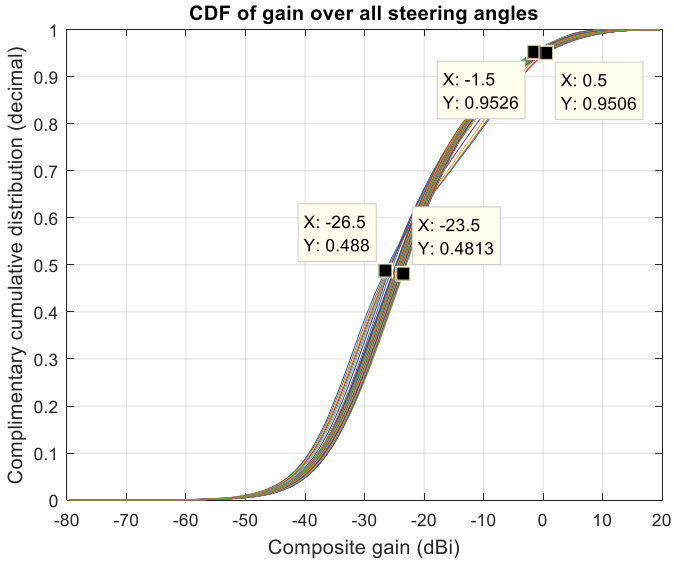

Figure A.40: Empirical cumulative distribution of gain for each of the fan beam steering angles at Access Point Position 1.

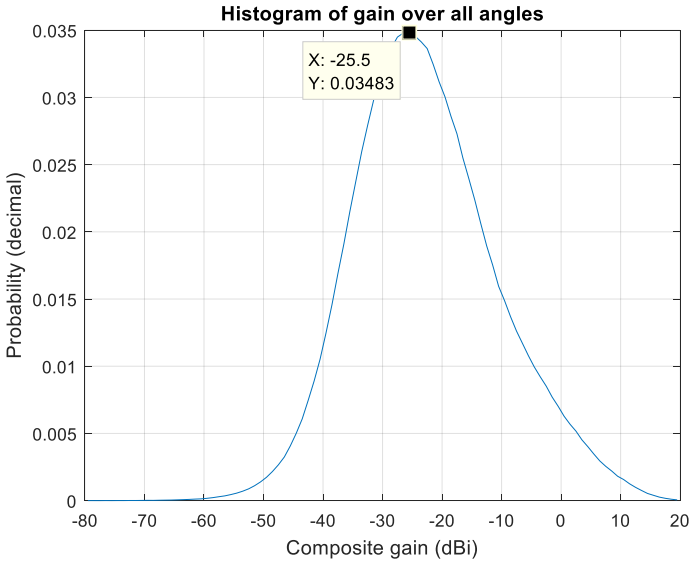

Figure A.41: Histogram of gain over all fan beam steering angles at Access Point Position 1.

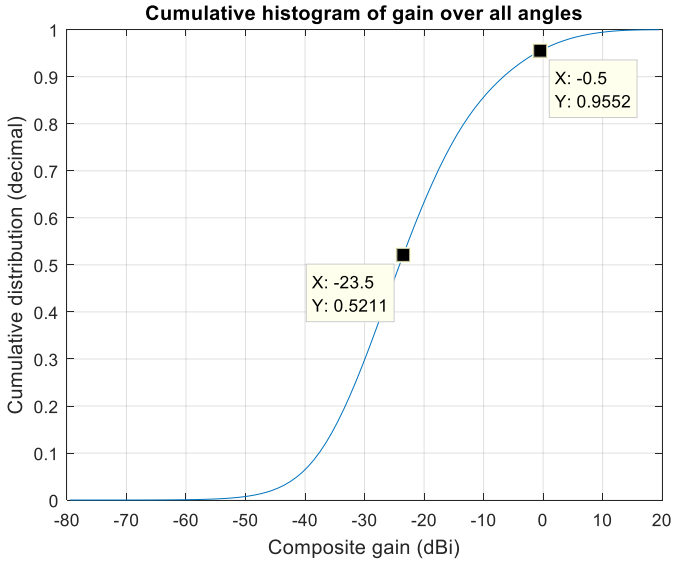

Figure A.42: Empirical cumulative distribution of gain over all fan beam steering angles at access point location 1.

A.5.10 Summary of Fan Beam Access Point Simulations

Table A.6 provides a summary of gain and effective aircraft attenuation based on empirical cumulative distributions for the fan beam and circular symmetric 30 degree HPBW antennas at Access Point Position 1. The results in Table A.6 lead to the following observations:

- The far field gain at 50 % cumulative probability for the fan beam antenna at access point position 1 is within 1 dB worst case of the 50 % cumulative probability of the circular symmetric antenna gain at Access Point Position 1.
- The far field gain at 95 % cumulative probability for the fan beam antenna at access point position 1 is within 6 dB worst case of the 95 % cumulative probability of the circular symmetric antenna gain at Access Point Position 1.

- The overall far field gain at 50 % cumulative probability for the fan beam antenna at access point position 1 is identical to the 50 % cumulative probability of the circular symmetric antenna gain at Access Point Position 1.
- The overall far field gain at 95 % cumulative probability for the fan beam antenna at access point position 1 is within 1 dB of the 95 % cumulative probability of the circular symmetric antenna gain at Access Point Position 1.
- The fan beam and circular symmetric antenna effective attenuation values at all but the 95 % high empirical cumulative probability are nearly identical.
- When comparing the fan beam and circular symmetric statistics, it becomes evident that the antenna pattern has negligible impact on the overall statistics. This is an important observation since it indicates that the variance in antenna array implementations has little impact on the overall radiation of the aircraft.
- Further comparison of simulation results with fuselage attenuation measurement results in Figure A.38 again shows excellent correlation. Note that Annex E utilized a pyramidal horn with a gain of approximately 24 dBi for measurements on the 777-200 aircraft in Marana, AZ.

Table A.6: Summary of gain and effective aircraft attenuation based on empirical cumulative distributions for a fan beam and circular symmetric 30 degree HPBW antennas in access point position 1.
Data for the circular symmetric 30 degree HPBW antenna is copied from Table A.4 and Table A.5 for reference.

	50 % Low	50 % High	95 % Low	95 % High	Overall 50 %	Overall 95 %
Fan beam gain	-26.5	-23.5	-1.5	0.5	-23.5	-0.5
Fan beam effective attenuation	43.2	40.2	18.2	16.2	40.2	17.2
Circular symmetric gain	-27.5	-23.5	-7.5	-0.5	-23.5	-0.5
Circular symmetric effective attenuation	43.7	39.7	23.7	16.7	39.7	16.7

A.5.11 PED Use Case

The access point use case has been the primary focus in this paper so far. The PED use case is expected to behave similarly to if not better than the access point use case. Given that section A.5.8 showed the antenna pattern has a minimal impact on radiation statistics, a circular symmetric 30 degree HPBW antenna was used for the PED use case for the sake of simplicity and improved simulation time. The PED was placed 12 m from the nose of the aircraft, 1.75 m away from the centerline of the aircraft towards the port side and approximately 1 m above the floor. The location of the PED is depicted in Figure A.43 and Figure A.44. Figure A.44 also provides a depiction of the antenna beam pointing out the port side window. PED orientation relative to an access point will be random therefore it is assumed that the PED will steer over 4π steradians.

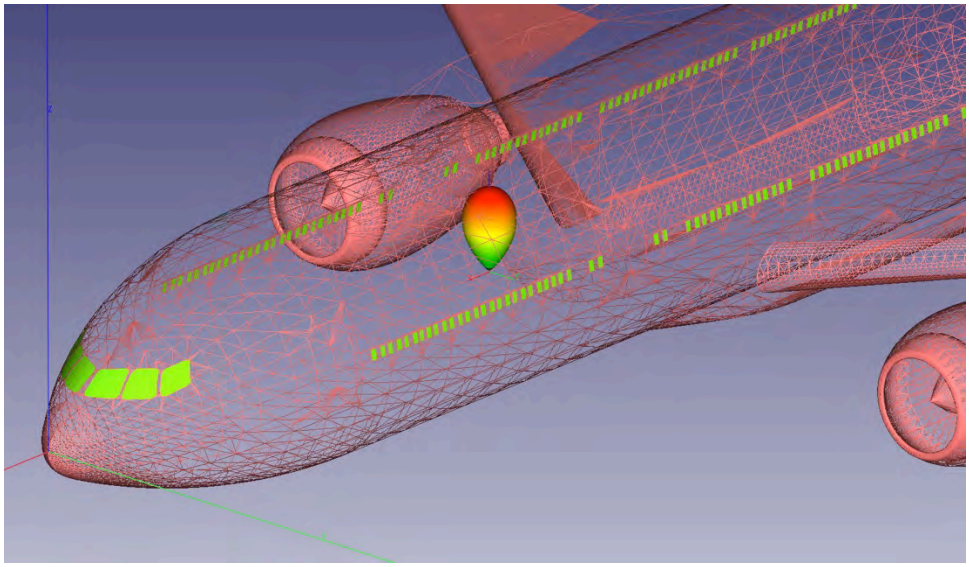

Figure A.43: Depiction of antenna in 777-200 model.
The antenna is in the PED position pointing towards the crown of the aircraft.

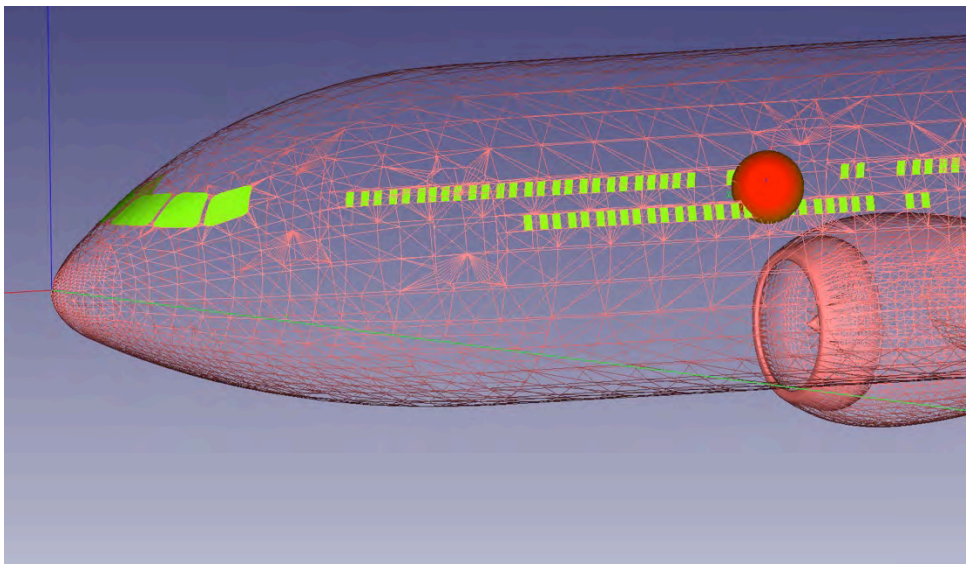

Figure A.44: An alternate depiction of the antenna in the 777-200 model.
The antenna is in the PED position pointing towards a port side window of the aircraft.

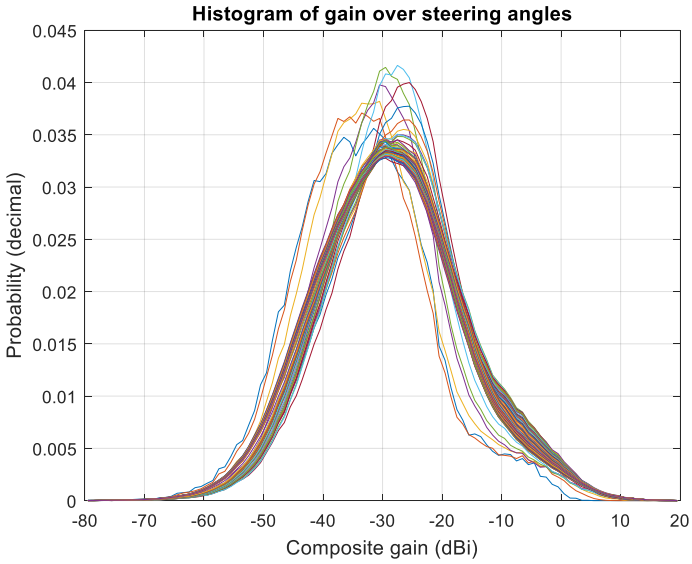

Figure A.45: Histograms of gain for each of the circular symmetric antenna steering angles at the PED position.

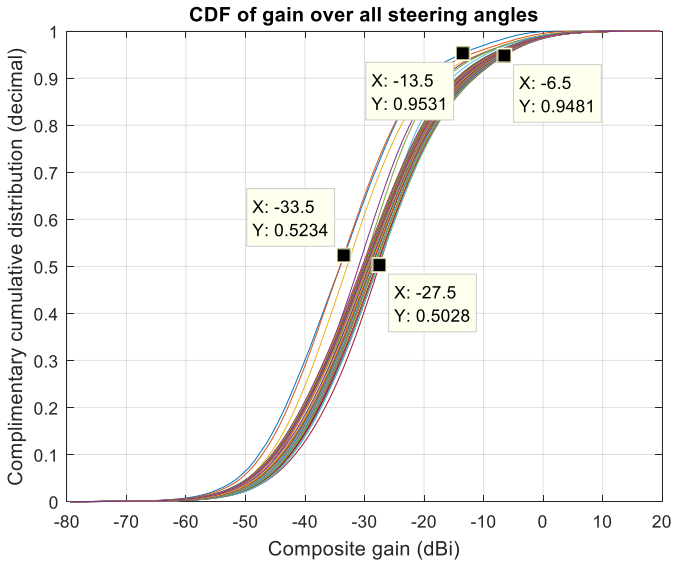

Figure A.46: Empirical cumulative distribution of gain for each of the circular symmetric steering angles at the PED position.

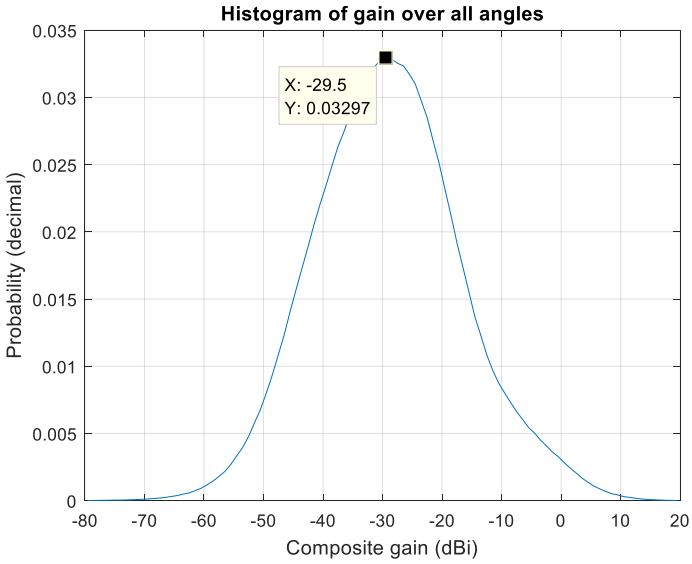

Figure A.47: Histogram of gain over all circular symmetric antenna steering angles at the PED position.

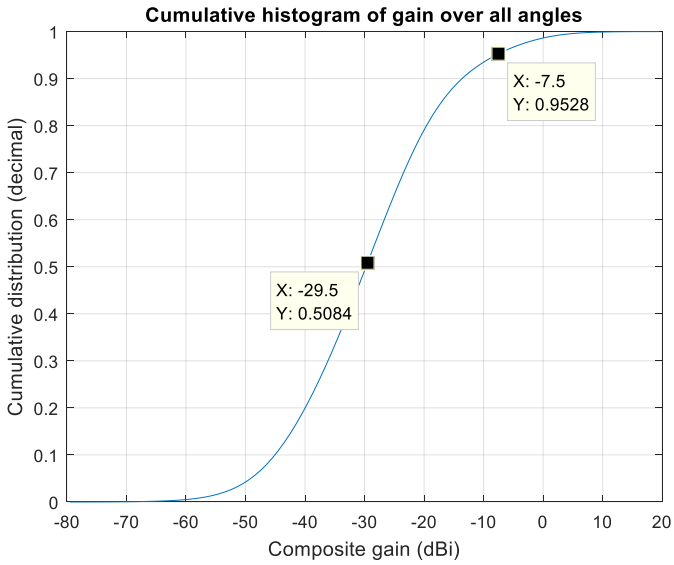

Figure A.48: Empirical cumulative distribution of gain over all circular symmetric antenna steering angles at the PED position.

A.5.12 Summary of PED Use Case Simulations

PED use case simulation results are summarized in Table A.7. The following observations and conclusions may be made:

- The PED use case yields lower gain and higher effective attenuation than the access point use case with circular symmetric 30 degree HPBW antenna. This is due to the reduced probability of the PED pointing towards a window when steering over 4π steradians towards the ceiling of the aircraft.
- It may be argued that simulations for the PED use case should have considered steering coverage over a full sphere rather than a half sphere. However, the PED use case is not expected to yield far field gain or effective aircraft attenuation that is worse than what was simulated for access point use cases. In general, the results for the access point use case will be used in the development of the emissions model provided in section A.6.

Table A.7: Summary of PED gain and effective attenuation statistics with comparison to access point 1 statistics.

Access point 1 data is copied from Table A.4 and Table A.5 for convenience.

	50 % Low	50 % High	95 % Low	95 % High	Overall 50 %	Overall 95 %
PED gain	-33.5	-27.5	-13.5	-6.5	-29.5	-7.5
PED effective attenuation	49.7	43.7	29.7	22.7	45.7	23.7
Access point position 1 gain	-27.5	-23.5	-7.5	-0.5	-23.5	-0.5
Access point position 1 effective attenuation	43.7	39.7	23.7	16.7	39.7	16.7

A.5.13 Summary and Comparison of Aircraft Simulation Results

Several sets of simulations were performed to determine the statistical nature of far field gain and effective aircraft attenuation. These simulations included access point and PED use cases. The access point use case simulations included multiple access point locations as well as two different antenna patterns. The PED use case included a single PED location and a circular symmetric 30 degree HPBW antenna steered over 4π steradians. The results are summarized in Table A.8. A key observation from Table A.7 is the consistency of the effective attenuation at 50% probability shown in the right-most column. It is clear that the average effective attenuation is on the order of 40 dB and is by and large independent of antenna location and antenna type. The PED position is the only scenario where the average effective attenuation is 45.7 dB rather than approximately 40 dB. This is likely due to the reduced numbed of steering angles over which an aircraft window is directly illuminated.

Table A.8: Summary of overall gain statistics for each of the simulation scenarios.

Scenario	Gain at 50 % probability	Gain at 95 % probability	Peak gain (dBi)	Avg. Effective attenuation (dB)
Access point position 1 with 30 deg HPBW circular symmetric antenna	-23.5	-0.5	16.2	39.7
Access point position 2 with 30 deg HPBW circular symmetric antenna	-25.5	-3.5	16.2	41.7
Access point position 3 with 30 deg HPBW circular symmetric antenna	-25.5	-3.5	16.2	41.7
Access point position 4 with 30 deg HPBW circular symmetric antenna	-25.5	-1.5	16.2	41.7
Access point position 1 with fan beam antenna	-23.5	-0.5	16.7	40.2
PED position with 30 deg HPBW circular symmetric antenna	-29.5	-7.5	16.2	45.7

A.6 Fit of Statistical Emission to a X^2 Probability Density Function

The simulation results presented in section A.5 may now be used as the basis for a general aircraft gain and ultimately an aircraft effective attenuation model. A X^2 distribution fits the simulations results with relatively low sum square error. This section provides details on the X^2 model derivation and definition.

A.6.1 Fit Results

The fit results for each of the use cases simulated in section A.5 are provided in the figures below, and a summary is provided in Table A.9. The fit is based on optimizing the shape factor A in the X^2 distribution function to minimize the sum square error between simulated and predicted probability densities.

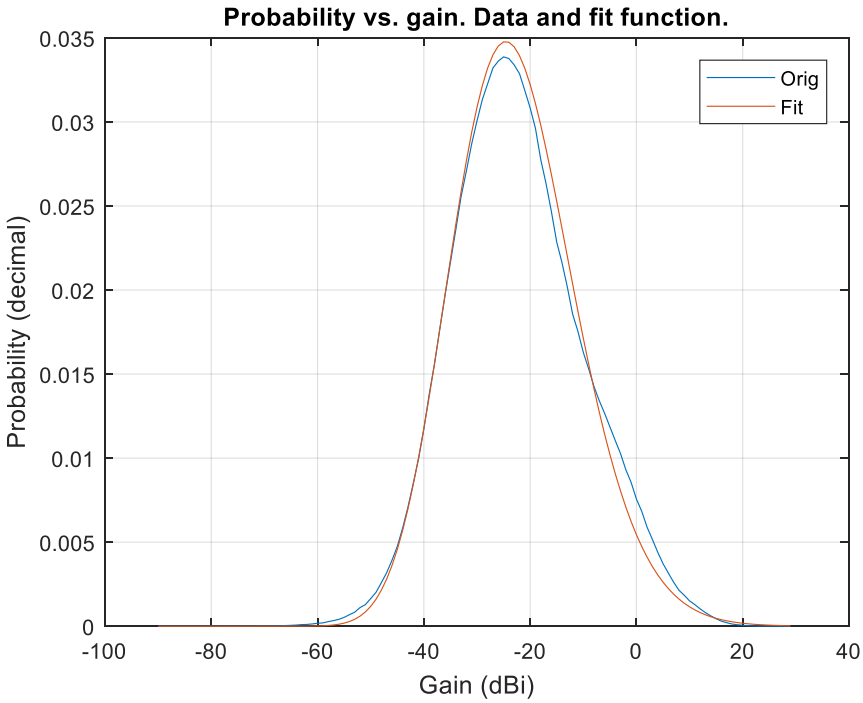

Figure A.49: Fit results from access point position 1.
The optimized value of A was 67.43 with a sum square error of 9.3E-5.

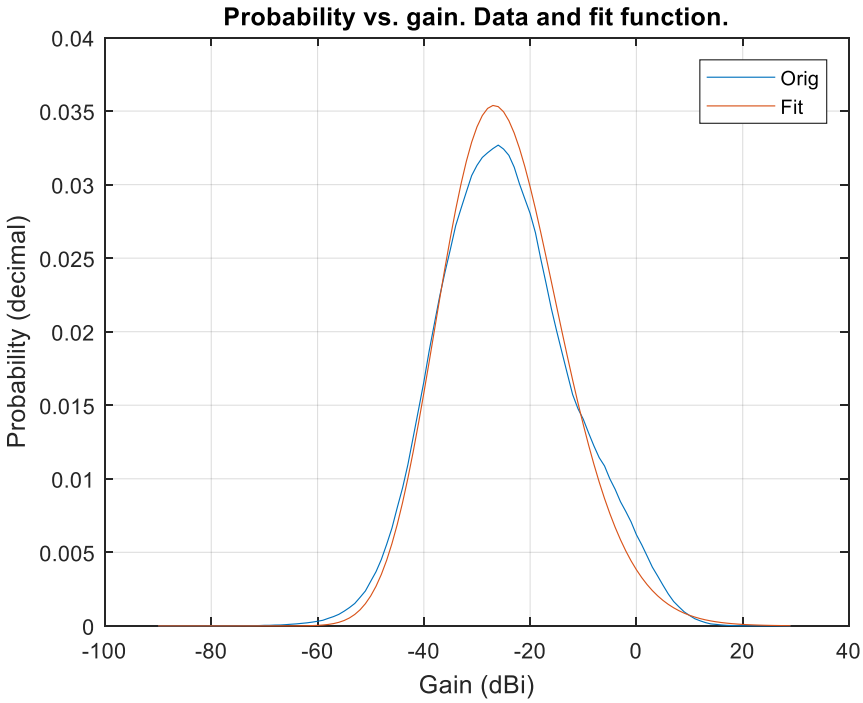

Figure A.50: Fit results from Access Point Position 2.
The optimized value of A was 65.21 with a sum square error of 1.8E-4.

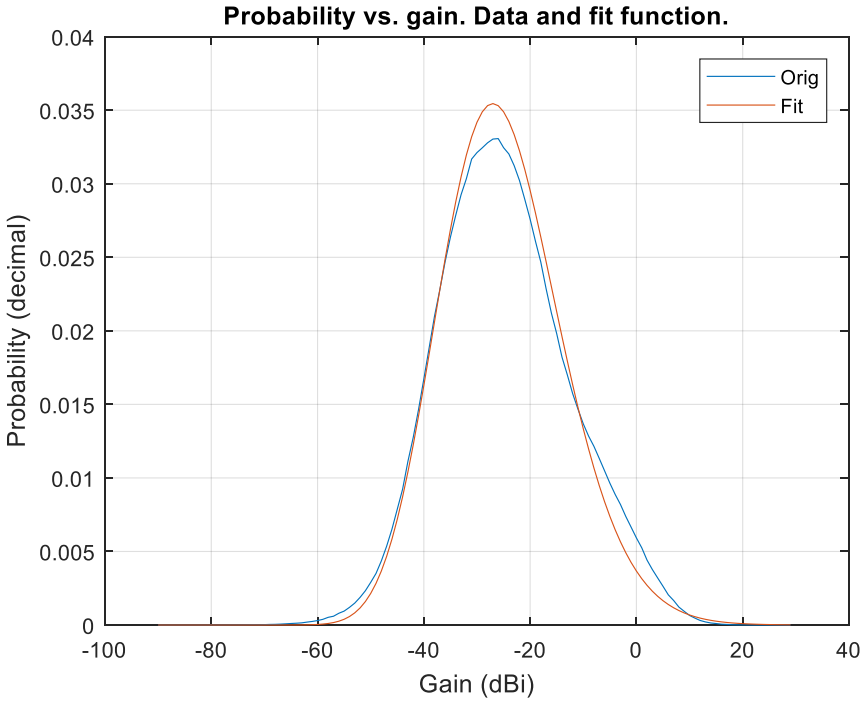

Figure A.51: Fit results from Access Point Position 3.
The optimized value of A was 64.98 with a sum square error of 1.5E-4.

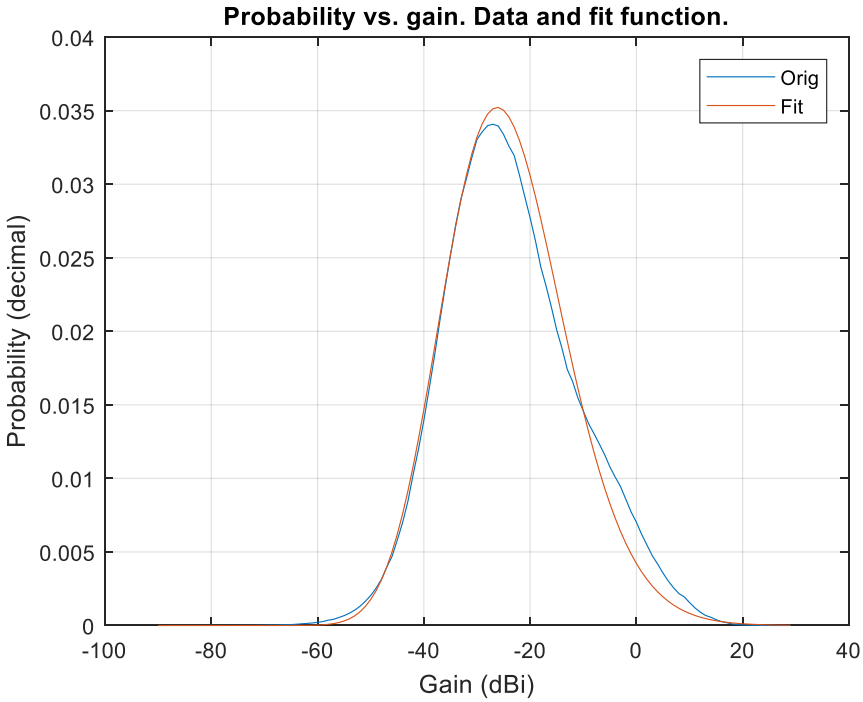

Figure A.52: Fit results from access point position 4.
The optimized value of A was 65.81 with a sum square error of 1.8E-4.

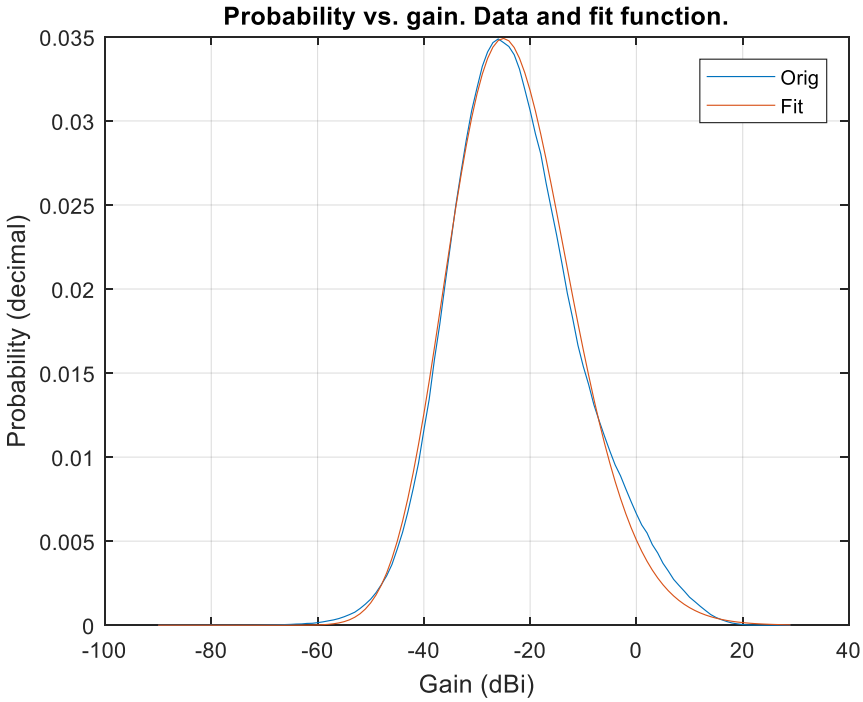

Figure A.53: Fit results for access point position 1 with fan beam antenna.
Optimized value of A was 66.96 with a sum square error of 5.7E-5.

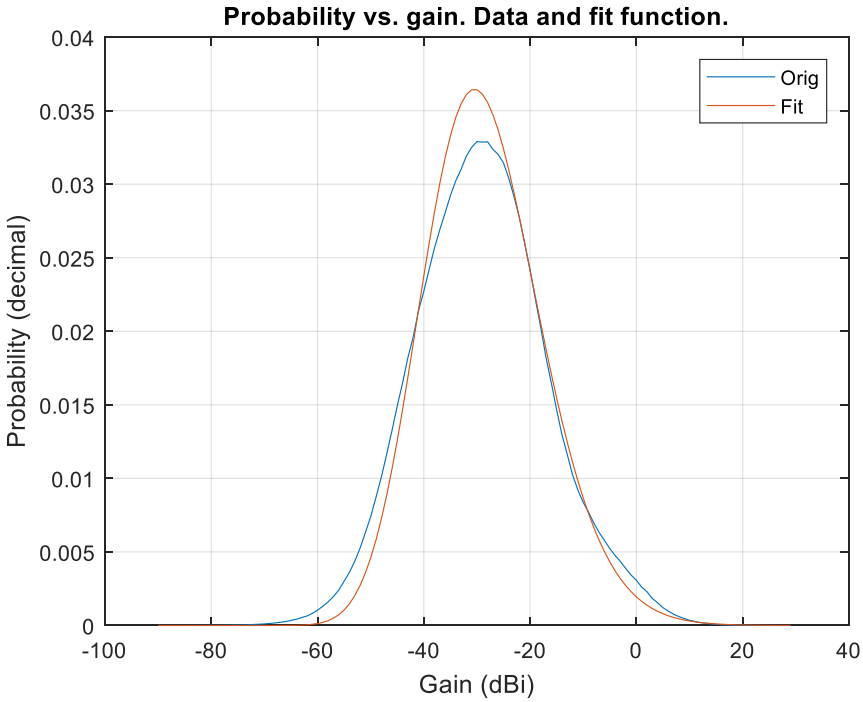

Figure A.54: Fit results for PED use case.
Optimized value of A was 60.61 with a sum square error of 2.6E-4.

Table A.9: Summary of fit values for variable A in X2 distribution.

Scenario	Value of A in X^2
Access point position 1 with 30 deg HPBW circular symmetric antenna	67.4
Access point position 2 with 30 deg HPBW circular symmetric antenna	65.2
Access point position 3 with 30 deg HPBW circular symmetric antenna	65
Access point position 4 with 30 deg HPBW circular symmetric antenna	65.8
Access point position 1 with fan beam antenna	67
PED position with 30 deg HPBW circular symmetric antenna	61.5

A.6.2 Gain and Effective Attenuation Statistical Model

The probability density function for gain is

$$P(gain, A) = \frac{(gain + 90)^{\frac{A}{2}-1}}{2^{A/2} \cdot \exp\left(\frac{gain + 90}{2}\right) \cdot \Gamma\left(\frac{A}{2}\right)}$$

where

- Gain in dB is the independent variable in the X^2 distribution and has a valid range of [-90, 30]. Note that a X^2 distribution requires the independent variable (gain in this case) to be greater than or equal to 0. Therefore the equation above includes a 90 dB offset, and hence the necessary valid range definition of [-90, 30].
- A is the shape factor. The shape factor A is 66 and is based on the average of fit values for A over all access point simulations. The PED use case is not used for determining the shape factor.
- Γ represents the gamma function.

In most cases it will be more convenient to use an effective aircraft attenuation rather than far field gain. Table A.8 above provides examples of this concept, where the average effective attenuation is the difference between the peak gain used in simulations and average gain over all steering and observation angles.

The probability density function for attenuation is:

$$P(atten, A) = \frac{(atten + offset)^{\frac{A}{2}-1}}{2^{A/2} \cdot exp\left(\frac{atten + offset}{2}\right) \cdot \Gamma\left(\frac{A}{2}\right)}$$

where

- $atten = gain - 16.5$,
- $offset = -\min(atten)$,
- Gain has the same definition as above and has a valid range of [-90, 30]. Attenuation ($atten$) then has a valid range of [-106.5, 13.5],
- A is the same as above.

Note that these equations result in a negative value for attenuation.

The probability density function for attenuation defined above is admittedly a bit cumbersome. A simpler and likely more practical method of determining attenuation is to utilize the “chi2rnd” function

in Matlab (or equivalent) to determine some random gain. Then the attenuation may be determined from the gain.

In the event an even simpler model is desired, then the average effective aircraft attenuation of approximately 40 dB may be used.

B: In-Aircraft Emissions Testing

Annex B provides an overview, analysis and summary of fuselage attenuation measurement data in the 57 to 62 GHz frequency range collected on a Boeing 777-200 aircraft. Measurements were performed the week of June 24th, 2017 in Marana, AZ.

The goal of on-aircraft measurements was to validate or provide guidance for ray tracing simulations. These ray tracing simulations are aimed at determining the power radiated from an aircraft with WiGig (802.11 ad) transmitters. The results of ray tracing simulations are then used as inputs to higher-level simulations and models with the aim of determining the impacts of inside aircraft cabin WiGig transmitters on incumbent services.

Note: This annex covers on-aircraft measurements only. Ray tracing correlation with measurement data is documented in Annex A: WiGig Aircraft Emissions Model.

B.1 Test Concept and Setup

This section provides the general test concept and details of the test setup. It is divided into the following topics:

- General test concept
- Transmitter setup and characterization
- Receiver setup and characterization

B.1.1 General Test Concept

Aircraft cabin measurements were aimed at validating or providing guidance for ray tracing simulations. One of the challenges in ray tracing simulations is determining cabin and fuselage material properties. Previous laboratory measurements show that window materials provide little to no transmission loss in the 60 GHz band. It was also known that 60 GHz transmissions inside an aircraft fuselage have the potential to excite a very large number of reverberant modes, and cabin interiors will dampen these reverberant modes to some extent. What is unknown however is the amount of dampening that will occur due to objects inside the cabin. Therefore, the general test concept was to place a transmitter inside the aircraft and a receiver outside the aircraft. The transmitter inside the aircraft was rotated clockwise in 30 degree increments in an effort to excite both direct as well as indirect transmit-receive coupling. This concept is depicted in Figure B.1. Measurements were taken over a frequency range of 57 to 62 GHz with a 10 MHz step size in order to attain statistical significance. It was expected that the average difference between direct (through window) and indirect transmit-receive coupling would be used to determine ray tracing material properties.

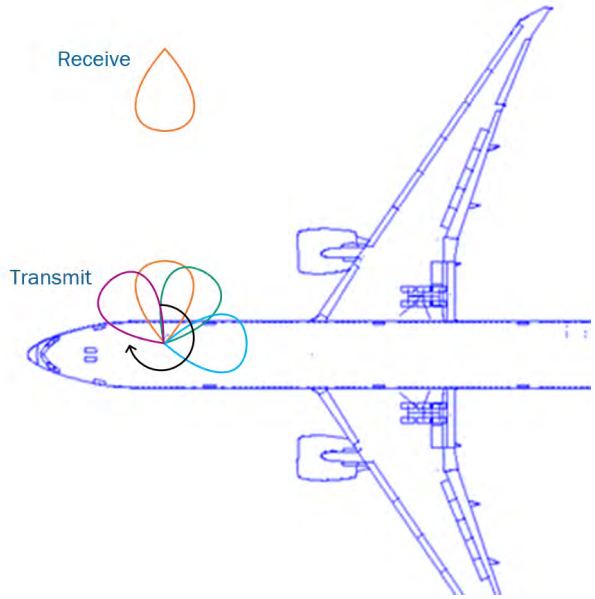

Figure B.1: General test concept.

B.1.2 Transmitter Test Setup

Figure B.2 provides a block diagram of the transmitter test setup, and Table B.1 provides the major transmitter test equipment used in testing.

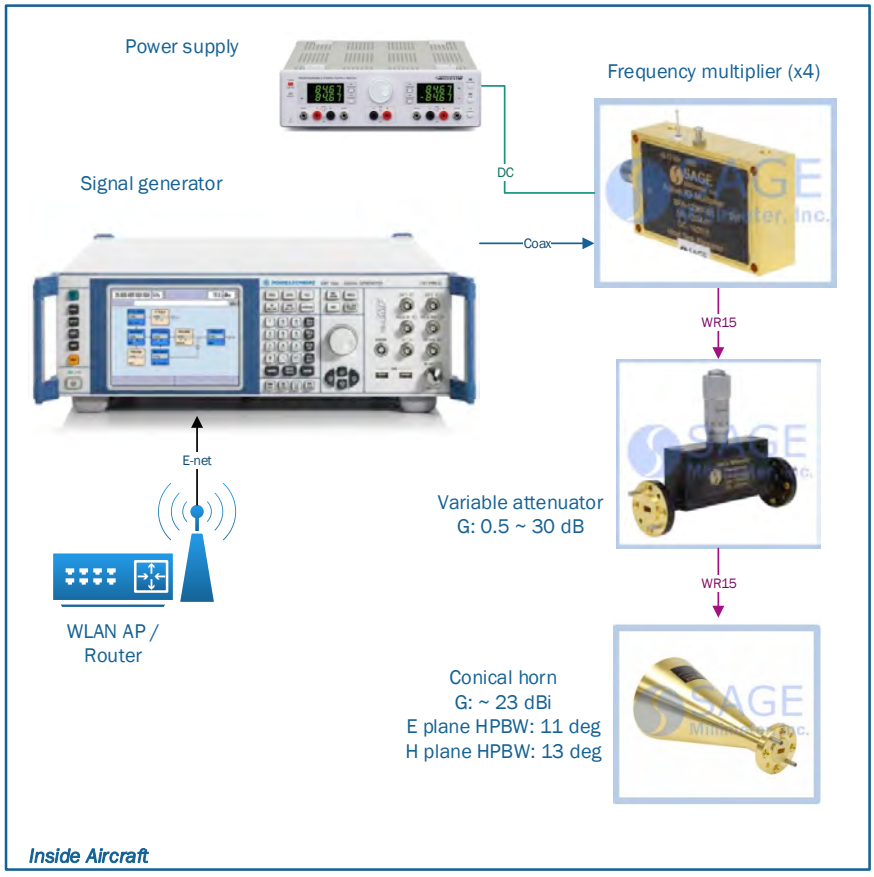

Figure B.2: Transmitter block diagram.

Table B.1: Major items in transmitter test setup.
Minor items such as RF cables, tripods or other mounting hardware are omitted from the table.

Component	Manufacturer	Model
Signal generator	Rohde & Schwarz	SMF100A-22
Frequency multiplier (x4)	Sage Millimeter	SFA-154KF-S1
Variable attenuator	Sage Millimeter	STA-30-15-M2
Conical horn	Sage Millimeter	SAC-2309-15-S2

B.1.3 Transmitter Characterization

Figure B.3 provides measured power as a function of frequency and variable attenuator Vernier setting. The reference plane for conducted power measurements was at the output of the variable attenuator. A Sage Millimeter SWC-151F-E1 WR-15 to 1 mm coaxial adapter was used between the output of the variable attenuator and a Rohde & Schwarz NRP-Z110 thermal power sensor. Given a conical horn gain of approximately 23 dBi and a temporary FCC license to transmit at 30 dBm EIRP maximum, the variable attenuator Vernier was set to 0.6 to yield approximately 5 dBm conducted power for on-aircraft tests.

Note: The transmit antenna used for testing was not calibrated, and the exact antenna gain and pattern are unknown. This is generally not an issue since conclusions will be driven based on relative rather than absolute measurements.

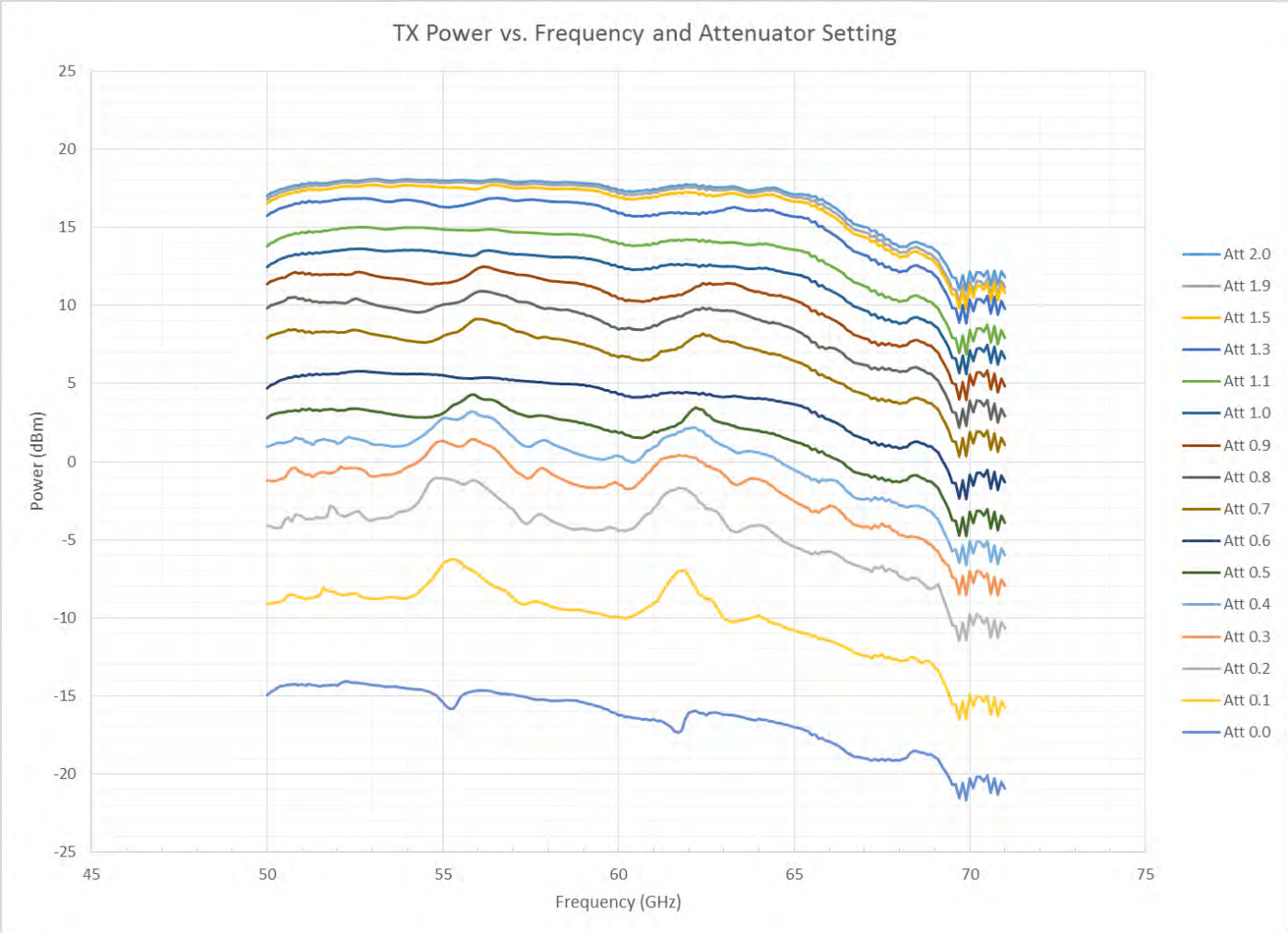

Figure B.3: Conducted transmit power at the output of the variable attenuator.
Transmit power is plotted vs. frequency and variable attenuator Vernier setting.

B.1.4 Receive Test Setup

Figure B.4 provides a block diagram of the receive test setup. Table B.2 provides the major test equipment used in the receive test setup.

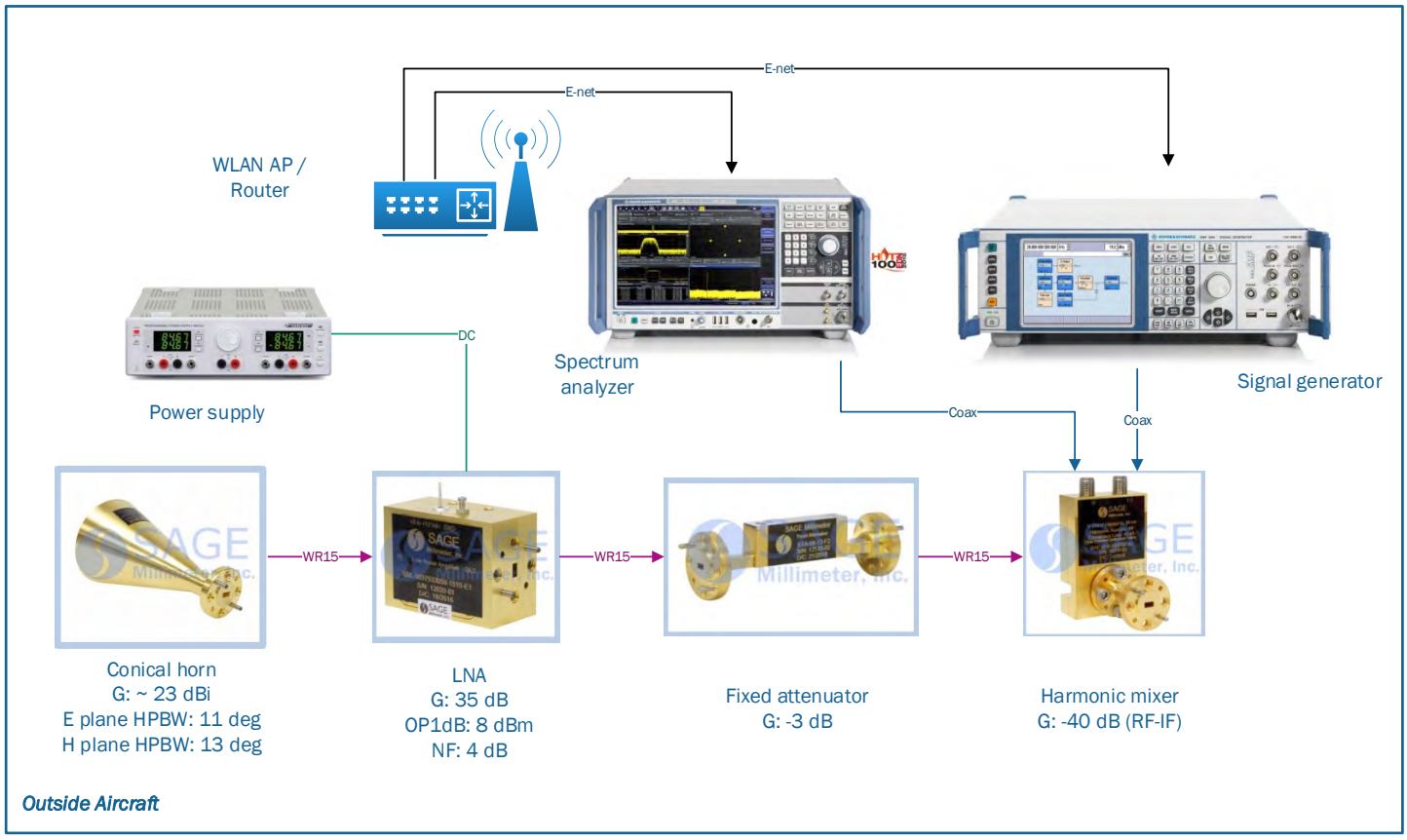

Figure B.4: Receive block diagram

Table B.2: Major items in the receive test setup.
Minor items such as RF cables, tripods or other mounting hardware are omitted from the table.

Component	Manufacturer	Model
Signal generator	Rohde&Schwarz	SMBV100A
Spectrum analyzer	Rohde&Schwarz	FSV7
Harmonic mixer (/14)	Sage Millimeter	SFH-15SFSF-A1
Fixed 3 dB attenuator	Sage Millimeter	STA-03-15-F2
LNA	Sage Millimeter	SBL-5037533550-1515-E1
Conical horn	Sage Millimeter	SAC-2309-15-S2

B.1.5 Receive Lineup Characterization

The conducted gain of the receive lineup is depicted in Figure B.5. This measurement data includes the LNA, 3 dB attenuator and harmonic mixer as depicted in Figure B.4. Measurements were recorded at an intermediate frequency (IF) of 1 GHz, the same frequency that is used in all measurements throughout this document. A brief inspection of the RX lineup conducted gain indicates a significant amount of frequency ripple. Though this ripple is significant and non-ideal, only relative changes in transmit-receive coupling are of interest.

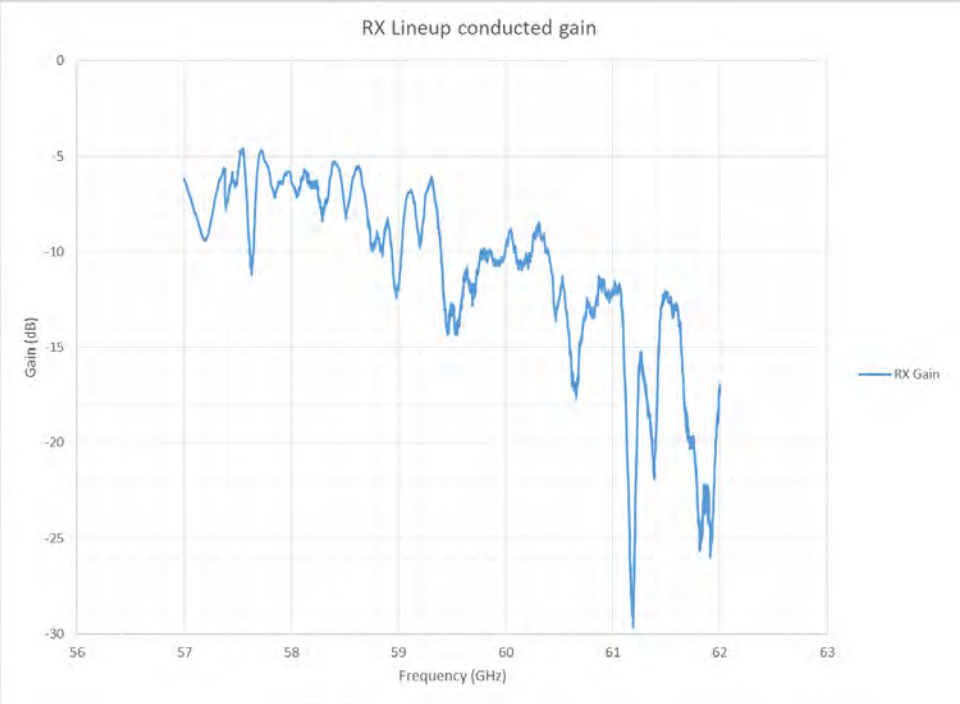

Figure B.5: Rx lineup conducted gain.

B.1.6 Aircraft Test Data

Two sets of measurements were performed on an aircraft. In both cases the receiver was placed on a scissor lift outside the aircraft, and the transmitter was placed inside the aircraft. The two sets of measurements include:

- Starboard door directly across from the port side passenger loading door. Measurement data was collected with the starboard door open as well as with the door closed. Measurements with the starboard door closed were collected to approximate the shielding of the aircraft.
- A second set of measurements were collected through the window at seat 12J. The transmitter orientation was varied in the azimuth (parallel with the aircraft floor) from 0 to 330 degrees in 30 degree steps.

B.1.7 Starboard Door Measurements

Figure B.6 provides a simple depiction of starboard door transmit and receive measurement locations. Figure B.7 depicts the measured power vs. frequency for the starboard door open and closed.

Test data observations:

- Measurement data through the open starboard door shows significant ripple over frequency. As highlighted in section B.1.5, this ripple is attributed to harmonic mixer and receive lineup performance in general. Measurements documented in E: Aircraft Fuselage Attenuation Testing show relatively little frequency ripple for similar types of measurements.
- The average difference between door-open and door-closed measurements is approximately 38.2 dB. This is within expectations from simulations.

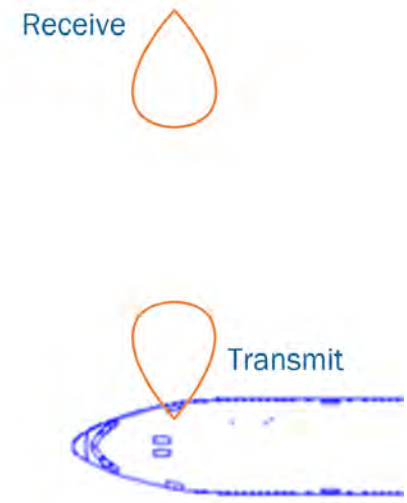

Figure B.6: Starboard door measurement location.

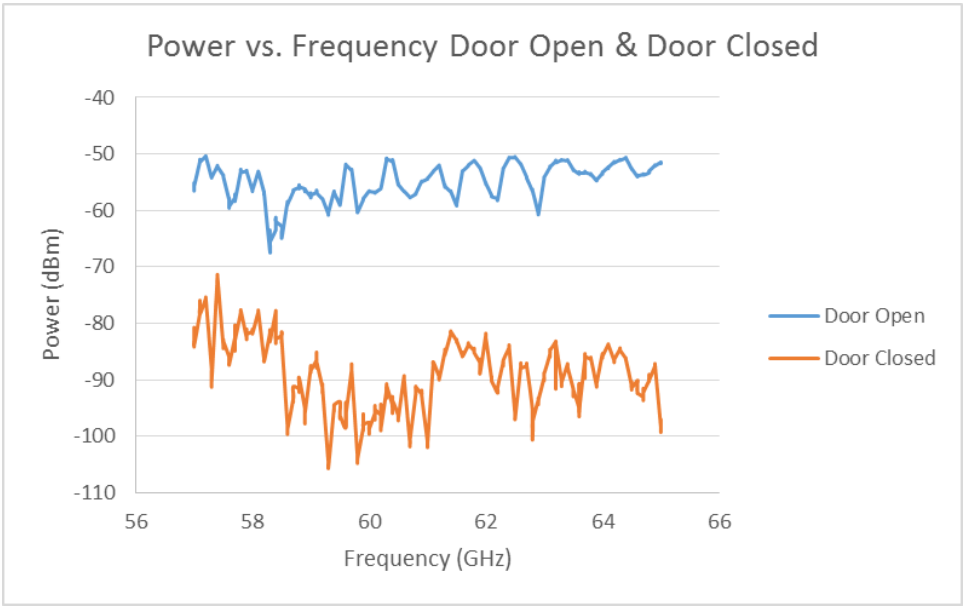

Figure B.7: Measured power vs. frequency with starboard door open and closed.

B.1.8 Measurements Through Window at Seat 12J

The measurement concept at seat 12J is depicted in Figure B.1 above, and a subset of measurement data at seat 12J is depicted in Figure B.8. The measurements in Figure B.8 include:

- Transmit pointing through the window at seat 12J directly at the receiver on a scissor lift. Transmit and receive antennas were aligned on boresight and co-polarized.
- Transmit orthogonal to receive (90 degrees) and pointing towards the tail of the aircraft.
- Transmit pointing directly opposite of receive (180 degrees) and towards the port sized of the aircraft.
- Transmit pointing orthogonal to receive (270 degrees) and pointing towards the nose of the aircraft.
- A reference, open door measurement.

Note: Reference measurements taken through the open starboard door were collected at a frequency step size of 0.1 GHz. Measurements at seat 12J were collected with a frequency step size of 0.01 GHz.

Observations from measurements in Figure B.8:

- Measurements at a TX azimuth of 0 degrees are similar to reference measurements made through the open starboard door. The difference in frequency response was likely due to transmit-receive alignment differences between reference (through door) and measurements collected at seat 12J. The overall average difference between the reference measurement and the measurement at seat 12J is approximately 0.7 dB. For all intents and purposes, this set of measurements indicates that the window is effectively lossless at this frequency. This is expected based on measurements and matches simulations.
- The average difference between a TX azimuth of 0 degrees and 90 or 270 degrees is 35 to 36 dB. This is in line with what was observed at the open vs. closed starboard door.
- The average difference between a TX azimuth of 0 degrees and 180 degrees is approximately 23 dB. This observation point is expected to be key in validating and / or adjusting ray tracing simulation parameters.

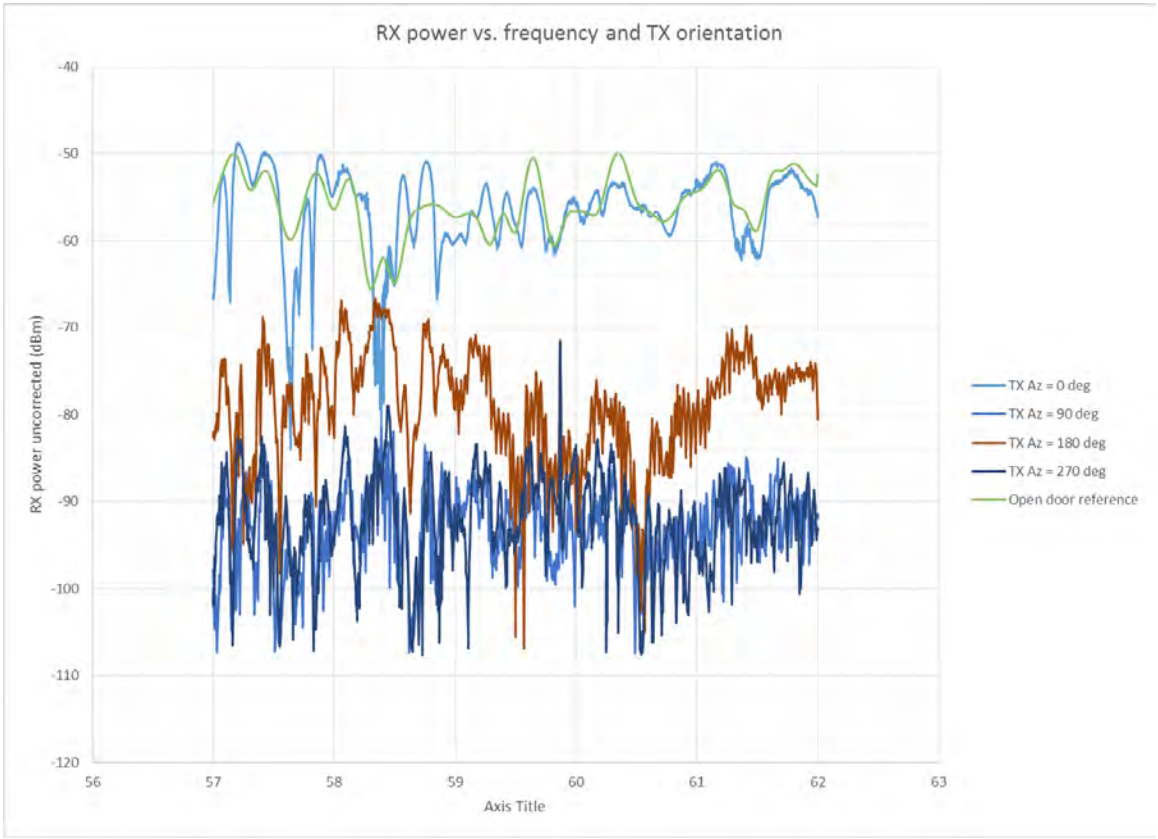

Figure B.8: RX power vs. frequency and transmit antenna orientation.
Measurement data is provided through an open starboard door as well as at seat 12J. Note: Open door reference data was taken at a frequency step size of 0.1 GHz while all other measurements were taken with a frequency step size of 0.01 GHz

Table B.3 provides a summary of the average difference between measurements at seat 12J vs. transmit azimuth angle. The difference is relative to the measurements at a transmit azimuth angle of 0 degrees; i.e. aligned (and co-polarized) with the receive antenna. The overall average difference between a TX azimuth of 0 degrees and all other steering angles is approximately 40.5 dB. This is

consistent with measurement results and reports from Annex E. (Note: Average values calculated based on linear values and converted to dB.)

Table B.3: Average difference between measured receive power at a transmit azimuth angle of 0 degrees (aligned with receive antenna boresight) and a sweep of transmit azimuth angles.

TX Azimuth (deg)	12J average delta (dB)
30	24.5
60	39
90	40.5
120	41.6
150	44.4
180	30
210	38.9
240	44.6
270	40.5
300	41
330	28.9

B.1.9 Summary

The goal of the on-aircraft testing in this annex was to support ray tracing simulations. The results of ray tracing simulations and ultimately aircraft emissions characteristics are summarized in Annex A: WiGig Aircraft Emissions Model. The data collected in Marana, AZ and summarized above were compared with ray tracing simulations to validate or adjust various simulation parameters.

The average difference between through window line of sight and non-line of sight measurements is approximately 41 dB.

C: Aircraft WiGig Performance Testing

This annex provides performance test results for Multi-Gigabit Wireless Devices (WiGig) On-Aircraft operating in the 57-71 GHz frequency range. Testing was conducted to quantify WiGig performance in the aircraft cabin as applicable to the use cases defined in Annex A, Section A.2 - Overview of WiGig On-Aircraft Use Cases, thereby validating the number and positions of access points used to establish the MEF used in the interference assessment.

The test results herein were obtained during ground testing aboard a Boeing 777-200. The test aircraft was located at Marana Airport, Tucson, AZ. The aircraft was fully equipped to support passenger airline operations.

The test aircraft had no IFE system in the seats. The aircraft cabin configuration as tested is illustrated in the Locations of Passenger Accommodations (LOPA) diagram in Figure C.1.

Figure C.1: Boeing B777-200 – LOPA.

C.1 Test Equipment

Multiple commercial laptops were used for performance testing. The particular model of laptop was chosen for its inbuilt WiGig-compliant radio and phased array antenna. A Notebook computer and separate access point were used to manage the laptops and record test results. During testing each laptop was configured as either an Access Point (AP) or a client Station (STA). The WiGig antenna in each laptop is located in the back of the screen. The antenna position in the laptop screen is denoted by a green rectangle that can be seen in the various photos.

C.2 Distance Measurements

C.2.1 Set-Up

Laptop TGS60-1 was configured as a WiGig Access Point and fixed above the aisle between seats 62C and 62D to approximate the position of a ceiling mounted access point. TGS60-1 was open with screen vertical, facing the rear of the aircraft so that the screen-mounted antenna faced forward. The height of the WiGig antenna was 2.1 meters above the cabin floor. To achieve this position TGS60-1 was positioned on top of a temporary platform between luggage bins consisting of three (3) collapsed baby bassinettes. Figure C.2 shows this set-up.

Laptop TGS60-2 was configured as a WiGig client. TGS60-2 was placed on top of a cardboard box positioned with the laptop body horizontal with the screen vertical. The screen was facing the front of the aircraft so the antenna faced the rear of the aircraft. The height of the WiGig antenna was 1.1 meter above the cabin floor.

Figure C.2: Distance Measurements – AP Set-up – Laptop TGS60-1.

Figure C.3: Distance Measurements – STA Set-up – Laptop TGS60-2.

C.2.2 Tests

The first measurement position was in the aisle between seats 61C and 61D. During the test a script recorded the slant range from the WiGig antenna in the screen of TGS60-1 to the WiGig antenna in the screen of TGS60-2 and then recorded the throughput for one minute. The distance from TGS60-1 to TGS60-2 was then increased and the test was repeated. The test continued until the TGS60-2 was no longer able to report measurable throughput.

Measurements were all Line of Sight (LoS) from row 61 to the front row of economy class. Distance measurements continued into business class section, but an offset of the aisle between business and economy somewhat inhibited LoS testing into business section. A total of 41 data points were taken

for 60 seconds each, over 34 meters. The distance change between measurements was approximately 80cm.

There were fixtures/monuments along the aisle distance measurement path that could have had some effect on test results. Table C.1 lists those fixtures/monuments along the test path and the distance of each from the access point during the test.

Table C.1: Distance Measurements – List of Fixtures/Monuments along the Test Path.

Fixture/Monument	Distance to the AP [m]
Overhead monitor	5.6
Exit sign	11.2
Port bulkhead	12.7
Center bulkhead	13.2
Overhead monitor	17.5
Section divider	22.2
Overhead monitor	25.4

C.2.3 Results

Figure C.4 depicts the results obtained during the distance measurements. The yellow line depicts the obtained mean data rate in each point. The red line depicts the most used MCS value (a.k.a. mode) for each measurement.

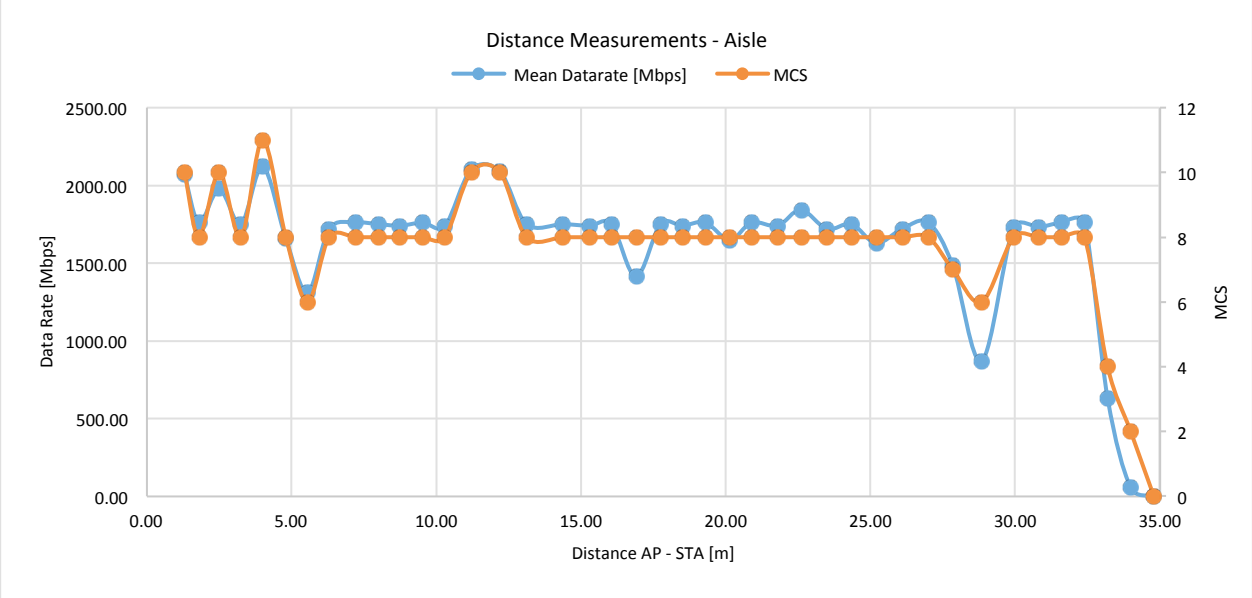

Figure C.4: Distance Measurements – Results.

As mentioned above, the link was maintained up to 34m with an averaged data rate of 1.75Gbps (in blue) until 32m (from this point on the data rate decreases until the link is broken at 35m). The most used data rate in this section is MCS8 (2,3Gbps @PHY).

During the test, there are some points in which the link is not stable (e.g. 28,85m), where the MCS value fluctuates a lot: at 28.85m the most used MCS is MCS6, but in this specific point this parameter jumps between constantly between MCS3 and MCS7.

In any case, compared to previous laboratory measurements with different WiGig devices, this test configuration is much more reliable and delivers a higher throughput for a longer LoS distance.

C.3 Coverage Measurements

C.3.1 Set-Up

The coverage measurements were run two times. The difference between tests was the location of the device acting as the AP (TGS60-1). In the first test the AP was positioned above the aisle; in the second test the AP was positioned beneath the luggage bin next to the window.

C.3.2 AP in the Aisle

The first coverage tests were run with the TGS60-1 acting as AP in the aisle position. For further details related to the AP's location, please refer to section C.2.1.

TGS60-2, again acting as STA, was strapped to a carry bag so it would stand upright on the passenger meal tray with the screen lying against the seat back (Figure C.5) to emulate a seatback display unit.

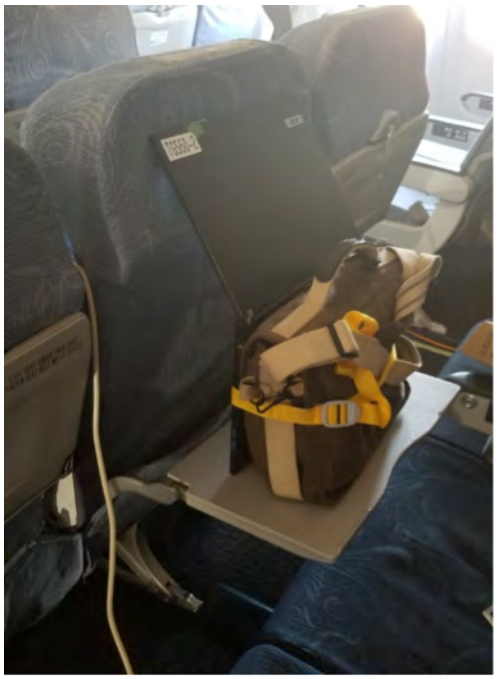

Figure C.5: Coverage Measurements – STA Set-up – Laptop TGS60-2.

C.3.3 AP Next to the Window

The coverage test was run a second time with TGS60-1 positioned above seat 62A. The B777-200 has near vertical walls above the window seats so the recommended positioning of the AP immediately beneath the luggage bin could not be accomplished. The laptop was instead hung beneath the luggage bin with the antenna as close to the luggage bin as possible with the screen fully open to direct the antenna somewhat downward (see Figure C.6).

Figure C.6: Coverage Measurements – AP Set-up – Window – Laptop TGS60-1.

C.3.4 Tests

Tests were run with the STA in alternate rows at seats xxA, xxF and xxL (where xx is the row number) for the length of the rear cabin section from rows 61 down to 49. Slant angle measurements between AP and STA antennas were taken at each seat location, when the AP was in the aisle.

When the AP was positioned next to the window, slant angle distance measurements were taken at the three (3) most extreme distances to give a reference for comparison to the previous (aisle AP) tests. All other tests recorded a distance value of 1 meter.

C.3.5 Results

Figure C.7 and Figure C.8 plot the data rate vs the distance (AP-STA) per seat "column" (A: blue, F: orange and L: grey). The numbers next to each point specify the seat row. The difference between plots, is the AP location.

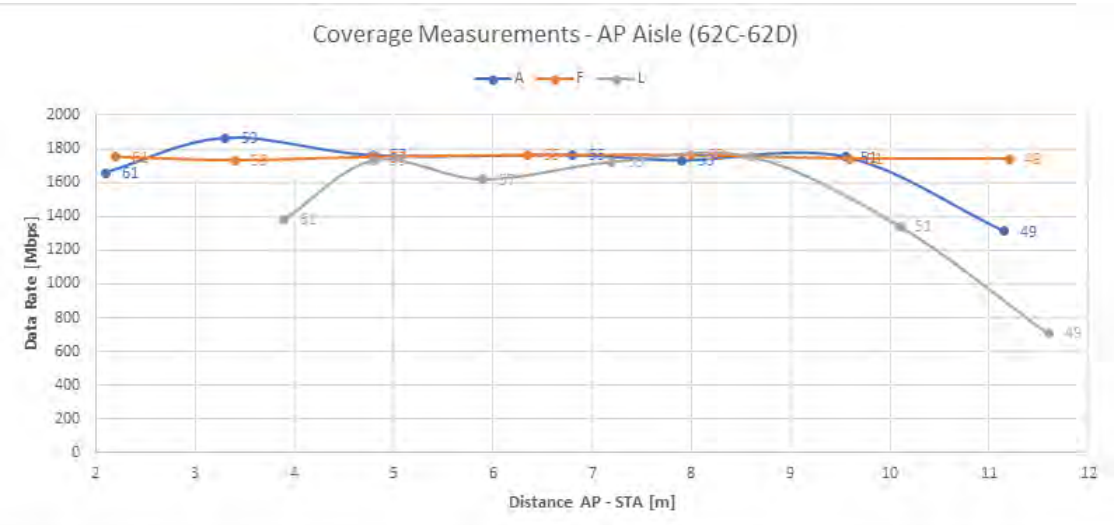

Figure C.7: Coverage Measurements – AP Aisle – Obtained Data Rate per Seat Column.

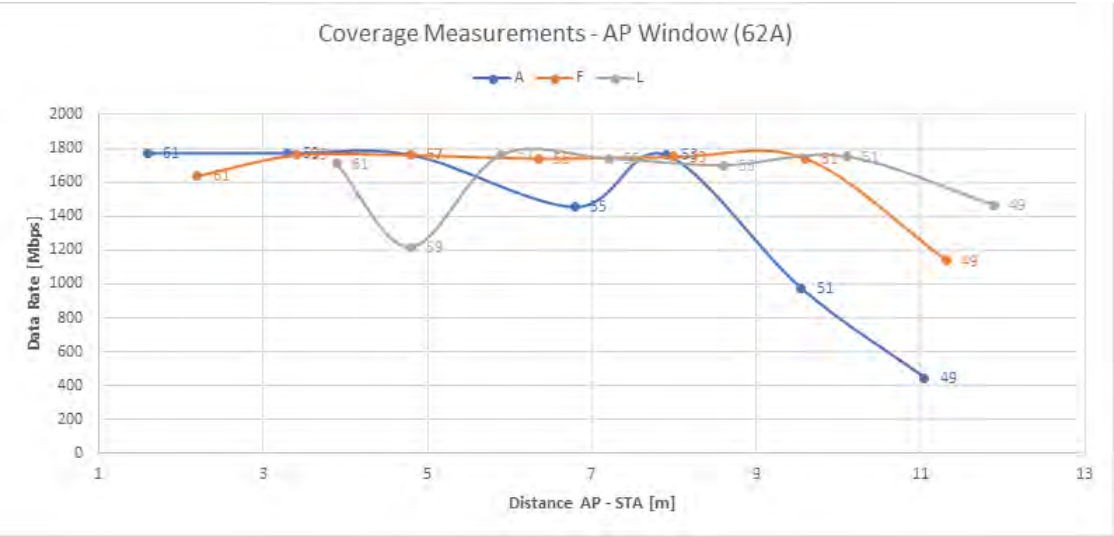

Figure C.8: Coverage Measurements – AP Window – Obtained Data Rate per Seat Column.

Both the aisle and window seat coverage tests were able to maintain connection to almost all seat positions with 1.5-1.8 GHz. The most used MCS is, again, MCS8.

From the previous plots, we can see that there are some points in which the data rate is lower than 1.5 Gbps. However, these points are not the same in both set-ups, that is to say, they depend on the position of the AP:

- When the AP is in the aisle: the least responsive points are located in the farther corners (49L-51L-49A-61L)

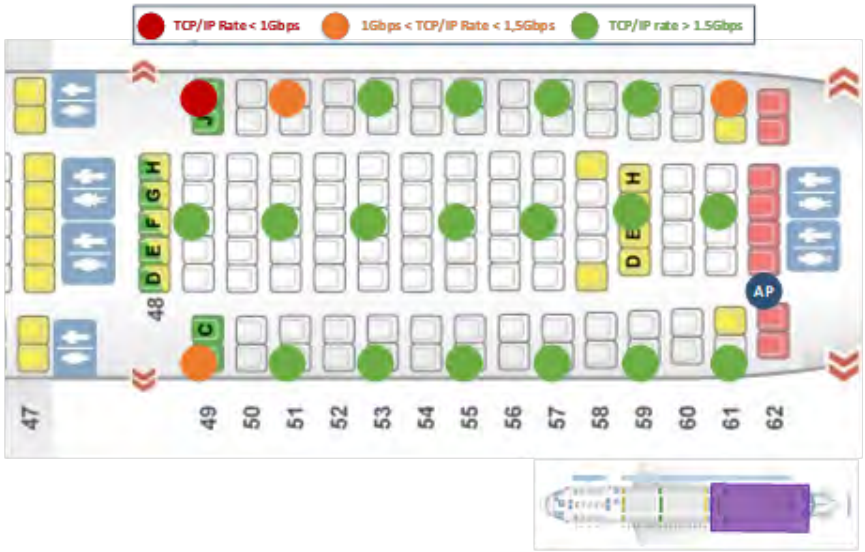

Figure C.9: Coverage Measurements – AP Aisle – Data Rate Map.

- When the AP is in next to the window: the least responsive test positions are closest to the near wall, that is, test locations in the same column (seats #A) at the farthest locations from the AP. These locations appear to be highly affected by reflections from the wall. Data rate/MCS values varied considerably on these seats.

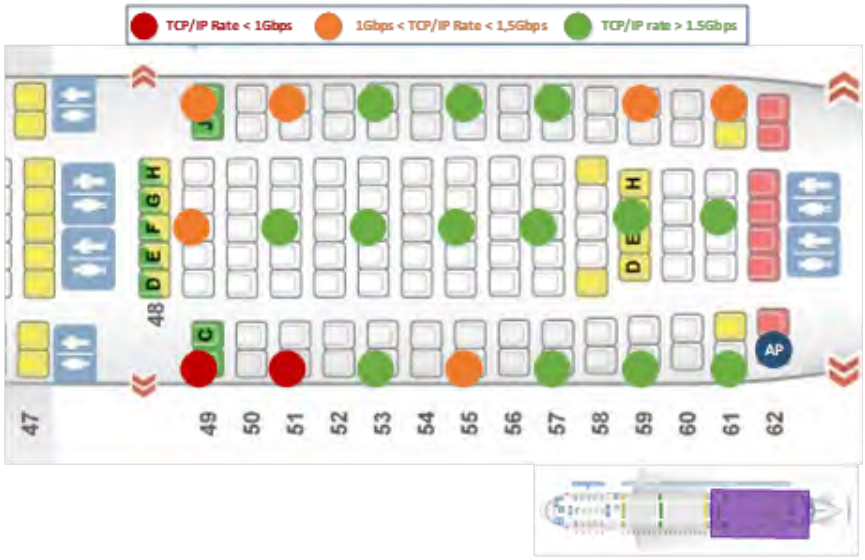

Figure C.10: Coverage Measurements – AP Window – Data Rate Map.

Even so, the minimum obtained data rate was 450Mbps (MCS1-3) for seat 49A in the coverage measurement in which the AP is close to the window. The averaged data rate for all points in both sets of measurements is 1.5 Gbps (MCS 8).

C.4 Conclusions

WiGig performance within the aircraft cabin was better than anticipated. Performance was adequate to provide approximately 1.5 Gbps to all locations within a given wide body aircraft section from a single access point positioned in the overhead above the aisle or below the luggage bins near the window. WiGig throughput was reduced by cabin monuments that separate cabin sections and by reflections along cabin walls.

Consistent with the use cases defined in Annex A: WiGig Aircraft Emissions Model a typical installation would require between 2 and 4 access points to be deployed per aircraft section between major monuments to ensure reliable, redundant coverage at every seat.

WiGig transmit power levels will have to be less than 30 dB to ensure efficient channel reuse in adjacent cabin sections.

Based on these performance tests, the total number of access points required for a typical wide body aircraft installation could vary from 16-24 in order to provide adequate coverage and bandwidth --well below the multiple equipment factor (MEF) used in the interference assessment. Therefore, the MEF used in the analysis is appropriate for determining potential interference to passive services from WiGig transmissions in the frequency range 57 – 71 GHz.

D: Fuselage Materials Comparison

The mechanism of how electromagnetic energy leaks through the skin of an aircraft fuselage is well understood. The dominant method of RF energy above 1 GHz leaking from an aircraft fuselage is through aircraft windows.

Most studies of fuselage shielding of wide-body commercial aircraft have been performed on aluminum-skinned aircraft. An aluminum-skinned aircraft was also used for this study due to the limited availability of aircraft types that employ Carbon Fiber Reinforced Plastics (CFRP) material as skin material, e.g. the Airbus A350 or the Boeing B787.

Manufacturers of aircraft with CFRP skins are obligated as part of their type certification to analyze and verify the conductivity of skin materials to ensure protection of aircraft occupants and electronics from repeated lightning strikes. The same conductivity that protects aircraft from lightning strikes is also a major contributor to fuselage RF attenuation.

Proprietary measurement campaigns conducted as part of Boeing 787 and Airbus A350 development and certification have shown that CFRP materials provide transmission losses in excess of 40 dB. The difference in RF attenuation of aircraft fuselage skin materials between aluminum and CFRP is negligible from the perspective of RF shielding.

E: Aircraft Fuselage Attenuation Testing

In order to accurately model how radio frequency emissions within an aircraft may impact systems outside the aircraft, measurements were taken to form a basis of understanding of fuselage attenuation in the frequency range 57 – 71 GHz. While there has been extensive fuselage attenuation testing below 15 GHz, testing above 57 has not been performed. Therefore, in order to better understand and quantify fuselage attenuation in this range, AVSI conducted a test campaign to measure these effects.

Measurements were conducted on a Boeing 777-200 aircraft in Marana, Arizona from June 26-30, 2017.

Figure E.1: AVSI Test Team and Boeing 777-200 aircraft.

E.1 Test Plan & Setup

This test plan for fuselage attenuation measurement consisted of four steps:

- Step A: Place a transmitter inside the cabin and measure the signal received outside the aircraft with the door open to obtain a reference measurement at a fixed distance (d1) for both Line of Sight (LOS) and non-LOS conditions
- Step B: With the doors closed move the transmitter inside the cabin and measure the signal received outside the aircraft to obtain data on the level of attenuation at a fixed distance (d2) under LOS condition.
- Step C: Rotate the transmitter position and repeat Step B to measure non-LOS conditions
- Step D: Calculate the difference between Steps B, C and A to determine the fuselage attenuation after correcting for distances.

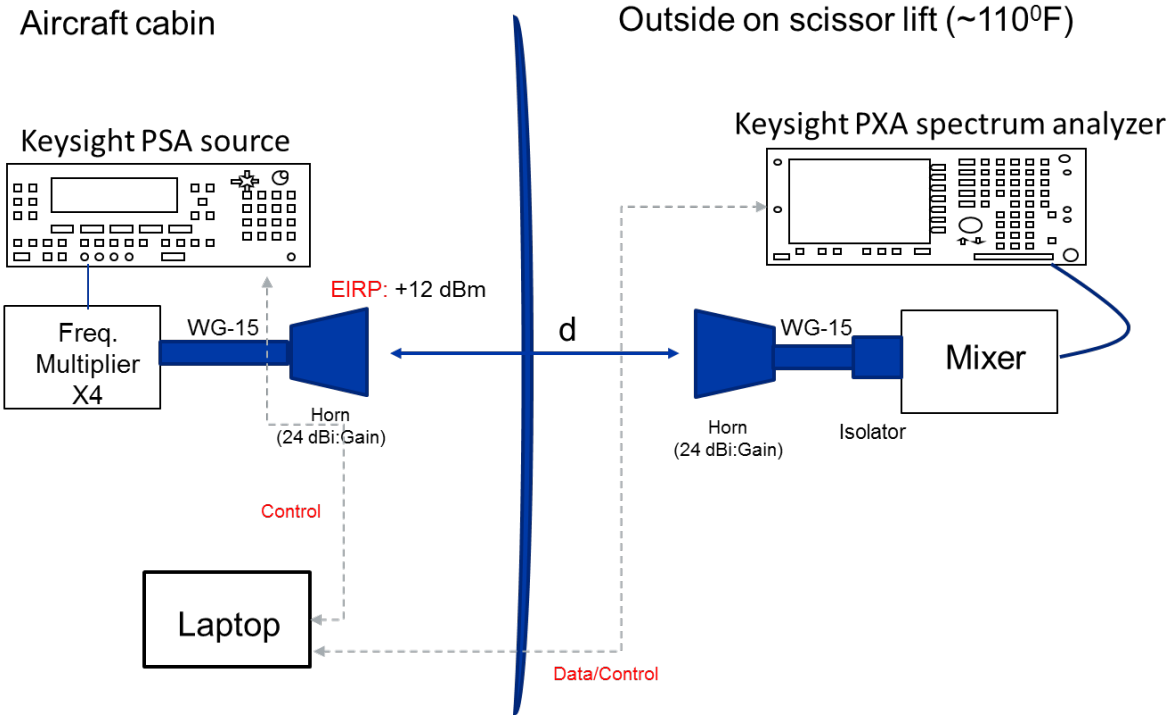

Figure E.2: Basic attenuation test setup.

The test set up consisting of transmit (Tx) and receive (Rx) sections is shown in Figure E.2. Application software on a laptop located in the aircraft cabin received the signal levels measured at the receiver via a fiber optic cable interface. The propagation path distance (d) between Tx and Rx antennas includes the blockage by the window and the fuselage material, and the effect of skew between the Tx and Rx antennas.

E.2 Reference Measurements

Reference measurements for distance are provided in Figure E.3. The distance corrected measurement is within 0.75 dB, which is reasonable for this type of measurement at this frequency range.

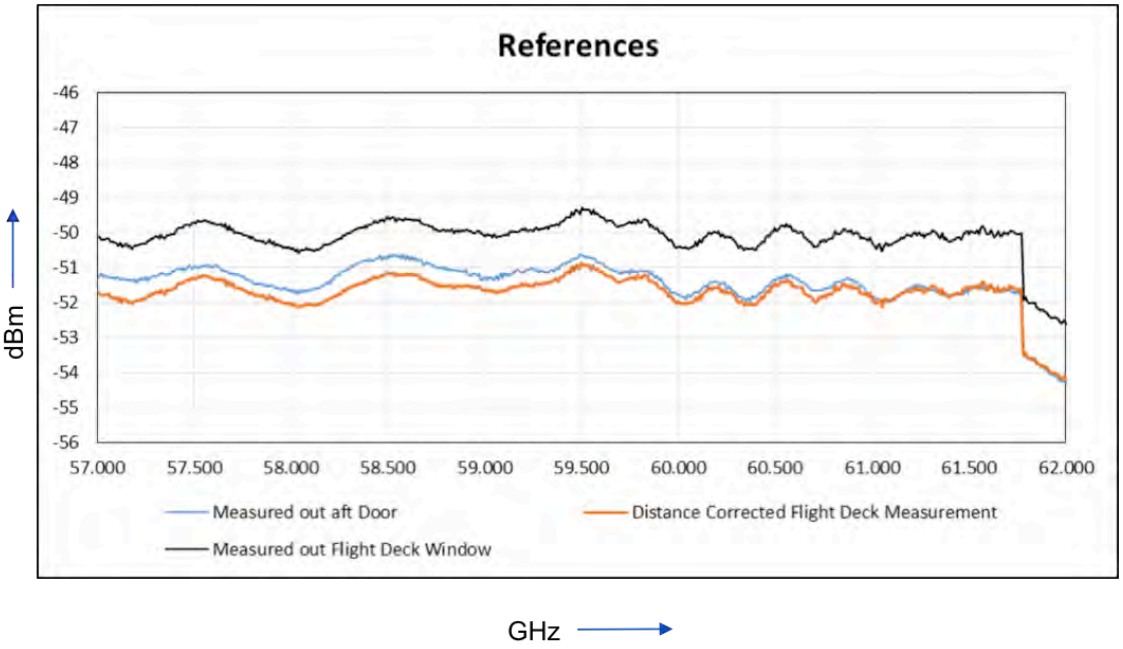

Figure E.3: Reference measurements.

Another element to consider is the aircraft's Q factor to determine the correlation between the samples. This is important to ensure that the samples are uncorrelated to eliminate bias. LoS and non-LoS measurements were taken with Tx and Rx antennas positioned at various points throughout the aircraft cabin for the purpose of establishing the appropriate measurement intervals and ensure uncorrelated results. Figure E.4 summarizes the analyses to establish the Q factor and establish the frequency interval unbiased testing. Figure E.5 illustrates the data taken as part of establishing the correlation between samples.

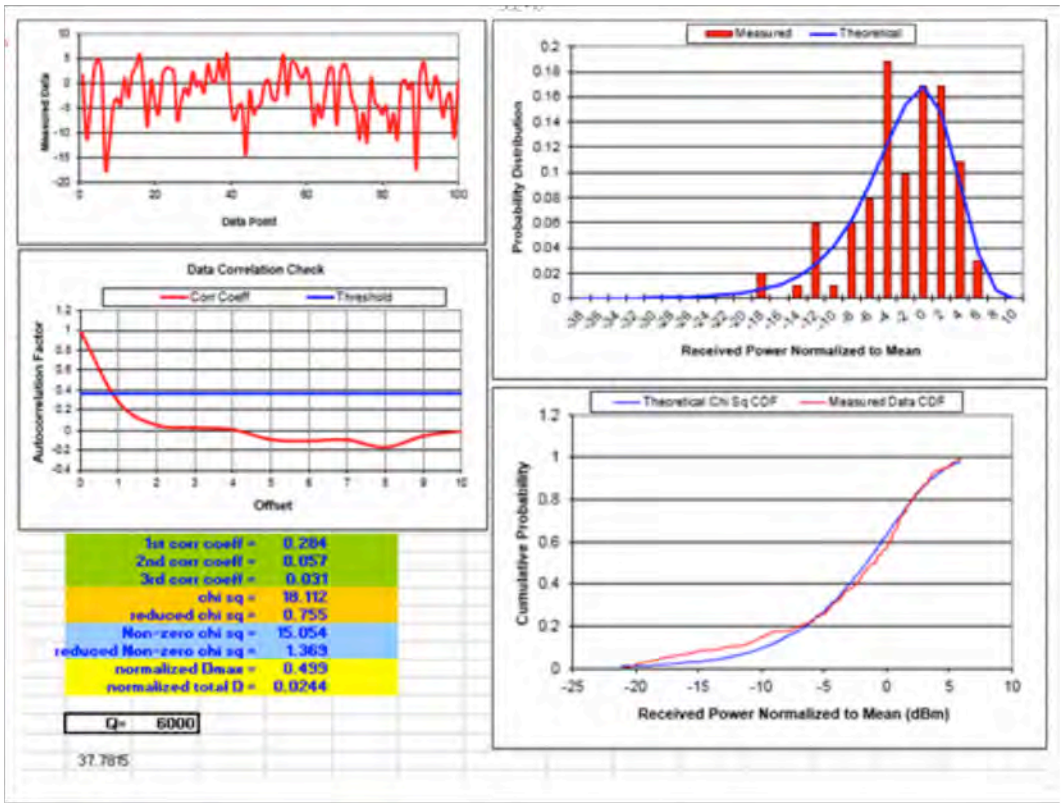

Figure E.4: Determining correlation.

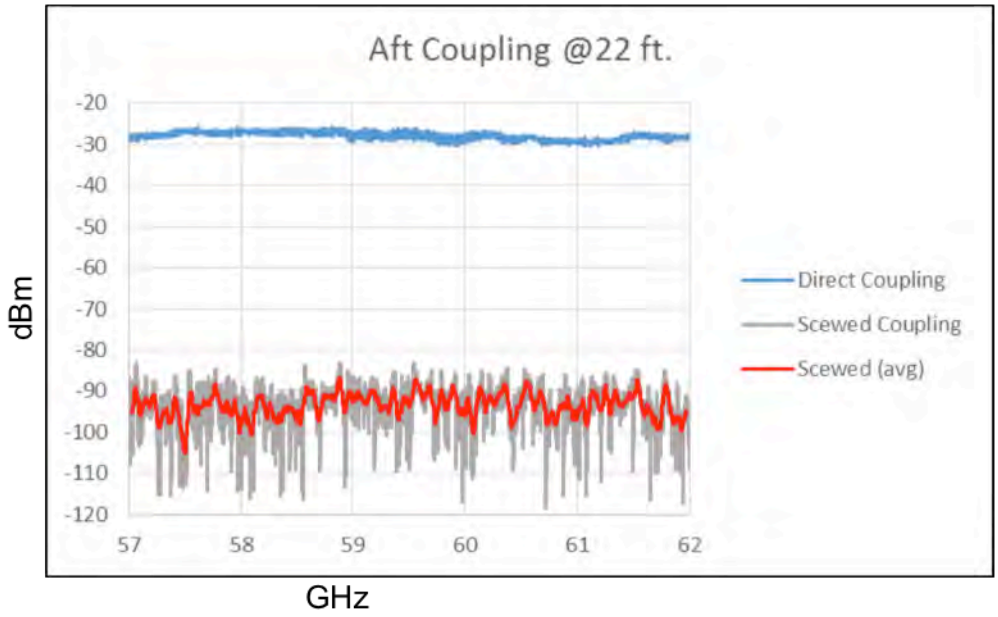

Figure E.5: Data from aircraft cabin.

Pearson's r autocorrelation check was used to determine if the data is uncorrelated:

$$r = \frac{\sum_i (x_i - \bar{x})(y_i - \bar{y})}{\sqrt{\sum_i (x_i - \bar{x})^2}\sqrt{\sum_i (y_i - \bar{y})^2}}$$

In the equation above, the x's represent a data set and the y's represent the same data set shifted by one so that x_2 has become y_1 and x_3 has become y_2, etc. It is uncorrelated when r is less than $1/e$.

The measurements indicated that if the samples were taken at 10 MHz intervals then they would be uncorrelated.

E.3 Cabin Fuselage Attenuation

While the aircraft fuselage provides a certain level of attenuation, the windows of the aircraft typically provide less attenuation and must be characterized to obtain an average aircraft attenuation.

E.4 Cabin Window Attenuation

Three line of sight (LoS) measurements were made in the configurations shown in Figure E.6 to determine the effects of aircraft cabin windows. The first test measured purely free space with a reference distance of 283 inches. The second test measured directly through a window with the transmitter located 19 inches from the window to establish the LoS attenuation through the window. The third test measured directly through a window with the transmitter located 101 inches inboard from the window to determine any additional attenuation effects due to window aperture.

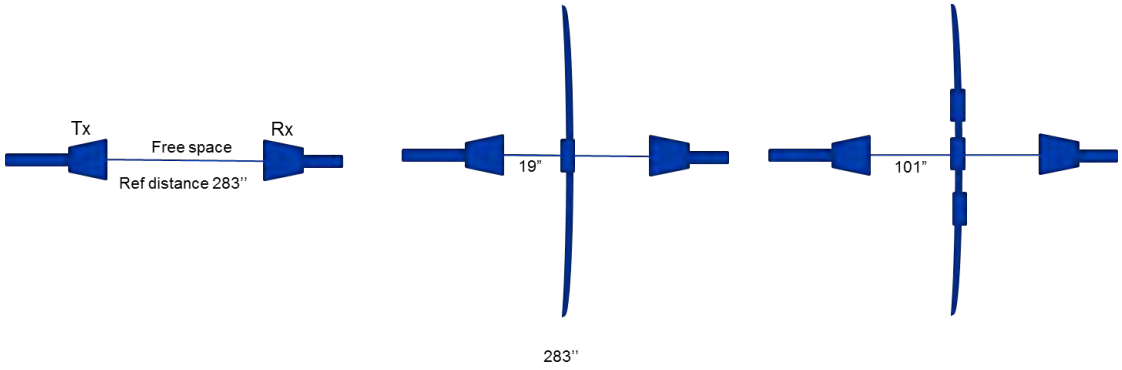

Figure E.6: Three measurement configurations.

Figure E.7: Free space attenuation measurement setup.

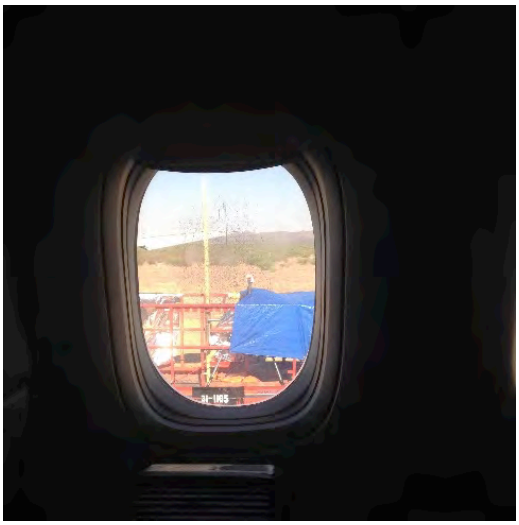

Figure E.8: Transmit antenna 19" from the passenger window.

Figure E.9: Transmit antenna 101" from the passenger window.

A comparison of the test results is shown in Figure E.10. The measurement at 19 inches directly through the window verifies that the window offers little attenuation. This was expected given the lack of shielding or electronic shading system found on newer aircraft. The measurement at the 101 inch distance illustrates the increased attenuation due to aperture effects and blockage by the fuselage structure surrounding the window.

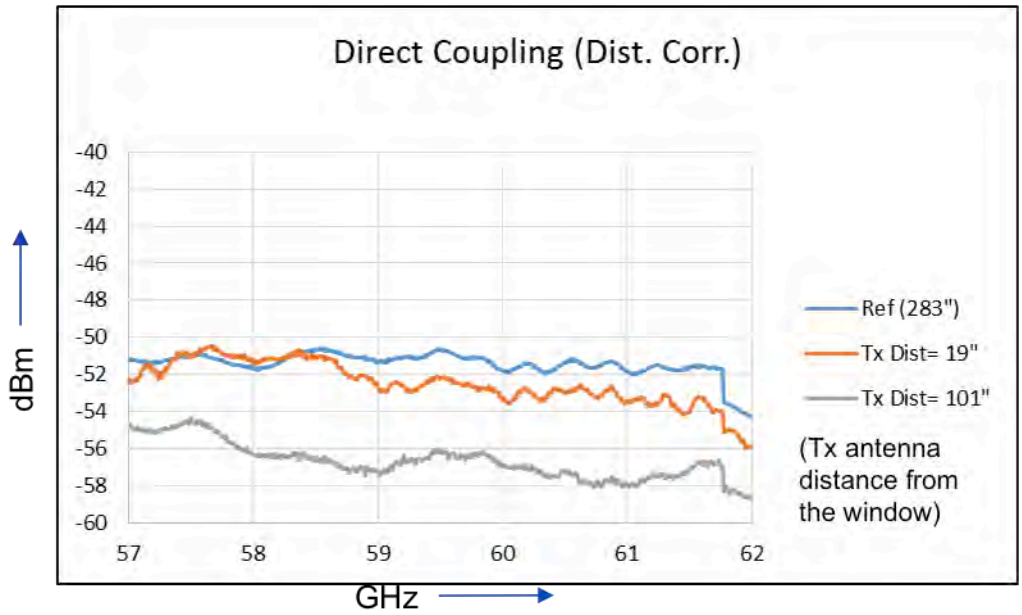

Figure E.10: Comparison of cabin window LoS signal levels.

In a typical aircraft WiGig system installation, transmitters will not be pointing directly through the windows. WiGig focuses transmissions between devices within the aircraft using beam steering to optimize throughput. Any WiGig emission out a window will be indirect from the transmit side lobes or the transmission reflecting at least once while incurring some indeterminate amount of attenuation in the process.

E.5 Cabin Attenuation

The next series of measurements were undertaken to determine attenuation in the cabin environment from sources more typical of a planned cabin installation and usage. The purpose of these measurements was to determine overall attenuation effects of the aircraft fuselage.

Non-LoS measurements were taken by rotating or skewing the Tx antenna at various points within the aircraft cabin relative to a fixed Rx antenna outside an aircraft cabin window.

The Rx antenna was positioned outside of the aircraft at a distance of 267 in (22.22 ft.) positioned vertically to match the height of the cabin window.

Two tests were performed in the passenger cabin of the Boeing 777-200; the first with the Tx antenna located at 19 inches from the cabin window and the second with the Tx antenna 101 inches from the cabin window. Measurements were taken with the Tx antenna rotated and skewed in a sequence of non-LoS directions.

A third non-LoS test was performed with the transmitter positioned in an overhead storage bin, as shown in Figure E.11.

Figure E.11: Transmitter in overhead storage bin.

In LoS tests attenuation inside the aircraft closely followed the path loss model:

$$\frac{P_r}{P_t} = G_t G_r \left(\frac{\lambda}{4\pi R}\right)^2$$

However, non-LoS test data needed to be statistically processed in order to determine fuselage attenuation characteristics. LoS and unprocessed non-LoS data are shown in Figure E.12.

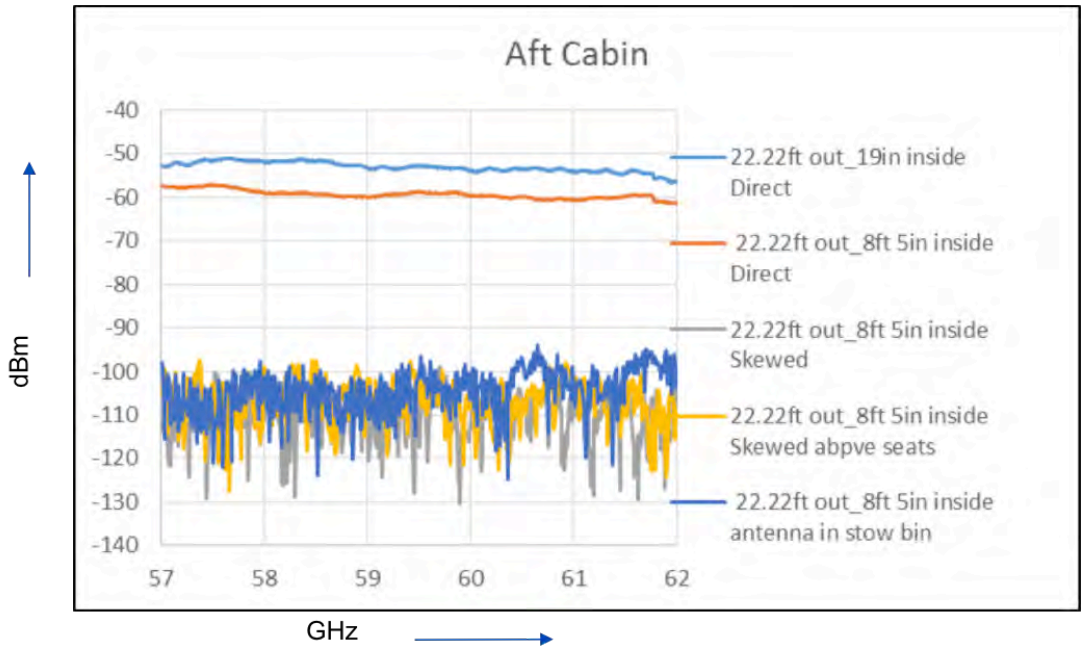

Figure E.12: Fuselage attenuation data.

The processed cabin measurement data results in the fuselage attenuation values in Figure E.13.

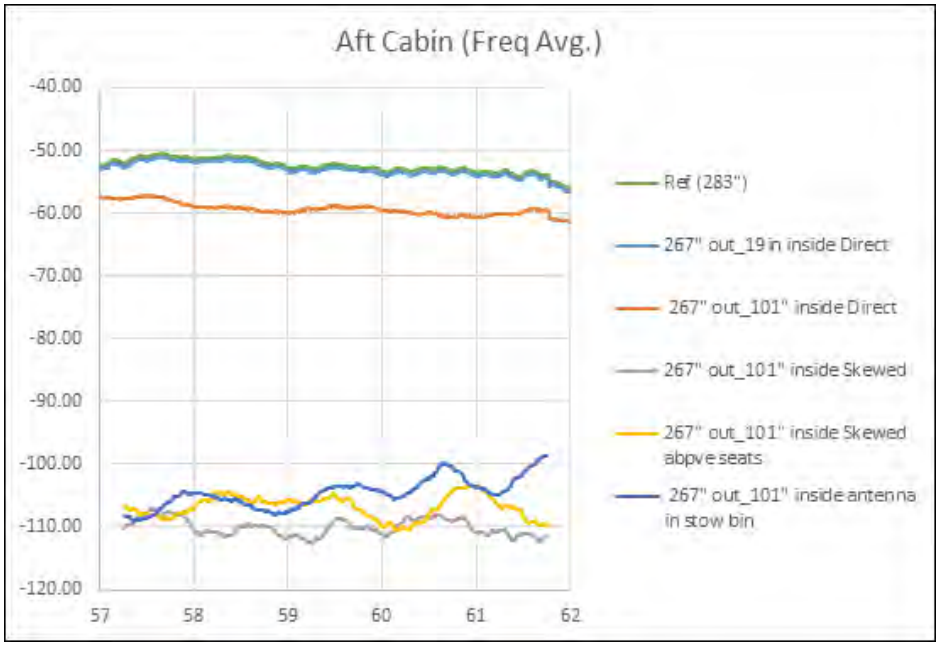

Figure E.13: Attenuation from the fuselage.

The key observation is that non-LoS transmissions in the frequency range 57 – 62 GHz inside the cabin are attenuated by about 40 dB relative to the direct LOS signal. For instance, the 267" LoS signal averages to about -60 dBm while the same signal skewed would average about -105 dBm.

E.6 Flight Deck Window Attenuation

Measurements were also taken from the aircraft flight deck to quantify the effects of window coating on attenuation. The window coating is used primarily for preventing or removing ice that can form on flight deck windows.

The measurement set up is as shown in Figure E.14. An initial LoS measurement was taken through an open flight deck window to establish an attenuation reference. The LoS measurement was then repeated with the window closed to measure the effect of the window. As a finally step, a series of non-LoS measurements were taken to measure the attenuation experienced due to indirect radiation.

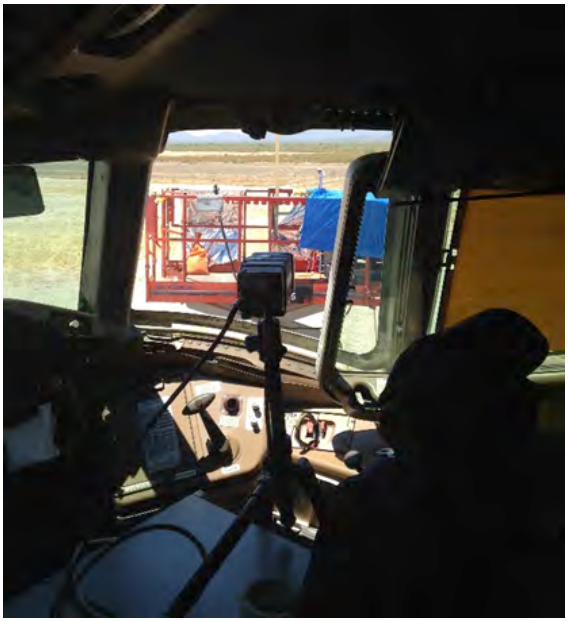

Figure E.14: Flight deck window test setup.

The blue trace in Figure E.15 illustrates the attenuation straight through the window when transmit and receive antennas are in alignment.

Cockpit windows are coated with indium tin oxide (ITO) for defrosting purposes. The orange trace in Figure E.15 shows that the ITO coating increases the attenuation of the 60 GHz LoS RF signal by approximately 25 dB.

Throughout the non-LoS measurements the transmit antenna was methodically skewed horizontally and vertically to measure the attenuation of the transmitted signal from inside the closed flight deck. The red trace in Figure E.15 shows that there is an additional 40 dB of attenuation through the flight deck window when there is no LoS RF path.

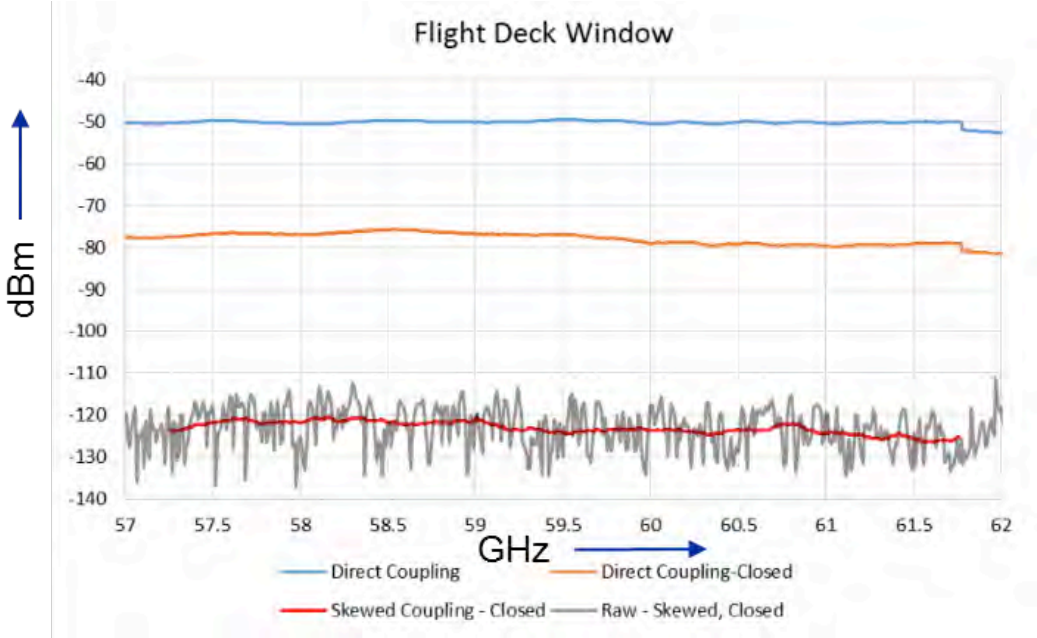

Figure E.15: Flight deck window attenuation.

Figure E.16 plots the difference in the attenuation between a non-coated passenger cabin window and a coated flight deck window.

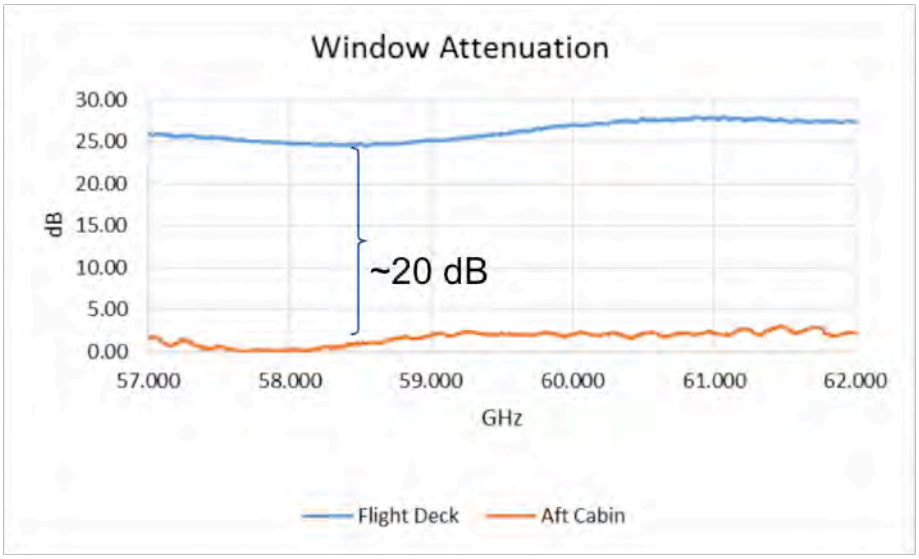

Figure E.16: Coated and non-coated window comparison.

E.7 Aircraft Attenuation Summary

From the tests performed on the Boeing 777-200 aircraft in Marana, Arizona several observations can be made.

WiGig MAC layer protocols incorporate continuous beam forming and beam steering functions to optimize communications between devices. WiGig devices cannot transmit directly out of an aircraft window during normal communications because there is no associated device outside the window with which to communicate. WiGig emissions outside of the aircraft will be the result of non-LoS emissions from side lobes or signals bounced off of one or more interior surfaces.

Non-LoS measurements of RF emissions transmitted from within the aircraft cabin show the fuselage attenuation to be about 40 dB. RF emissions from within the aircraft flight deck are reduced an additional 25 dB when window coatings are present.

LoS measurements are important to understand the attenuation of RF through aircraft windows and the modality of the aircraft interior but such measurements are of limited utility when considering potential interference to EESS from 60 GHz wireless systems operating in aircraft. The speed EESS satellites and the varying trajectories of commercial aircraft make alignment of emitters through aircraft cabin windows with EESS sensors extremely unlikely. If LoS interference between an emitter on aircraft and an EESS sensor were to occur it will be of extremely short duration.

All RF measurements were taken with the external receiver on a common horizontal plane with the center of the passenger windows. Previous fuselage test campaigns have shown this to be the worst-case angle for attenuation about the aircraft's longitudinal axis.

Measurements of non-LoS attenuation from the closed flight deck to an external antenna varied from -111 to -138 dB through a wide range of angles and azimuth, or 32-52 dB below measured LoS. Measured flight deck non-LoS attenuation stayed within this range regardless of transmitter angle despite being a highly RF reflective environment. Attenuation measurements taken outside the passenger cabin match those taken in the flight deck and further reinforce the position that a value of 40 dB for fuselage attenuation is appropriate when conducting sharing studies with incumbent services.

F: Reference Area Definition for Dynamic Simulation

Recommendation ITU-R RS.2017 defines that aggregate emissions should be evaluated within a reference two million square kilometer area (2e6 km^2). However, no criteria are provided for establishing the appropriate location or the orientation of that area.

Air traffic over CONUS is cyclic, with high traffic volumes over the east coast states in the morning EST, high volumes over the lower Rocky Mountains at mid-day, high volumes again in the eastern states in early evening and high volumes on the west coast a few hours later. For reference, Figure F.1, generated by www.flightradar24.com, is a snapshot of commercial air traffic over the continental United States taken at 1800 EST on 8 February 2017 based on transmitted ADS-B data.

The black rectangle in Figure F.1 represents the two million square kilometer area chosen for interference analysis of airborne 60GHz emitters with EESS.

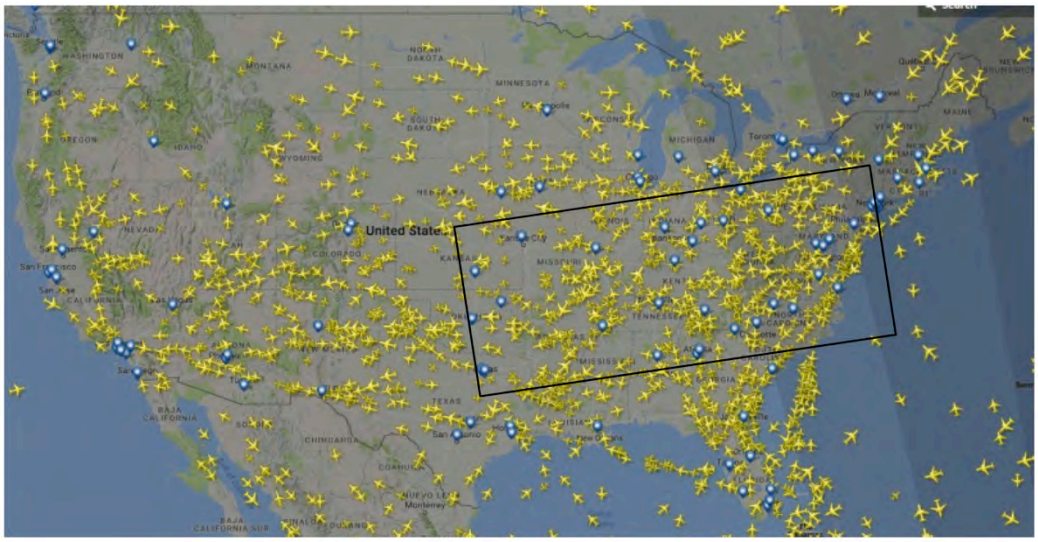

Figure F.1: CONUS Air Traffic 1800 8 February 2017.

This area was chosen after an informal assessment of commercial air traffic on www.flightradar24.com to identify the area in CONUS with the highest volume of air traffic over a 24 hour period. The rectangle encompasses traffic between several of the busiest airports in the United States: Atlanta, Chicago, Dallas/Fort Worth, Newark and New York.

The width of the rectangle (2187 km) was chosen to match the width of the sweep of the G2 sensor from Recommendation ITU-R RS.1861, being generally representative of the width of a nadir sweep. Thereafter the rectangle's height (914 km) was calculated to achieve a 2e6 km2 area.

The rectangle has been positioned laterally to overlay the highest number of transient aircraft in the US rather attempting to align the rectangle with the ground track of any particular satellite due to sun synchronization. The same reference area will be used for interference assessment of all nadir cross-track and conical satellite sensors.

Coordinates of the rectangle corners are approximately:

39° 41.3'N 98° 35.219'W 40° 13.572'N 75° 28.07'W

31° 32.02'N 97° 9.493'W 32° 4.333'N 74° 1.581'W

G: EESS Satellite and Dynamic Simulation Set-up

This annex summarizes the data provided by NOAA for current and planned EESS that was used to identify at-risk sensors for use in the interference assessment. The K2 and K3 sensors were identified operating in frequencies that could be affected by OoB and/or spurious emissions from WiGig transceivers.

Ephemeris data for the K2 and K3 satellites is evaluated to determine their ground tracks in relationship to the interference reference area defined in Annex F.

Table G.1: K2 and K3 sensor overlap with WiGig harmonics.

3rd Order Sub Harmonics:	19.0 - 23.66 GHz	Sensor K2:	Mechanical nadir scan, Alt: 824km, Inclination: 98.7°, Eccentricity.: 0, Repetition Period: 9 days
2nd Order Sub Harmonics:	28.5 - 35.5 GHz	Sensor K3:	Mechanical nadir scan, Alt: 833/822km, Inclination: 98.6/98.7°, Eccentricity.: 0/0.001, Repetition Period: 9/29 days
Fundamentals:	57.0 - 71.0 GHz		
2nd Order Harmonics:	114.0 – 142.0 GHz		
3rd Order Harmonics:	171.0 – 213.0 GHz		

Table G.2: NOAA current and planned EESS.

Satellite	Launch	EoI	lower freq (MHz)	upper freq (MHz)	sensor referenced in table 14 of RS. 1813	falls within
JPSS-1	≥2017-09	≥2024	54200	54600	K2	
JPSS-2	≥2021	≥2028	54200	54600	K2	
JPSS-3	≥2026	≥2033	54200	54600	K2	
JPSS-4	≥2031	≥2038	54200	54600	K2	
NOAA-15	13.05.1998	≥2017	54200	54600	K3	
NOAA-18	20.05.2005	≥2017	54200	54600	K3	
NOAA-19	06.02.2009	≥2017	54200	54600	K3	
SNPP	28.10.2011	≥2017	54200	54600	K2	
JPSS-1	≥2017-09	≥2024	54740	55140	K2	
JPSS-2	≥2021	≥2028	54740	55140	K2	
JPSS-3	≥2026	≥2033	54740	55140	K2	
JPSS-4	≥2031	≥2038	54740	55140	K2	
NOAA-15	13.05.1998	≥2017	54740	55140	K3	
NOAA-18	20.05.2005	≥2017	54740	55140	K3	
NOAA-19	06.02.2009	≥2017	54740	55140	K3	
SNPP	28.10.2011	≥2017	54740	55140	K2	
JPSS-1	≥2017-09	≥2024	55335	55665	K2	
JPSS-2	≥2021	≥2028	55335	55665	K2	
JPSS-3	≥2026	≥2033	55335	55665	K2	
JPSS-4	≥2031	≥2038	55335	55665	K2	
NOAA-15	13.05.1998	≥2017	55335	55665	K3	
NOAA-18	20.05.2005	≥2017	55335	55665	K3	
NOAA-19	06.02.2009	≥2017	55335	55665	K3	
SNPP	28.10.2011	≥2017	55335	55665	K2	

Satellite	Launch	Eol	lower freq (MHz)	upper freq (MHz)	sensor referenced in table 14 of RS. 1813	falls within
JPSS-1	≥2017-09	≥2024	57.125.344	57.455.344	K2	fundamental band
JPSS-2	≥2021	≥2028	57.125.344	57.455.344	K2	fundamental band
JPSS-3	≥2026	≥2033	57.125.344	57.455.344	K2	fundamental band
JPSS-4	≥2031	≥2038	57.125.344	57.455.344	K2	fundamental band
NOAA-15	13.05.1998	≥2017	57.125.344	57.455.344	K3	fundamental band
NOAA-18	20.05.2005	≥2017	57.125.344	57.455.344	K3	fundamental band
NOAA-19	06.02.2009	≥2017	57.125.344	57.455.344	K3	fundamental band
SNPP	28.10.2011	≥2017	57.125.344	57.455.344	K2	fundamental band
JPSS-1	≥2017-09	≥2024	53849	54047	K2	
JPSS-2	≥2021	≥2028	53849	54047	K2	
JPSS-3	≥2026	≥2033	53849	54047	K2	
JPSS-4	≥2031	≥2038	53849	54047	K2	
NOAA-15	13.05.1998	≥2017	53849	54047	K3	
SNPP	28.10.2011	≥2017	53849	54047	K2	
NOAA-18	20.05.2005	≥2017	53849	54047	K3	
NOAA-19	06.02.2009	≥2017	53849	54047	K3	
JPSS-1	≥2017-09	≥2024	53859	54037	K2	
JPSS-2	≥2021	≥2028	53859	54037	K2	
JPSS-3	≥2026	≥2033	53859	54037	K2	
JPSS-4	≥2031	≥2038	53859	54037	K2	
SNPP	28.10.2011	≥2017	53859	54037	K2	
NOAA-15	13.05.1998	≥2017	53859	54037	K3	
NOAA-18	20.05.2005	≥2017	53863	54033	K3	
NOAA-19	06.02.2009	≥2017	53863	54033	K3	
JPSS-1	≥2017-09	≥2024	53863	54033	K2	
JPSS-2	≥2021	≥2028	53863	54033	K2	
JPSS-3	≥2026	≥2033	53863	54033	K2	
JPSS-4	≥2031	≥2038	53863	54033	K2	
SNPP	28.10.2011	≥2017	53863	54033	K2	
NOAA-15	13.05.1998	≥2017	53863	54033	K3	
NOAA-18	20.05.2005	≥2017	53865.5	54030.5	K3	
NOAA-19	06.02.2009	≥2017	53865.5	54030.5	K3	
JPSS-1	≥2017-09	≥2024	53865.5	54030.5	K2	
JPSS-2	≥2021	≥2028	53865.5	54030.5	K2	
JPSS-3	≥2026	≥2033	53865.5	54030.5	K2	
JPSS-4	≥2031	≥2038	53865.5	54030.5	K2	
NOAA-15	13.05.1998	≥2017	53865.5	54030.5	K3	
SNPP	28.10.2011	≥2017	53865.5	54030.5	K2	
NOAA-18	20.05.2005	≥2017	53828	54068	K3	
JPSS-1	≥2017-09	≥2024	53828	54068	K2	
JPSS-2	≥2021	≥2028	53828	54068	K2	
JPSS-3	≥2026	≥2033	53828	54068	K2	
JPSS-4	≥2031	≥2038	53828	54068	K2	
NOAA-15	13.05.1998	≥2017	53828	54068	K3	
SNPP	28.10.2011	≥2017	53828	54068	K2	
NOAA-18	20.05.2005	≥2017	53859	54037	K3	
NOAA-19	06.02.2009	≥2017	53859	54037	K3	

G.1 EESS Ground Track in Relationship to Reference Area

Ephemeris data of the EESS satellite is available for 7 days from System Tool Kit (STK), cf. Figure G.1, which shows a plot of the satellite ground tracks and the 2e6 km^2 reference area. The essential satellite orbits parameters are given in ITU-R RS.1861 [6].

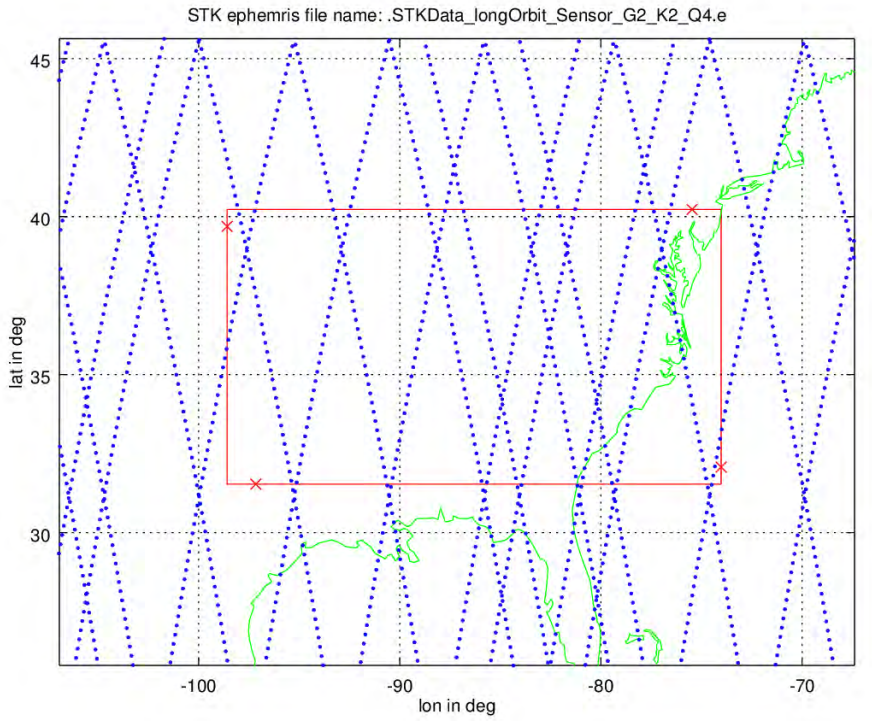

Figure G.1: Simulated satellite ground tracks (blue) from STK ephemeris data and 2e6 km^2 reference area (red).

In addition to the satellite movement along its track, the dynamic simulation also includes simulating the sensor scanning pattern, including off-nadir pointing angle and beam dynamics (based on the information given in ITU-R RS.1861 [6]). Figure G.2 shows the areas inside and outside the reference area covered by the sensor scans.

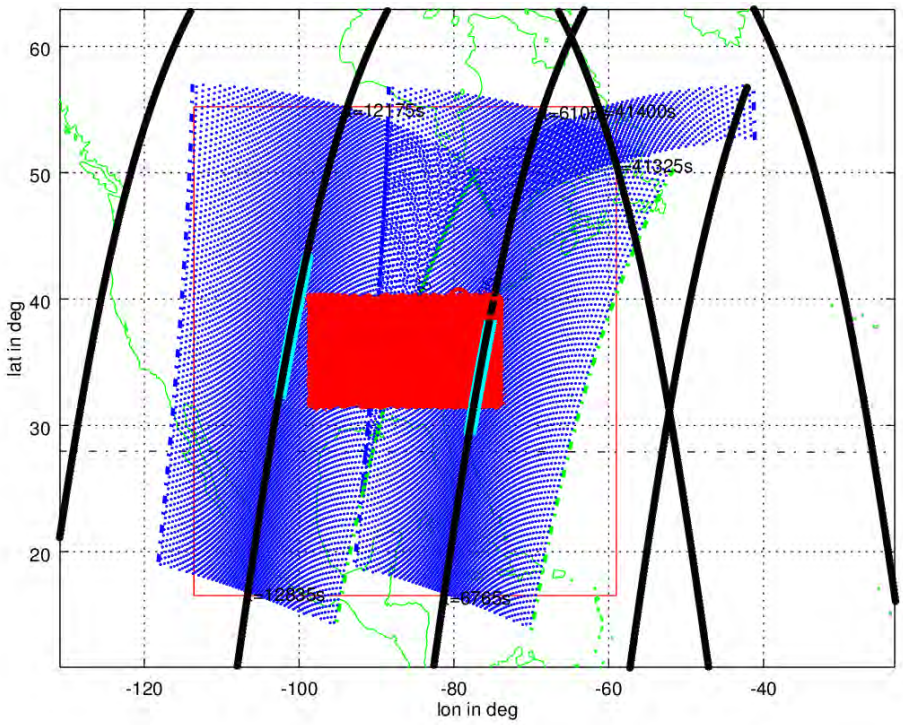

Figure G.2: Satellite tracks and scanned points for a 12 h period.
Black: satellite tracks, Blue: scanned points, Red: scanned points in reference area. Cyan: orbit track segments that correspond to scan points in reference area. Sample time is 20 ms.

Figure G.3 shows the applicable sensor gain pattern, which is defined in ITU-R RS.1813 [9] and Figure G.4 and Figure G.5 show how the sensor covers the reference area (using contour plots).

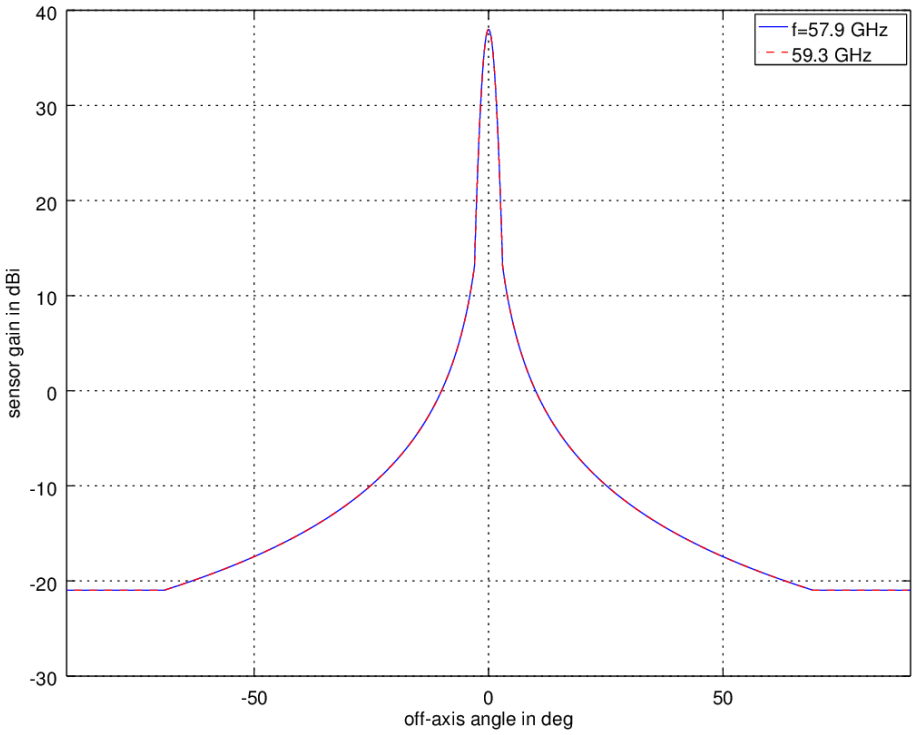

Figure G.3: Sensor gain vs. off-axis angle (according to ITU-R RS.1813-1).

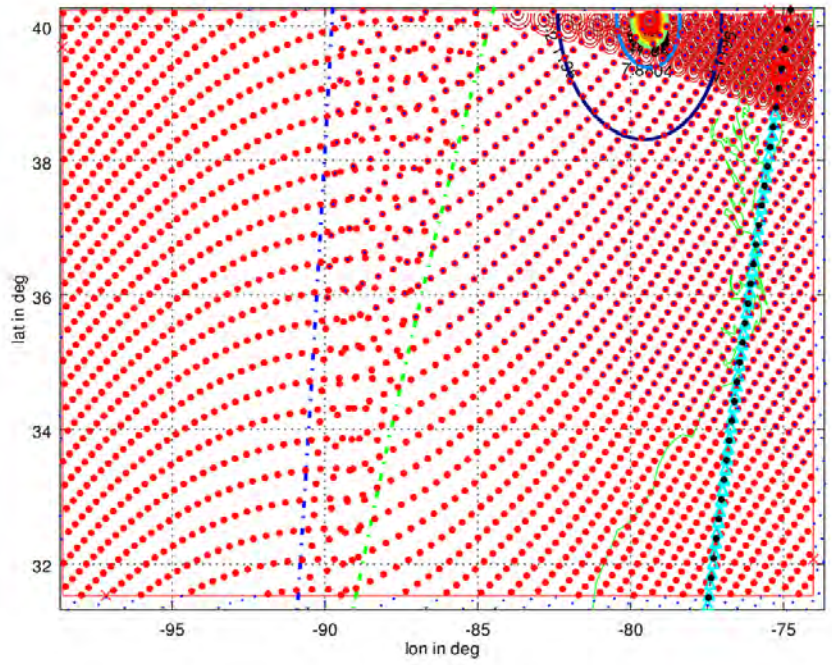

Figure G.4: Detail of reference area. Sample time is 20 ms.

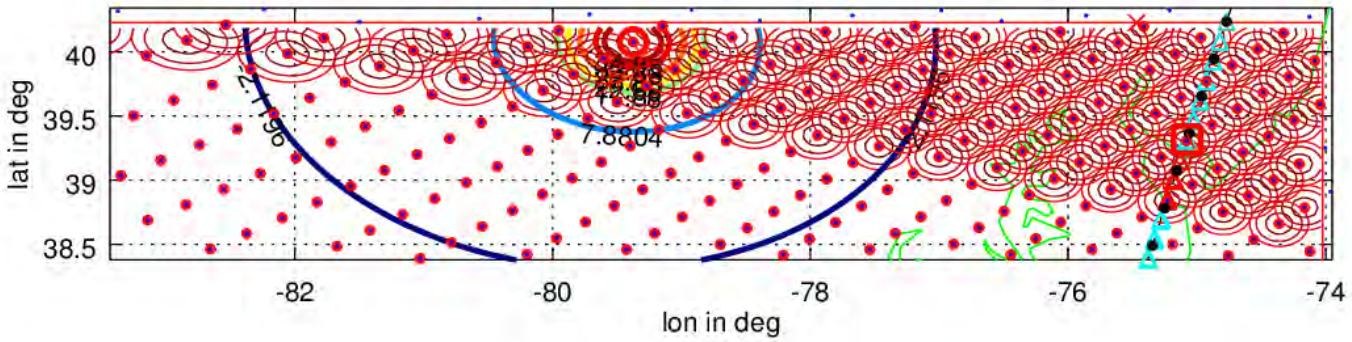

Figure G.5: Detail of reference area incl. contours of sensor main beam gain.
Sample time is 20 ms. Contour plots for several sensor scan points are shown for the 1dB, 3dB, and 5dB contours relative to peak gain.

Finally, Figure G.6 and Figure G.7 show all tracks for the 7 days periods and how densely the area of interest is sampled in the dynamic simulation by approximately 30,000 scan points.

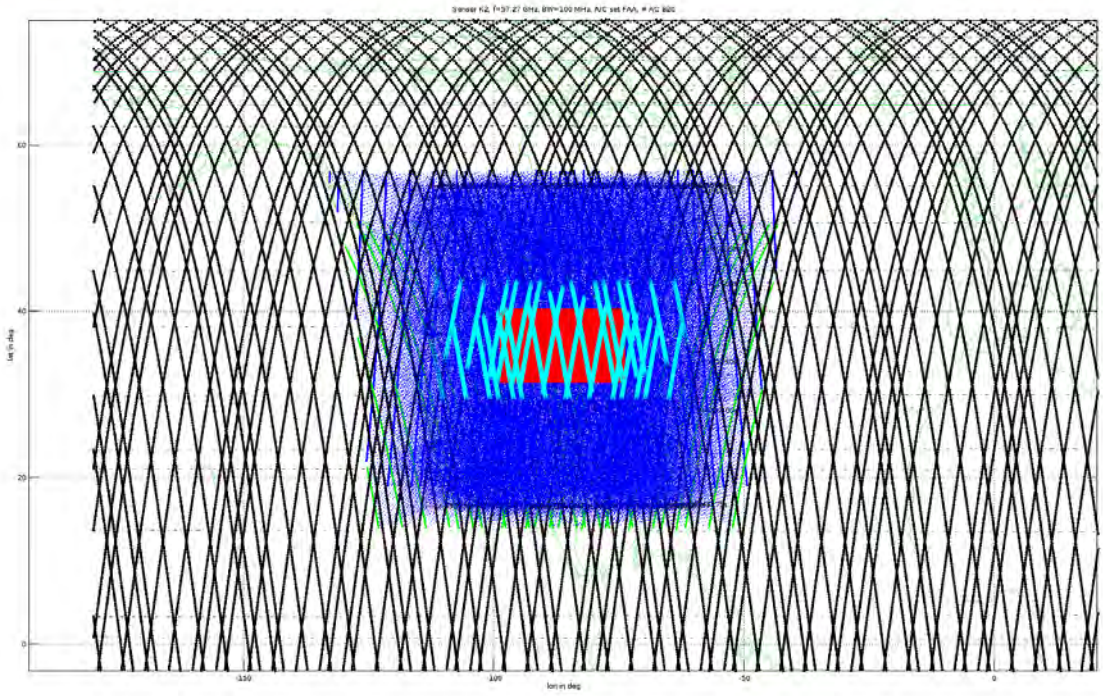

Figure G.6: Satellite tracks for 7 days.

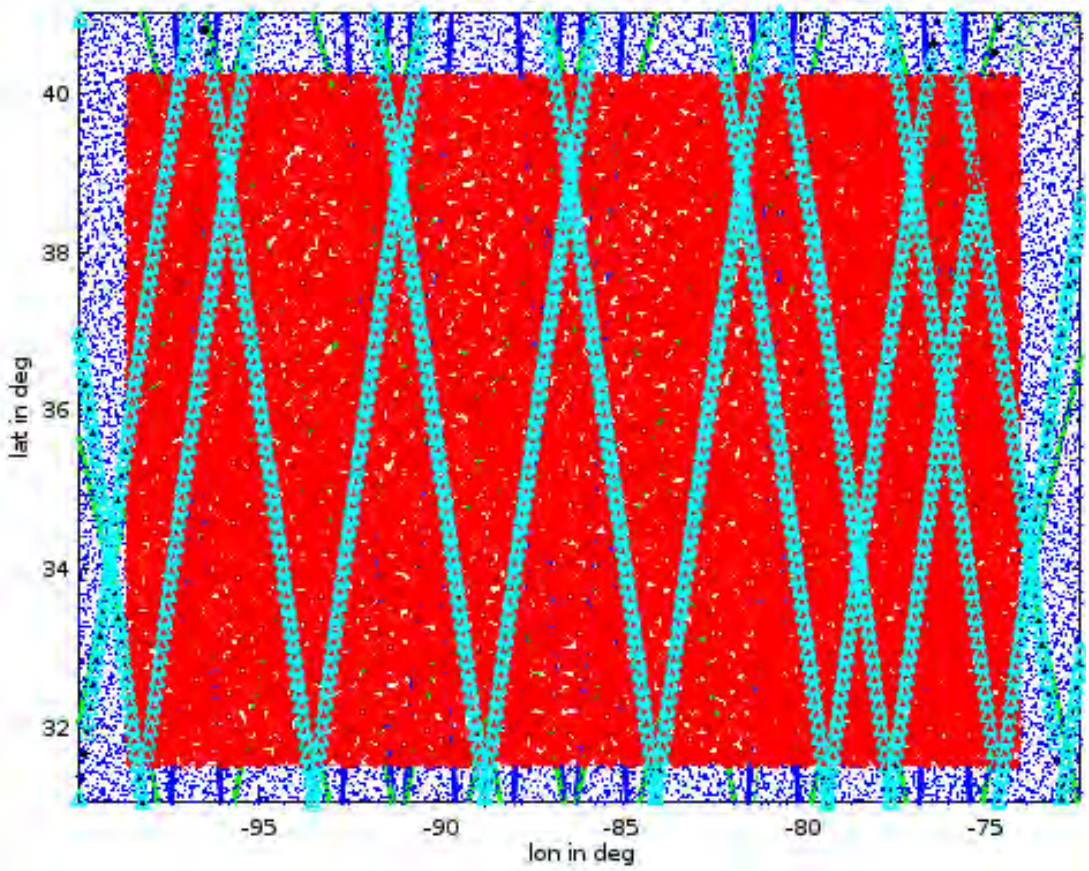

Figure G.7: Satellite tracks over 7 days resulting in ~30,000 scan points in reference area (20 ms sampling period).

H: Atmospheric Attenuation

Figure H.1 below reproduces Fig. 6 of Rec. ITU-R P.676-11 [8], showing that attenuation in the EESS band considered in this report is dominated by dry air attenuation.

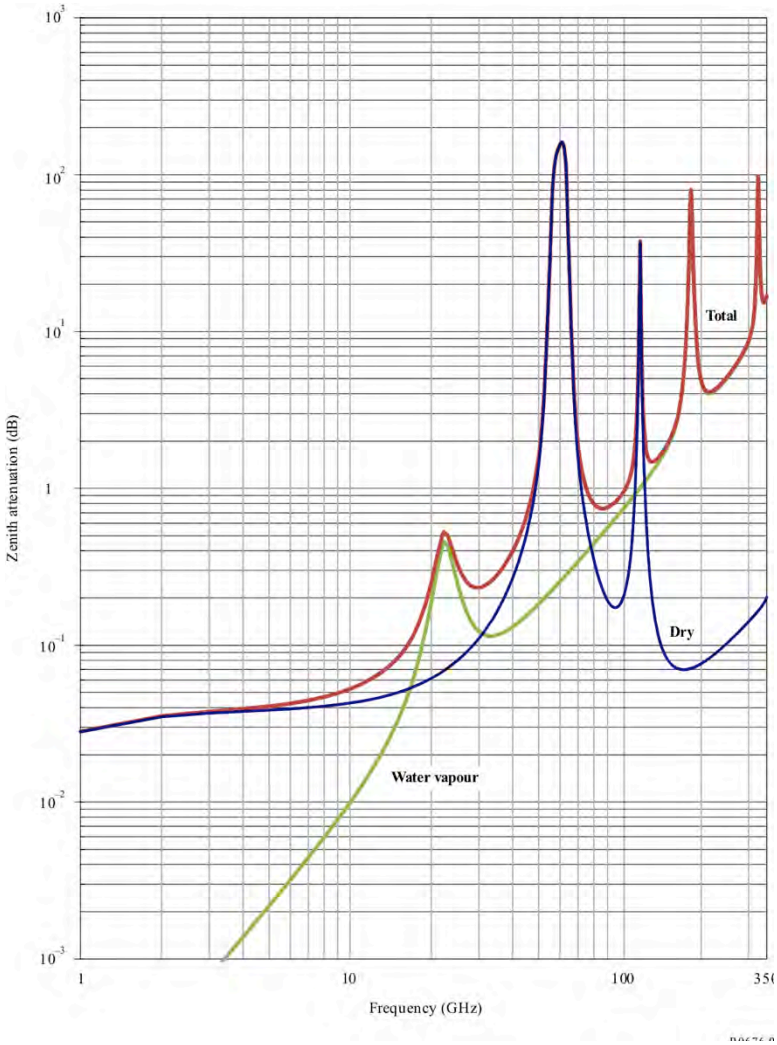

Figure H.1: Ground-space Zenith attenuation for the reference atmosphere; Dry, Water vapor, and total attenuation.

In the simulations implemented to produce interference statistics for this report the atmospheric attenuation is computed using the detailed equations found in Annex 1 of Recommendation ITU-R P.676-11 [8]. The code was successfully validated against the published reference plots from Recommendation ITU-R P.676, cf. Figure H.2 below.

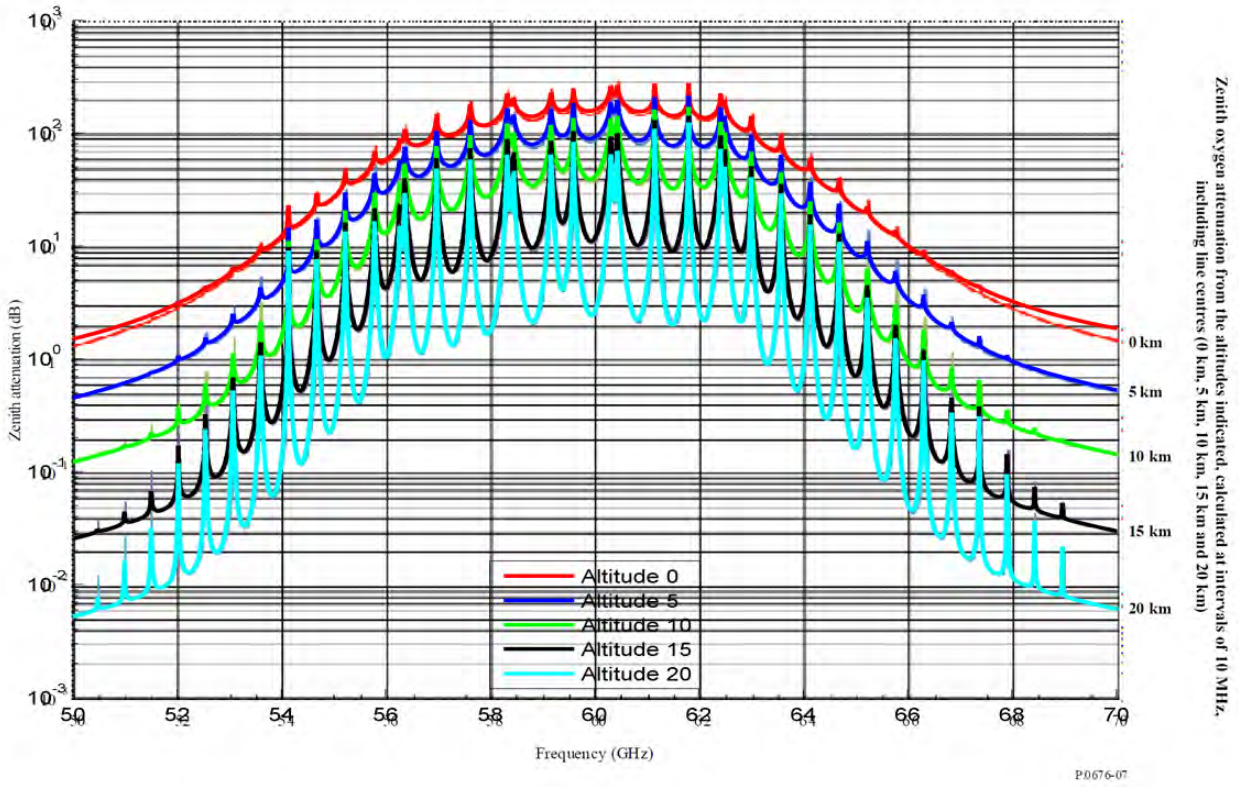

Figure H.2: Zenith attenuation in dB from 50 to 70 GHz.

Computed with the code used for the interference study covered by this report, results agree very well with Fig. 7 of ITU-R Rec. P.676-11 (both graphs are overlaid in the plot).

I: FAA Air Traffic Data Set

This annex summarizes the air traffic data used in this Report.

FAA Air Traffic Control provided a complete data set of high volume air traffic over the continental United States (CONUS) for a period of 7 days, including the peak traffic day of 2016.

The data set was initially filtered to identify all fixed wing aircraft flying within the reference area defined in Annex F.

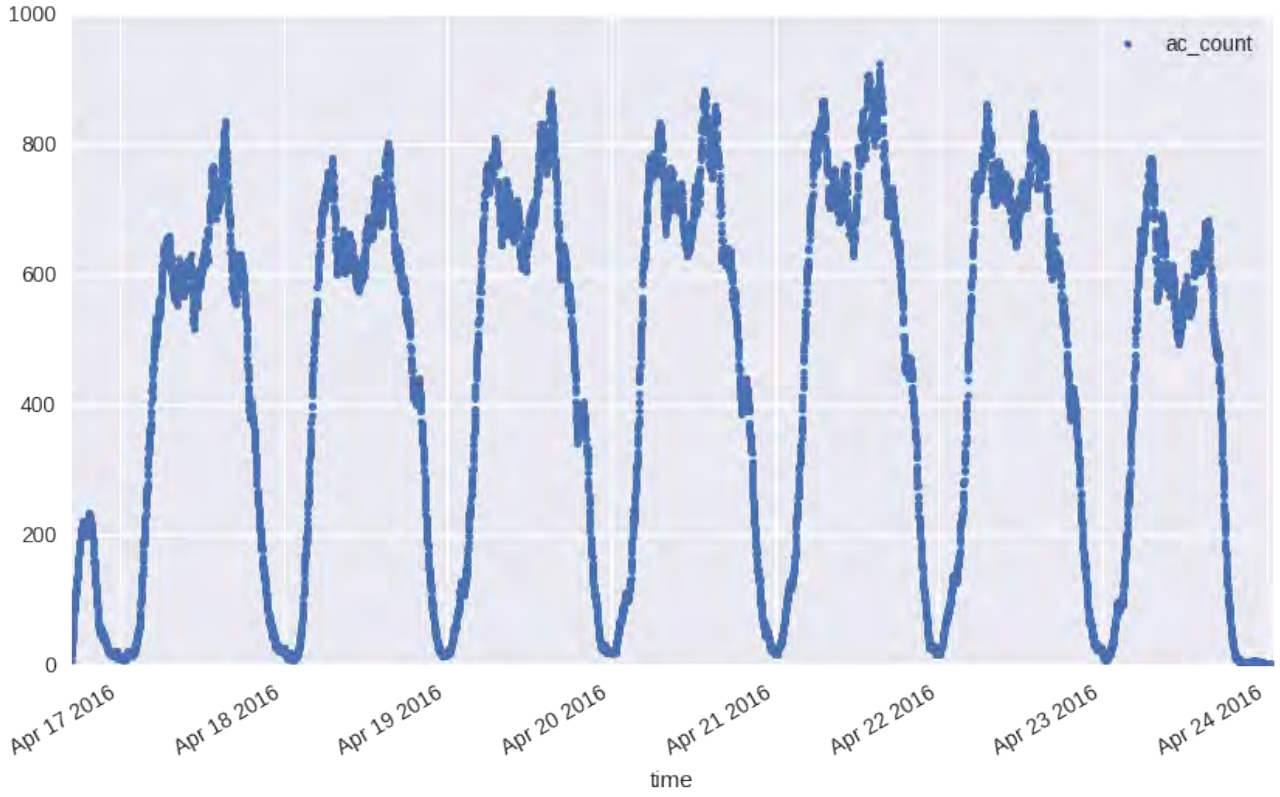

Figure I.1: Aircraft count for data set after initial filtering based on aircraft type and geographical area.
(60s time window; every aircraft is counted only once)

The aircraft traffic data for the peak time is further filtered to only contain aircraft in flight (by only considering aircraft above 50 m in altitude and with at least 200 km/h speed).

This filtering resulted in a total of 820 aircraft containing 69 unique aircraft types, including large twin and single aisle aircraft (typically from Boeing and Airbus) plus a larger percentage of medium sized aircraft. The types included in the aircraft population are identified in Table I.1.

In the interference analysis, it is assumed that all aircraft emit the same interference power towards the EESS satellite, obviously representing a worst-case scenario.

Table I.1: Aircraft population within Reference Area.

#	ICAO 8643 type code	count	accumulated count	accum. Count percentage	#	ICAO 8643 type code	count	accumulated count	accum. Count percentage
1	A320	69	69	8%	**35**	A332	4	753	92%
2	B738	68	137	17%	**36**	A333	4	757	92%
3	B737	63	200	24%	**37**	B753	4	761	93%
4	A319	57	257	31%	**38**	B77W	4	765	93%
5	CRJ2	48	305	37%	**39**	E190	4	769	94%
6	E170	41	346	42%	**40**	F900	4	773	94%
7	CRJ7	40	386	47%	**41**	B734	3	776	95%
8	CRJ9	39	425	52%	**42**	B772	3	779	95%
9	E145	36	461	56%	**43**	C650	3	782	95%
10	A321	30	491	60%	**44**	GLEX	3	785	96%
11	MD88	26	517	63%	**45**	LJ75	3	788	96%
12	B739	18	535	65%	**46**	B744	2	790	96%
13	BE40	17	552	67%	**47**	CL35	2	792	97%
14	C56X	17	569	69%	**48**	DC10	2	794	97%
15	MD83	17	586	71%	**49**	E135	2	796	97%
16	B752	16	602	73%	**50**	GLF5	2	798	97%
17	C560	14	616	75%	**51**	HA4T	2	800	98%
18	E45X	12	628	77%	**52**	LJ31	2	802	98%
19	MD90	12	640	78%	**53**	MD82	2	804	98%
20	B712	11	651	79%	**54**	B462	1	805	98%
21	B763	9	660	80%	**55**	B722	1	806	98%
22	GLF4	9	669	82%	**56**	B762	1	807	98%
23	CL30	8	677	83%	**57**	B77L	1	808	99%
24	CL60	8	685	84%	**58**	B789	1	809	99%
25	B733	7	692	84%	**59**	C25C	1	810	99%
26	C750	7	699	85%	**60**	FA20	1	811	99%
27	F2TH	7	706	86%	**61**	G150	1	812	99%
28	LJ45	7	713	87%	**62**	G280	1	813	99%
29	MD11	7	720	88%	**63**	GL5T	1	814	99%
30	A306	6	726	89%	**64**	GLF6	1	815	99%
31	C680	6	732	89%	**65**	J328	1	816	100%
32	E55P	6	738	90%	**66**	LJ35	1	817	100%
33	FA50	6	744	91%	**67**	LJ40	1	818	100%
34	H25B	5	749	91%	**68**	LJ60	1	819	100%
					69	SBR1	1	820	100%

Distribution of the aircraft population in the reference area over altitude is summarized in the figures below. Figure I.2 shows the aircraft altitude distribution, which must be considered in the analyses due to the effects free air attenuation.

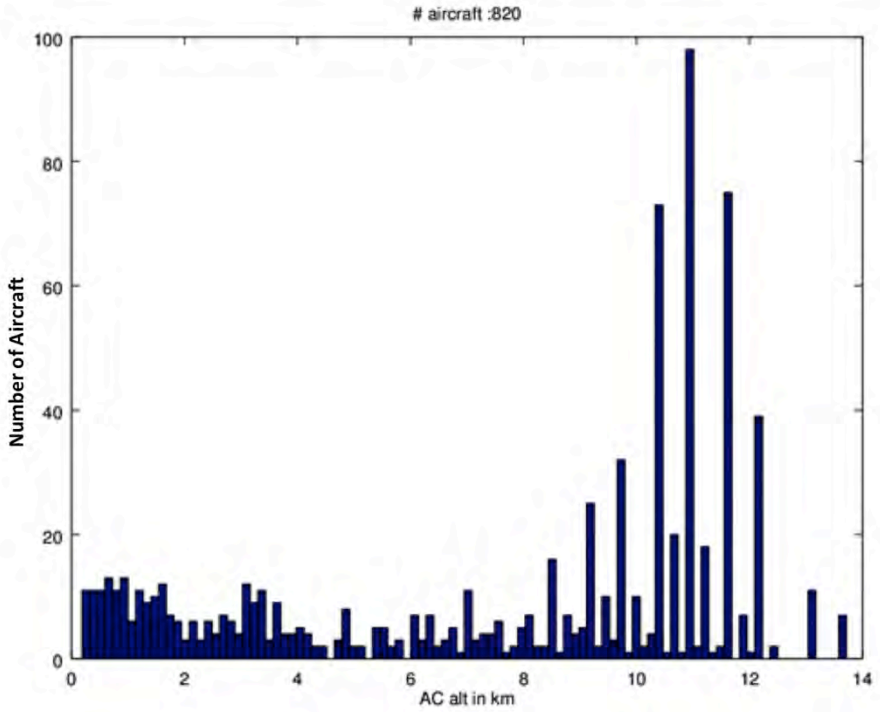

Figure I.2: Aircraft altitude distribution.

A histogram of the speed of aircraft within the reference area is provided in Figure I.3. Aircraft speed impacts the potential for LoS interference.

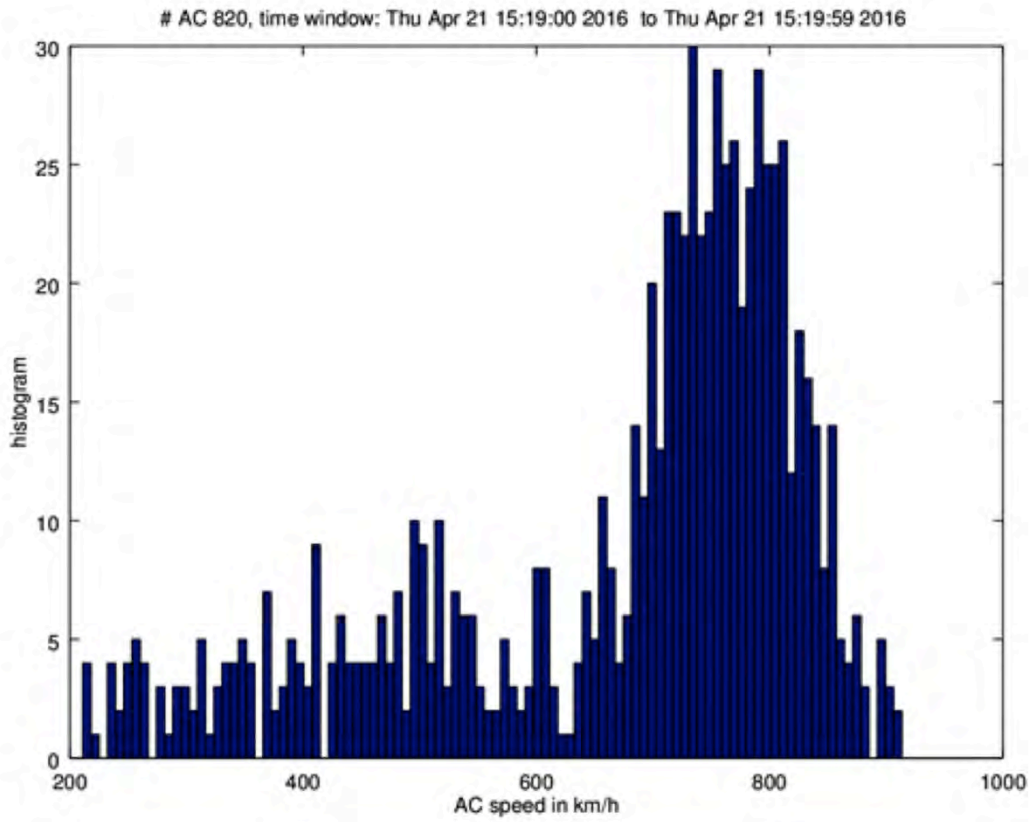

Figure I.3: Aircraft speed distribution.

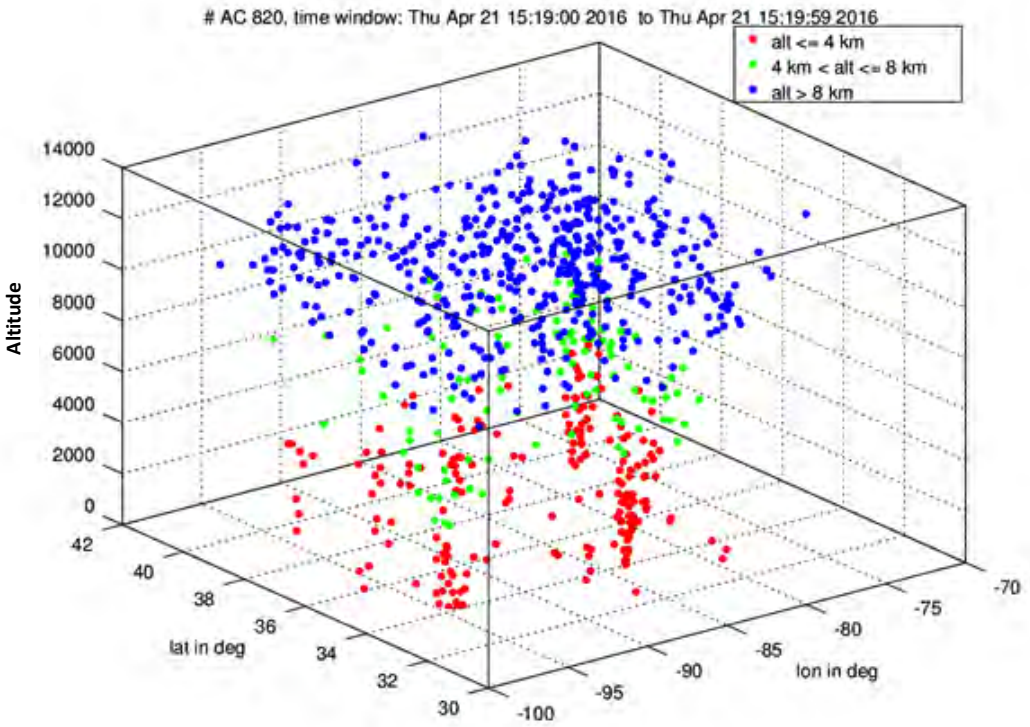

Figure I.4: Aircraft distribution for peak.

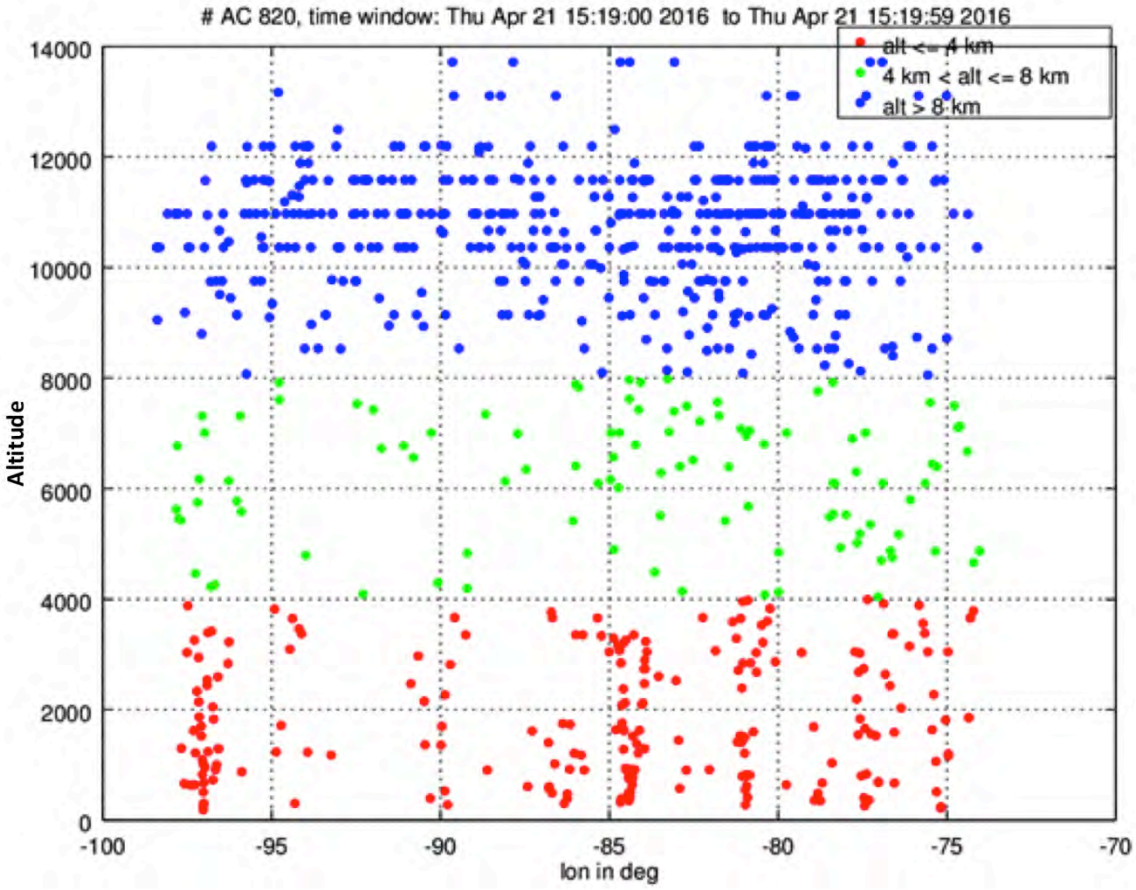

Figure I.5: Aircraft distribution for altitude.

Figure I.6 illustrates the geographical distribution of aircraft across the reference area at the peak traffic period in the analysis.

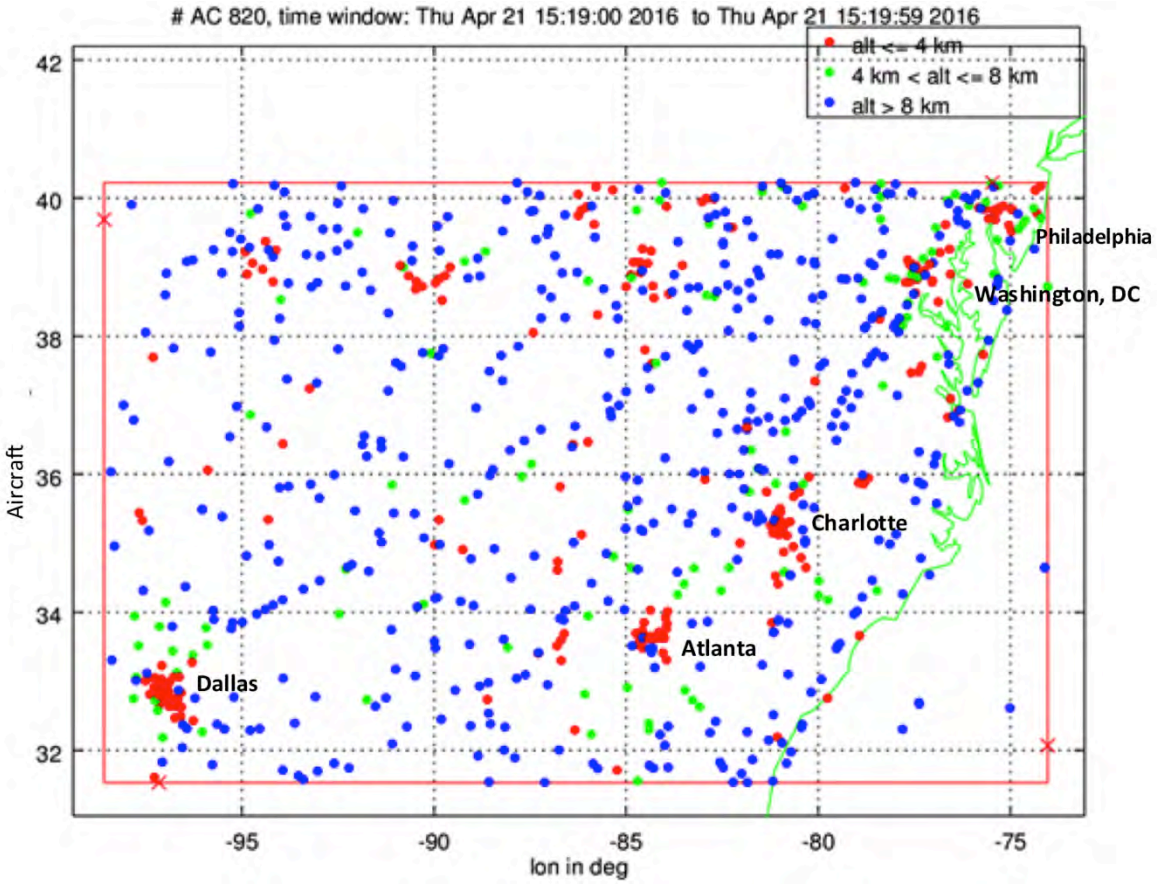

Figure I.6: Distribution of aircraft for peak time step, 60s time window (altitude, long/lat) within 2e6 km^2 reference area.